



Barium and strontium isotope fractionation by cyanobacteria forming intracellular carbonates

Neha Mehta, Margot Coutaud, Julien Bouchez, Kirsten van Zuilen, Harold J. Bradbury, Frederic Moynier, Caroline Gorge, Feriel Skouri-Panet, Karim Benzerara

► To cite this version:

Neha Mehta, Margot Coutaud, Julien Bouchez, Kirsten van Zuilen, Harold J. Bradbury, et al.. Barium and strontium isotope fractionation by cyanobacteria forming intracellular carbonates. *Geochimica et Cosmochimica Acta*, 2023, 356, pp.165-178. 10.1016/j.gca.2023.07.014 . insu-04187882

HAL Id: insu-04187882

<https://insu.hal.science/insu-04187882>

Submitted on 12 Dec 2023

HAL is a multi-disciplinary open access archive for the deposit and dissemination of scientific research documents, whether they are published or not. The documents may come from teaching and research institutions in France or abroad, or from public or private research centers.

L'archive ouverte pluridisciplinaire **HAL**, est destinée au dépôt et à la diffusion de documents scientifiques de niveau recherche, publiés ou non, émanant des établissements d'enseignement et de recherche français ou étrangers, des laboratoires publics ou privés.

1 **Barium and strontium isotope fractionation by cyanobacteria forming intracellular**
2 **carbonates**

3 Neha Mehta¹, Margot Coutaud¹, Julien Bouchez², Kirsten van Zuilen^{2,3}, Harold J. Bradbury^{4,5},
4 Frederic Moynier², Caroline Gorge², Feriel Skouri-Panet¹ and Karim Benzerara^{1*}

5 ¹Sorbonne Université, Muséum National d'Histoire Naturelle, UMR CNRS 7590. Institut de
6 Minéralogie, de Physique des Matériaux et de Cosmochimie (IMPMC), 4 Place Jussieu, 75005
7 Paris, France.

8 ²Université Paris Cité, Institut de physique du globe de Paris (IPGP), CNRS, F-75005 Paris,
9 France

10 ³Shell Global Solutions International B.V., Grasweg 31, 1031 HW Amsterdam, The
11 Netherlands

12 ⁴Department of Earth Sciences, University of Cambridge, Cambridge, CB2 3EQ, UK

13 ⁵Department of Earth, Ocean and Atmospheric Sciences, University of British Columbia, 2020-
14 2207 Main Mall, Vancouver, British Columbia, V6T 1Z4, Canada.

15 *Corresponding author: karim.benzerara@sorbonne-universite.fr

16 **Keywords:** cyanobacteria; barium isotopes; strontium isotopes; stable isotope fractionation;
17 carbonate biomineralization

18

19

20

21

22

23

24

25

26 **ABSTRACT:**

27 While barium (Ba) and strontium (Sr) stable isotopes are increasingly used as tracers of
28 biogeochemical processes and paleo-proxies, the role of biotic processes on Ba and Sr isotope
29 fractionation is poorly understood. Here, Ba and Sr stable isotope fractionations were studied
30 in the laboratory using *Gloeomargarita lithophora*, a cyanobacterium that selectively
31 hyperaccumulates Ba and Sr within intracellular amorphous carbonate biominerals. Our results
32 show that lighter Ba and Sr isotopes are enriched in *G. lithophora* cells compared to the initial
33 solution by $-0.24\text{\textperthousand}$ to $-0.03\text{\textperthousand}$ ($\delta^{137}\text{Ba}$) and $-0.33\text{\textperthousand}$ to $-0.01\text{\textperthousand}$ ($\delta^{88}\text{Sr}$) depending on the stage
34 of the experiment. The fractionation of Ba and Sr isotopes is distinct in magnitude from that
35 occurring during abiogenic and other known biogenic carbonate formation cases. Additionally,
36 using a Rayleigh fractionation model, the fractionation factors of Ba and Sr isotopes between
37 *G. lithophora* cells and the fluid (the growth medium), i.e., $\Delta^{137}\text{Ba}_{(\text{bac-sol})}$ and $\Delta^{88}\text{Sr}_{(\text{bac-sol})}$, were
38 equal to $-0.25\text{\textperthousand}$ and between $-0.46\text{\textperthousand}$ and $-0.38\text{\textperthousand}$, respectively. Interestingly, $\delta^{137}\text{Ba}_{\text{sol}}$ and
39 $\delta^{88}\text{Sr}_{\text{sol}}$ decreased at the end of Ba and Sr uptake stages back towards their initial values, which
40 caused departures from the Rayleigh fractionation model. This suggests the existence of a back
41 reaction resulting in a Ba and Sr outflux from cells to the solution. Possible hypotheses for this
42 back-reaction include dissolution of amorphous carbonate inclusions in response to cellular
43 stress, or a first-order rate dependence of amorphous carbonate dissolution on the amount of Ba
44 and Sr inside the cell. Our findings suggest that bacteria forming intracellular amorphous
45 carbonates could introduce Ba and Sr isotope variability in environmental records, especially
46 in environments where they thrive. Moreover, the enrichment of lighter isotopes of Ba and Sr
47 during amorphous carbonate formation is consistent with that occurring during the formation
48 of other biogenic carbonates but slightly differs in magnitude, opening a discussion about the
49 possibility to use $\Delta^{137}\text{Ba}_{(\text{bac-sol})}$ and $\Delta^{88}\text{Sr}_{(\text{bac-sol})}$ as an indicator of intracellular amorphous
50 carbonate biomineralization in the fossil rock record. Overall, this work highlights the

51 complexity of the biological uptake of alkali-earth metals and stresses the overlooked role of
52 bacteria forming intracellular amorphous carbonates in Ba and Sr biogeochemical cycles.

53

54

55

56

57

58

59

60

61

62

63

64

65

66

67

68

69

70

71

72

73

74

75 **1. Introduction**

76 Barium (Ba) and strontium (Sr) and their stable isotopes have received growing
77 interest over the last few years because of their utility as paleo-proxies and involvement in
78 (bio)geochemical processes. For instance, the Sr and Ba to calcium (Ca) ratios in biogenic
79 carbonates, such as otoliths, coral skeletons, foraminifera tests, coccolithophores and bivalve
80 shells have been suggested to record the physicochemical conditions of the environment where
81 the organisms lived (e.g. Cusack and Freer, 2008; Meibom et al., 2008; Avigliano et al., 2021;
82 Ulrich et al., 2021 and references therein). The Ba and Sr stable isotopic compositions of a
83 range of materials have also been used to investigate the modern and past marine cycles of Ba
84 and Sr and to constrain their oceanic budget (e.g. Krabbenhöft et al., 2010; Horner et al., 2015;
85 Cao et al., 2016, 2020; Bates et al., 2017; Hsieh and Henderson, 2017; Teng et al., 2017;
86 Bridgestock et al., 2018; Charbonnier et al., 2018; Paytan et al., 2021; Wei et al., 2021; Zhang
87 et al., 2022). Many experimental studies have focused on Ba and Sr isotope fractionation during
88 inorganic processes such as the precipitation and dissolution of Ba- and Sr-rich carbonates and
89 sulfates (von Allmen et al., 2010; Mavromatis et al., 2016, 2017a; Böttcher et al., 2018;
90 AlKhatib et al., 2022), the incorporation of Ba and Sr in the lattice of Ca-rich carbonates or in
91 barite during mineral growth (Böhm et al., 2012; Fruchter et al., 2016; AlKhatib and
92 Eisenhauer, 2017a, b; Mavromatis et al., 2020) or the transformation of Ca-carbonate and Ca-
93 sulfate into Ba-rich carbonate and Ba-rich sulfate minerals (Böttcher et al., 2018). One aim of
94 these studies was to assess the existence of a link between stable isotope fractionation and
95 parameters such as the mineral growth rate, the saturation state of the solution, the Ca, Ba or Sr
96 partition coefficients between solids and solutions, the salinity, or the temperature. However,
97 relatively few studies have assessed the influence of living organisms on Sr and Ba isotope
98 signatures in the environment. Some studies have analyzed the stable Ba and/or Sr isotopic
99 signature of Earth surface material with the aim to determine the influence of biological activity
100 on the Ba and/or Sr cycles at the scale of soil columns or watersheds (Souza et al., 2010; Bullen

101 and Chadwick, 2016; Charbonnier et al., 2020, 2022). Other studies have mainly focused on Ba
102 and/or Sr isotope composition of marine biomineralizing organisms, and more specifically
103 calcifying organisms (e.g. Gussone et al., 2007; Rüggeberg et al., 2008; Böhm et al., 2012;
104 Raddatz et al., 2013; Stevenson et al., 2014; Vollstaedt et al., 2014; Pretet et al., 2015; Fruchter
105 et al., 2016; Tasker et al., 2016; Hemsing et al., 2018; Mejía et al., 2018). However, none of
106 these studies have addressed the role of cyanobacteria in the Sr and Ba isotope cycles, despite
107 the prominent role of these bacteria in modern and past environments and their significant
108 contribution to the formation of carbonate deposits over geological times (Altermann et al.,
109 2006; Riding, 2006). Consequently, we still lack insight in the extent to which these
110 phototrophic microorganisms fractionate Ba and Sr isotopes and more importantly on how they
111 could potentially impact the Ba and Sr isotope proxy applications.

112 Here, we studied the recently discovered cyanobacterium *Gloeomargarita lithophora*,
113 which is known to hyperaccumulate alkaline earth elements (AEE) with a "sequential"
114 elemental uptake during cellular growth with Ba taken up first, followed by Sr and lastly Ca,
115 resulting in a preferential uptake of heavier AEE (Cam et al., 2016; Blondeau et al., 2018a).
116 The preferential accumulation of heavier AEE by *G. lithophora* is intriguing because high
117 concentrations of Ba and Sr are considered toxic for cellular processes and organisms rarely
118 discriminate these elements owing to their chemical similarity (Abbass, 2014). *G. lithophora*
119 has been found in biofilms associated with modern microbialites in the highly alkaline Lake
120 Alchichica (Mexico) (Couradeau et al., 2012). This cyanobacterium forms intracellular
121 amorphous carbonates and polyphosphate (polyP) inclusions (Benzerara et al., 2014). PolyP
122 inclusions are commonly present in bacteria and serve as a storage form of P and/or energy for
123 cells (Li et al., 2016). They received particular attention since they can be morphologically
124 confused with carbonate inclusions but also because they can be reservoirs of diverse elements,
125 including alkaline earth elements. The detection of amorphous carbonates in *G. lithophora* was

surprising because previously cyanobacteria were believed to favor extracellular rather than intracellular carbonate precipitation (Achbergerová and Nahálka, 2011; Cosmidis and Benzerara, 2022). Moreover, pure abiogenic amorphous calcium carbonate is highly unstable, usually transforming to crystalline calcium carbonate (CaCO_3) polymorphs (e.g. Rodriguez-Blanco et al., 2011). However, the amorphous carbonates found in cyanobacteria remain stable intracellularly during the lifetime of the cells, with no obvious spontaneous transformation to crystalline phases, at least under the conditions that have been studied so far. This may be due to the effect of various organic or inorganic additives (Mg, P), structural water and/or confinement of ACC within small volumes, which have been proposed to stabilize of biogenic amorphous carbonates found in eukaryotes (Loste et al., 2003; Stephens et al., 2010; Cavanaugh et al., 2019; Liu et al., 2020). The process of amorphous carbonate formation occurs within an intracellular compartment of unknown composition, in a biologically controlled manner involving a new gene family (Blondeau et al., 2018b; Benzerara et al., 2022). Moreover, it involves some energy cost for the cells to produce intracellular supersaturation with regard to calcium carbonate, as it has been shown to occur even when the extracellular solution is undersaturated (Cam et al., 2018). The Ba and Sr sequestered by *G. lithophora* are primarily hosted in amorphous carbonates (Cam et al., 2016; Mehta et al., 2022). The distribution coefficients of Sr and Ba between the solution and the solids (expressed as $D_{(\text{Sr})} = [\text{Sr}/\text{Ca}]_{\text{carbonate}}/\text{[Sr}/\text{Ca}]_{\text{solution}}$, $D_{(\text{Ba})} = [\text{Ba}/\text{Ca}]_{\text{carbonate}}/\text{[Ba}/\text{Ca}]_{\text{solution}}$) were much higher for cyanobacterial amorphous carbonate ($D_{(\text{Sr})} = 86$, $D_{(\text{Ba})} = 1370$) than for abiotically synthesized amorphous carbonate ($D_{(\text{Sr})} = 0.6\text{-}0.9$, $D_{(\text{Ba})} = 0.7\text{-}4.3$) or inorganic crystalline Ca carbonates (e.g. $D_{(\text{Ba})} \sim 1.5$; $D_{(\text{Sr})} \sim 1.2$ at 25°C), likely due to some specific biological processes involved in ion uptake and homeostasis (Tesoriero and Pankow, 1996; Dietzel et al., 2004; Couradeau et al., 2012; Cam et al., 2015; Evans et al., 2020). The preferential accumulation of Sr and Ba was detected under experimental conditions where Ca, Sr and Ba were provided at equal

151 concentrations as well as more environmentally relevant conditions where Sr and Ba were much
152 less abundant, by several orders of magnitudes, than Ca (Blondeau et al., 2018a). Overall, these
153 observations raise the question: is the elemental fractionation trend observed in *G. lithophora*
154 also followed by the Ba and Sr stable isotopes, resulting in preferential uptake of the heavier or
155 lighter isotopes for the given element?

156 The formation of amorphous carbonate is not restricted to *G. lithophora* alone, but
157 taxonomically widespread. The repertoire of microorganisms forming intracellular amorphous
158 carbonates includes many strains of cyanobacteria (Benzerara et al., 2014, 2022), the sulfur-
159 oxidizing gammaproteobacterium *Achromatium* (Benzerara et al., 2021), magnetotactic
160 bacteria affiliated to the Alphaproteobacteria and Gammaproteobacteria (Monteil et al., 2021),
161 and several species of the *Tetraselmis* genus, affiliated to green algae (Martignier et al., 2017).
162 Among all these microorganisms, only *Tetraselmis* and *G. lithophora* have been shown to form
163 Ba- or Sr-enriched amorphous carbonate inclusions (Martignier et al., 2018). Microorganisms
164 forming intracellular amorphous carbonates occur in freshwater and marine environments, as
165 well as in soils, under a wide range of temperatures (Benzerara et al., 2014; Ragon et al., 2014)
166 and are abundant in some environments (e.g. Amarouche-Yala et al., 2014; Bradley et al.,
167 2017). As such, these biominerals have been suggested to be an overlooked component of the
168 Ca, Ba, and Sr geochemical cycles (Blondeau et al., 2018a). Moreover, *G. lithophora* belongs
169 to a deeply rooted lineage in the cyanobacteria phylogenetic tree, suggesting that the amorphous
170 carbonate formation is an ancient process (Ragon et al., 2014; Moreira et al., 2017). Considering
171 the high elemental fractionation of AEE shown by *G. lithophora*, we hypothesize that this may
172 be accompanied by relatively strong isotope fractionation of Sr and Ba. If true, Sr and Ba stable
173 isotope fractionation would provide an additional tool to assess the presence of bacteria forming
174 intracellular amorphous carbonates such as *G. lithophora* in the modern and past environments.
175 Lastly, our current understanding of cellular cycling of Ba and Sr within organisms is poor.

176 Tracing the Ba and Sr isotope fluxes during their uptake by *G. lithophora* could offer new
177 insights into how organisms manage the presence of Ba and Sr in their surroundings, which is
178 otherwise toxic to cellular physiology. Overall, these observations highlight the need of
179 systematic studies investigating the impact of bacteria forming intracellular amorphous
180 carbonates on Ba and Sr stable isotope fractionation.

181 Here, we experimentally determine the stable Ba and Sr isotope fractionation occurring
182 during Ba and Sr uptake by *G. lithophora* cells. This is performed in batch reactors upon cell
183 growth. The findings of these experiments aim to contribute to the following questions: (1) how
184 does *G. lithophora* cycle Ba and Sr intracellularly? and, (2) could stable Ba and Sr isotopes
185 serve as a tracer of the presence of intracellular calcification in modern and past environments?

186 **2. MATERIAL AND METHODS**

187 **2.1. Culture conditions for *G. lithophora* growth**

188 The cyanobacterial uptake experiments were performed in 2000 ml polycarbonate
189 erlenmeyer culture flask (Corning®) as batch cultures open to the atmosphere for 700 h. *G.*
190 *lithophora* was incubated in the 1000 ml BG-11 medium (Stanier et al., 1979), supplemented
191 with Sr and Ba both at a concentration of ~ 260 µM. The BG-11 medium is a growth medium
192 classically used for culturing cyanobacteria. The detailed chemical composition of BG-11
193 medium is given in Table S1. Temperature and luminosity were kept constant at 30°C and 30
194 µmol s⁻¹ m⁻², respectively. The reactors were agitated at 120 rpm in a rotating shaker (INFORS
195 HT celltron AK82). Evaporation was compensated daily by adding sterile de-ionized water
196 prior to sampling. The growth of the cells was monitored by measuring the optical density at
197 730 nm (OD_{730nm}) of the cell suspension using a spectrophotometer (PRIM Secoman). The
198 doubling time of *G. lithophora* cultures was calculated based on the slope of the linear portion
199 (corresponding to exponential phase) of the growth curve (log(OD₇₃₀) *versus* time). The error
200 reported on doubling time is the standard deviation of triplicate measurements. The pH of the

201 cell suspension was measured over the growth of the cells with a CyberScan pH 5500 pH-meter
202 (Eutech instruments) using a combined pH microelectrode (FisherbrandTM) calibrated with
203 Hanna pH standard buffer solutions (4.010, 7.010, 10.010), yielding an uncertainty (1SD) of
204 0.01 pH unit. The initial pH of the cell suspension was 7.5 ± 0.01 (Table S1). Experiments were
205 performed in triplicates. A control, non-inoculated experiment with the same initial conditions
206 as in the cultures was included in the experiment.

207 The Ba and Sr concentrations were monitored over time in three different fractions: the
208 solution, the cells, and the bulk suspension, i.e., the solution plus the cells. All the sampling
209 occurred after a manual homogenization of the cellular suspension under sterile conditions. The
210 solution fraction was collected by filtering the cell suspension through a 0.22- μm Durapore[®]
211 PVDF filter, acidified to pH 2 with 15 M HNO₃ and stored at 5°C before analysis. For the cell
212 fraction, cells were harvested by centrifugation (10 min at 8500 rpm) in acid-cleaned
213 microcentrifuge tubes. The supernatant was subsequently removed, and the cells were acid
214 digested at 20°C, first in 15 M HNO₃ for 30 min, followed by 0.5 M HNO₃ for 24 h. Bulk
215 samples were acid-digested using 0.5 M HNO₃ for 24 h at 20°C in acid-cleaned microcentrifuge
216 tubes. After 24 h of digestion, both the cell and bulk sample fractions were filtered (0.22 μm)
217 and filtrates were stored at 5°C before analyses. The Ba and Sr concentrations were measured
218 in the acidified fractions (solution, cells, and bulk) using inductively coupled plasma-optical
219 emission spectrometry (ICP-OES, iCAP6200 Thermofisher) or inductively coupled plasma-
220 mass spectrometry (ICP-MS, Agilent 7900) at the High-Resolution Analytical Platform (PARI)
221 of the Institut de Physique du Globe de Paris (IPGP), Paris, France. The measurement
222 uncertainty was calculated as the 2SD of three repeat measurements on the sample, and ranged
223 between 2% and 6%. For ICP-OES analysis, the quantification limit for Ba and Sr, calculated
224 as the mean plus 10 times the SD of blank solution concentrations (HNO₃ 2-3%; ~10 repeats),
225 were 0.3 parts per billion (ppb) and 0.1 ppb, respectively. For ICP-MS analysis, the

quantification limit for Ba and Sr, calculated as the mean plus 10 times the SD of blank solution concentrations (~10 repeats), were 6 parts per trillion (ppt) and 2 ppt, respectively. The acid digestion protocol used in this study resulted in about 93% and 98% recovery (referred as elemental yield) of Ba and Sr (Figure S1). We note that the low Ba elemental yield for t<360 h is not considered to be of concern, as it is still in the range of 80%-90%, compared to Ba elemental yield of 93% across the rest of the experiment. Visual MINTEQ was used to estimate saturation indices of the initial growth medium (BG-11) with respect to some mineral phases (Gustafsson, 2012). Computations were carried out using the chemical make-up of the initial growth medium BG-11 as shown in Table S1. The cultures were set-up to be in free exchange with the atmosphere with a partial CO₂ pressure of 380 ppm. Saturation indices of the solution with respect to all Ca or Ba or Sr mineral phases were calculated using the solubility constants reported in the Visual MINTEQ thermodynamic database as well as with amorphous calcium carbonate using a solubility constant of 2.32 x 10⁻⁸ (Kellermeier et al., 2014).

2.2. Scanning transmission electron microscopy (STEM) observations

G. lithophora cells (4 µm in length and 1 µm in width) (Moreira et al., 2017) were observed by scanning transmission electron microscopy (STEM) at different time points, to investigate the cellular distribution of sequestered Ba and Sr. Cell suspensions were harvested by centrifugation at 8500 rpm for 10 min. The supernatant was removed, and the cell pellet was rinsed thrice with de-ionized water. A ~ 2–3 µL drop was deposited on a 200-mesh carbon-film-covered copper grid, air-dried and stored at room temperature before STEM analyses.

STEM measurements were performed using a JEOL 2100F field emission gun instrument operating at 200 kV. The microscope was equipped with a JEOL STEM detector and STEM analyses were performed in the high angle annular dark field (HAADF) mode with a 1-nm probe. X-ray energy dispersive spectrometry (XEDS) was conducted to characterize the elemental composition of the samples using a JEOL XEDS detector with a 140-eV resolution.

251 **2.3. Sr isotope analyses**

252 Aliquots of the solution, digested cells and bulk samples (see section 2.1) from two
253 replicates, were evaporated at 90°C in acid-cleaned Savillex® Teflon vials and re-dissolved in
254 0.1 mL of 5 M HNO₃. Depending on the Sr concentration of the initial sample, two different
255 procedures were performed for separating Sr from the sample matrix, both based on ion
256 exchange chromatography. (1) Samples with a Sr concentration higher than 7 µM were
257 processed with an automated set-up, using a DX120 ion chromatographic column following the
258 procedure described in (Meynadier et al., 2006). (2) Samples with Sr concentrations lower than
259 7 µM were processed manually, using the Sr-SPEC resin (Eichrom™) following the protocol
260 of (Hajj et al., 2017). In both cases, the Sr purification step was performed twice sequentially,
261 to maximize the Sr purity (Romaniello et al., 2015). The Sr recovery during the chromatography
262 separation procedure, calculated as the difference between the Sr mass in the sample before and
263 after purification was quantified using ICP-MS and was higher than 95% for both separation
264 procedures. After Sr purification, the collected fractions were evaporated at 90°C. Organic
265 residues were subsequently oxidized with 2 µL of 15 M HNO₃ at 90°C. After evaporation, the
266 samples were once again re-dissolved in 0.5 M HNO₃ to a final Sr concentration of 100 or 200
267 ppb, depending on the Sr mass of the sample. Total procedural blanks were below 0.7 ng Sr,
268 corresponding in any case to less than 0.1% of the Sr mass processed, which can be considered
269 as negligible.

270 Strontium isotope ratios were measured using a Neptune Plus MC-ICP-MS
271 (Thermo Scientific) at the PARI platform of IPGP (Paris, France). Samples were introduced
272 using an APEX desolvating unit coupled with a PFA nebulizer. Signals for the following
273 isotopes were measured: ⁸²Kr⁺, ⁸³Kr⁺, ⁸⁴Sr⁺, ⁸⁵Rb⁺, ⁸⁶Sr⁺, ⁸⁷Sr⁺ and ⁸⁸Sr⁺. The intensity of ⁸³Kr
274 was measured to correct interferences of ⁸⁴Kr and ⁸⁶Kr on ⁸⁴Sr and ⁸⁶Sr, respectively. ⁸⁵Rb was
275 monitored to check for any potential interference of ⁸⁷Rb on ⁸⁷Sr, but the Rb signal was

negligible for all samples. For each measurement, data were collected using a series of 50 cycles with an integration time of 4 s. All signals were measured with Faraday cups connected to $10^{11}\Omega$ resistors, except for the ^{84}Sr signal which was amplified using a $10^{12}\Omega$ resistor. Samples were measured three times on average. In this study, the mean of these repeated measurements is used. The instrumental mass bias and its drift were corrected by using a standard-sample bracketing procedure using strontium standard SRM987 (Fietzke and Eisenhauer, 2006) such that the $^{88}\text{Sr}/^{86}\text{Sr}$ ratios of the samples are reported relative to the NIST standard reference material SRM 987 in the standard delta notation ($\delta^{88}\text{Sr}$), defined as

$$\delta^{88/86}\text{Sr}(\text{\textperthousand}) = 1000 \times \left\{ \frac{(^{88}\text{Sr}/^{86}\text{Sr})_{\text{sample}}}{(^{88}\text{Sr}/^{86}\text{Sr})_{\text{SRM987}}} - 1 \right\} \quad (1)$$

The $\delta^{88}\text{Sr}$ values for the three measured fractions are reported throughout the manuscript as a relative change in $\delta^{88}\text{Sr}$ from the initial isotope composition of the corresponding fraction, and referred as $\delta^{88*}\text{Sr}$. For each measurement, the "radiogenic" $^{87}\text{Sr}/^{86}\text{Sr}$ ratio was calculated using the $^{88}\text{Sr}/^{86}\text{Sr}$ ratio to correct for the effect of instrumental fractionation, using a natural ratio of 8.3752 and the so-called "Russell's law" (Russell et al., 1978).

The three-isotope plot ($\delta^{88}\text{Sr}$ vs $\delta^{87}\text{Sr}$) shows a mass dependent fractionation for all stable Sr isotopes (88, 86, 84 and 88, 87, 86), showing the absence of uncorrected interference (Figure S2). The absence of any matrix effect on the $\delta^{88}\text{Sr}$ measurements using either chromatography approach was checked through the analyses of Sr solution doped with EDTA, iron citrate, or BG-11 medium at three different Sr concentrations (representative of the Sr concentration in our samples—Table S3). The consistency between our Sr isotope measurements could be further evaluated independently using an isotope mass balance (i.e., by comparing the bulk $\delta^{88}\text{Sr}$ value of each sample with the corresponding Sr-weighted sum of the solution and cell $\delta^{88}\text{Sr}$ values), resulting in a mean offset of 0.04‰ (Table S4), well within analytical uncertainty (95% confidence interval). The $^{87}\text{Sr}/^{86}\text{Sr}$ ratio, is by nature, corrected for

300 any effect of mass-dependent fractionation, meaning that it should remain constant in a closed
301 system such as our experimental set-up.

302

303 **2.4. Ba isotope analyses**

304 To measure the Ba isotopic compositions of the different fractions from two replicates, samples
305 with a minimum amount of 300 ng of Ba, were first mixed with a ^{130}Ba - ^{135}Ba double spike (van
306 Zuilen et al., 2016) and evaporated at 100°C. Samples were then re-dissolved in 0.5 mL of 3 M
307 HCl for Ba separation by ion exchange chromatography with 1.1 mL of Dowex® 50WX8 cation
308 exchange resin following the protocol by (van Zuilen et al., 2016). Total procedural blanks were
309 below 0.3 ng Ba (0.16 ng Ba on average), corresponding to less than 0.1% of the total amount
310 of Ba processed. The fractions collected after purification were evaporated at 100°C and re-
311 dissolved in 0.3 M HNO₃ to a final Ba concentration of 100 or 300 ppb, depending on the Ba
312 mass available.

313 Barium isotope analyses were performed using a Neptune Plus MC-ICP-MS at the
314 PARI platform of IPGP, Paris, France. Sample solutions with Ba concentrations of 300 ppb
315 were introduced via a quartz dual cyclonic spray chamber and a PFA nebulizer. For low-
316 concentration samples (i.e., 100 ppb), an APEX desolvating nebulizer was used. Signals of
317 $^{129}\text{Xe}^+$, $^{130}\text{Ba}^+$, $^{131}\text{Xe}^+$, $^{132}\text{Ba}^+$, $^{134}\text{Ba}^+$, $^{135}\text{Ba}^+$, $^{136}\text{Ba}^+$, $^{137}\text{Ba}^+$ and $^{138}\text{Ba}^+$ were measured
318 simultaneously. Data were collected by a series of 100 cycles with an integration time of 4 s.
319 Samples were measured twice on average. Instrumental mass bias was corrected by using a
320 ^{130}Ba - ^{135}Ba double spike (for more details see (van Zuilen et al., 2016)). Xe interference on
321 masses 130, 132, 134 and 136 were calculated using the $^{129}\text{Xe}^+$ signal and subtracted from the
322 respective total signal. Natural $^{129}\text{Xe}/{}^x\text{Xe}$ ratios (where x denotes 130, 132, 134 or 136) were
323 corrected for instrumental mass bias using the instrumental fractionation factor calculated for

324 Ba (De Laeter et al., 2003). The measured Ba isotope ratios are reported in $\delta^{137/134}\text{Ba}$ relative to
325 the international NIST reference material SRM 3104a:

326

$$\delta^{137/134}\text{Ba} (\text{\textperthousand}) = 1000 \times \left\{ \frac{\left(\frac{^{137}\text{Ba}}{^{134}\text{Ba}} \right)_{\text{sample}}}{\left(\frac{^{137}\text{Ba}}{^{134}\text{Ba}} \right)_{\text{SRM3104a}}} - 1 \right\} \quad (2)$$

327 The $\delta^{137}\text{Ba}$ values for the three measured fractions are reported throughout the
328 manuscript as a relative change in $\delta^{137}\text{Ba}$ from the initial isotope composition of the
329 corresponding fraction and referred to as $\delta^{137*}\text{Ba}$. The intermediate measurement precision of
330 sample analysis was estimated by calculating the pooled standard deviation of all repeated
331 sample measurements and equal to $\pm 0.05\text{\textperthousand}$ ($2 s_p$) on $\delta^{137/134}\text{Ba}$. Accuracy of the analyses was
332 assessed by comparison of the geological reference materials from the USGS (BCR-2, BHVO-
333 1 and AGV-1) and two in-house reference materials (BaBe12 and BaBe27) with other studies.
334 All were in good agreement with literature data (e.g. van Zuilen et al., 2016) within analytical
335 uncertainties (Table S5). The Ba isotope mass balance of each experimental sample did not
336 reveal any significant difference between the bulk $\delta^{137}\text{Ba}$ value and the Ba-weighted sum of the
337 solution and cell $\delta^{137}\text{Ba}$ values (Table S6).

338 **2.4. Calculation of the Ba and Sr isotope fractionation factors using a Rayleigh model**

339 In the following, we first estimate Ba and Sr isotope fractionation factors during their uptake
340 by the bacteria using a Rayleigh fractionation model:

341

$$R_t = R_o f(X)_{sol}^{(\alpha-1)} \quad (4)$$

342 where R_t and R_o represent the $^{137}\text{Ba}/^{134}\text{Ba}$ or $^{88}\text{Sr}/^{86}\text{Sr}$ ratios of the solution at time t and at time
343 $t=0$, respectively; $f(X)_{sol}$ is the fraction of initial $X = \text{Ba}$ or Sr remaining in the solution and α is
344 the fractionation factor. Eq. 4 can be re-arranged so that the slope of a line in a $\ln(R_t/R_o)$:
345 $\ln(f(X)_{sol})$ space is equal to $(\alpha-1)$. The isotope enrichment factor, i.e., the offset between the
346 cyanobacteria and the solution, $\Delta X_{(bac-sol)}$, is accordingly calculated as:

347

$$\Delta X_{(bac-sol)} = 1000 \times (\alpha - 1) \quad (5)$$

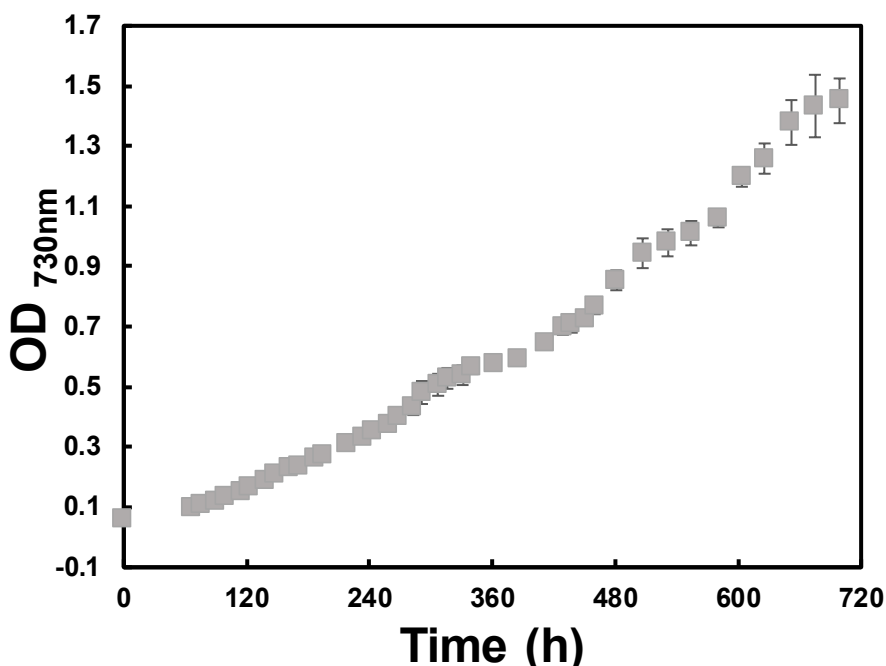
348 where X is ^{137}Ba or ^{88}Sr ; the subscript “bac” corresponds to cyanobacteria and “sol” corresponds
349 to solution

350 **3. RESULTS**

351 **3.1. Growth of *G. lithophora***

352 The OD_{730nm} of *G. lithophora* cell suspensions cultured in the presence of Sr and Ba
353 increased continuously over time from 0.06 to 1.45 OD unit (Figure 1). The cells grew with a
354 doubling time of 106 ± 4 h, comparable with previously reported *G. lithophora* generation times
355 of 92 h (Cam et al., 2016). The increase in OD_{730nm} was accompanied by an increase in pH
356 from 7.5 to 9.3 (Figure S3). No change in pH (7.67 ± 0.06) was detected in the non-inoculated
357 controls (Figure S3). The initial extracellular growth solution was undersaturated with respect
358 to amorphous calcium carbonate and other carbonate minerals (Table S2).

359



360

361 **Figure 1.** Optical density at 730 nm (OD_{730nm}, ■) of *G. lithophora* cultures incubated in the BG-11
362 medium amended with 260 μM Ba and Sr. Data points and error bars correspond to the average

363 and standard deviation of three replicates cultures, respectively. When not visible, error bars are
364 smaller than the symbol size. The OD values are provided in Table S7.

365

366 While pH of the cell suspension was monitored, no alkalinity measurements were made. The
367 increase of the extracellular pH in the growth medium in inoculated control was likely due to
368 the cellular activity, as the pH of the growth medium in non-inoculated controls remained
369 constant over time (Figure S3). Photosynthetic organisms such as cyanobacteria are well known
370 to elevate the extracellular pH resulting from the fixation of CO₂ by RuBisCO (e.g. Middelburg
371 et al., 2020). This results in the production of an extracellular alkaline microenvironment around
372 the cell. The increase in extracellular pH due to photosynthetic activity of *G. lithophora* cells
373 suggest that the health of the *G. lithophora* cells was not adversely affected under our
374 experimental conditions. Similar suggestions were made in previous studies culturing *G.*
375 *lithophora* in presence of Ba and Sr, (e.g. Mehta et al., 2022). Moreover, (Cam et al., 2016)
376 noted that the growth of *G. lithophora* was not affected by the addition of 50 µM Sr and Ba and
377 was even slightly faster with Sr and Ba than with Ca alone.

378 **3.2. Barium and Sr uptake by *G. lithophora***

379 The growth of *G. lithophora* cells was accompanied by a decrease in the concentrations of Sr,
380 Ba and Ca in the solution (Figure 2A). Over time, the concentrations of Sr and Ba in the solution
381 decreased from 250±10 µM (2SD) to 1.5±0.2 µM (2SD), and Ca in the solution decreased from
382 230 µM to 54 µM. The removal of Ba, Sr and Ca in the solution occurred in three stages, as
383 previously observed by (Cam et al., 2016). During the first stage, within 316 h, the
384 concentrations of Ba in the solution decreased from 250±10 µM to 2.5±0.75 µM , and the
385 concentrations of Sr and Ca decreased from 250±10 µM to 211±15 µM and 170±12.5 µM
386 respectively. In the second stage (316 h < t < 554 h), the Ba concentration in the solution
387 remained below 3.9 µM, while Sr concentration decreased from 211±15 µM to 2.5±0.5 µM.
388 Unlike in the first stage, the Ca concentration increased to reach a value close to the initial Ca

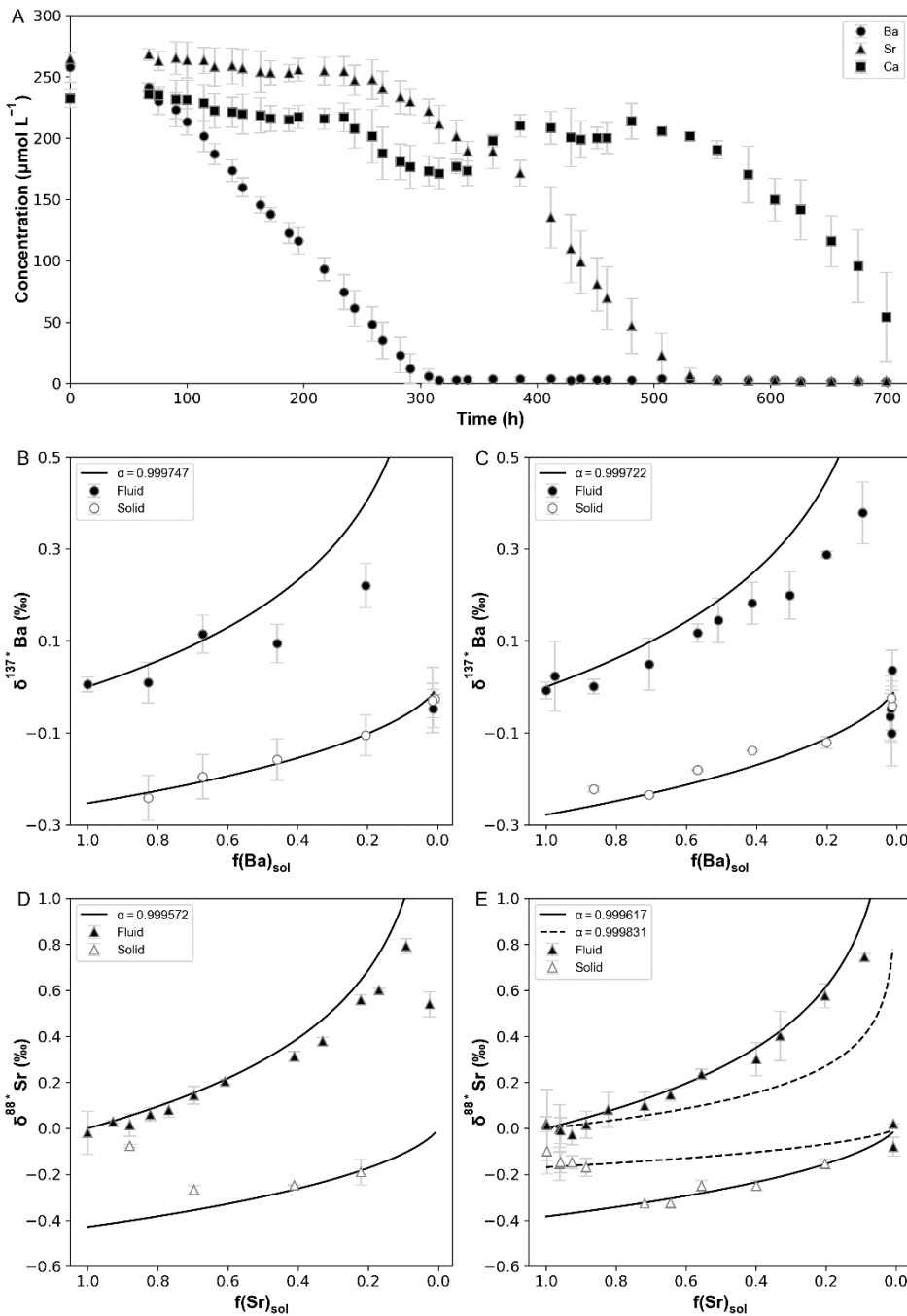
389 concentration in the middle of the second stage (~400 h). In the second half of the second stage
390 ($400 \text{ h} < t < 554 \text{ h}$), Ca concentration starts decreasing from $208 \pm 13 \mu\text{M}$ to $190 \pm 10 \mu\text{M}$. Finally,
391 in the last stage, Sr concentration reached a value below $2.1 \mu\text{M}$ and Ba concentration remained
392 below $1.5 \mu\text{M}$ and Ca concentration decreased from $190 \pm 7.5 \mu\text{M}$ to $54 \pm 36 \mu\text{M}$. The total Ba
393 and Sr removed from the solution were associated with the growth of *G. lithophora* cells as
394 evidenced by the Ba and Sr mass balance between cell, solution, and bulk fractions and electron
395 microscopy observations (Figure S4, Figure 3 and section 3.4). The trends in Ba and Sr uptake
396 by *G. lithophora* cells were also observed under conditions where *G. lithophora* was grown at
397 lower concentrations of Ba and Sr (Blondeau et al., 2018a). This suggests that preferential and
398 massive uptake of both Ba and Sr by *G. lithophora* operates in a similar way at low or high
399 extracellular concentrations of Sr and Ba.

400 In the non-inoculated controls (Figure S5B), the Sr and Ca concentrations in the solution was
401 equal to the bulk fraction Sr and Ca concentrations over time and remained nearly equal to the
402 initial concentration of Sr and Ca. In contrast, Ba concentration decreased in both solution and
403 bulk fractions over time in the non-inoculated control (Figure S5A). The decrease in Ba
404 concentration in controls could be due to precipitation of barite (BaSO_4) as the initial
405 extracellular solution was oversaturated with this phase (Table S2). However, the decrease in
406 Ba concentration in non-inoculated control cannot be due to Ba removal in another mineral
407 phase as the decrease in Ba concentration was the same for the solution (dissolved fraction only)
408 and the bulk suspension (i.e. dissolved+ cell fractions) in the control, suggesting the sink of Ba
409 in non-inoculated controls is adsorption. Indeed, adsorption to the culture flask in the controls
410 results in the elemental yield normalized to initial Ba concentration to decrease from 100% to
411 34% (Figure S5D). Unlike controls, adsorption is not a major sink of Ba compared to cells as
412 the Ba elemental yield normalized to initial Ba concentration remains >90% whereas in controls

413 it drops to 34%, suggesting that Ba uptake by cells outcompeted Ba adsorption on the culture
414 flask.

415 **3.3 Evolution of the Ba and Sr isotope composition upon cell uptake**

416 With the removal of dissolved Ba and Sr, the $\delta^{137*}\text{Ba}_{\text{sol}}$ (Ba isotope composition of the solution)
417 increased up to 0.38‰, for the proportion of Ba remaining in the solution ($f(\text{Ba})_{\text{sol}}$) of 0.10
418 (Figure 2B-C, Table S9) and the $\delta^{88*}\text{Sr}_{\text{sol}}$ (Sr isotope composition of the solution) increased up
419 to 0.79‰, for the proportion of Sr remaining in solution ($f(\text{Sr})_{\text{sol}}$) of 0.09 (Figure 2D-E, Table
420 S10). Throughout the duration of the experiments, $\delta^{137*}\text{Ba}_{\text{bac}}$ (Ba isotope composition of the
421 cells) and $\delta^{88*}\text{Sr}_{\text{bac}}$ (Sr isotope composition of the cells) were negative relative to the solution
422 (Figure 2; Tables S9-S10). The solution reached isotope compositions close to those of the
423 bacteria at ~340 h for Ba (Fig. 2B-C) and at ~550 h for Sr (Fig. 2D-E).



424

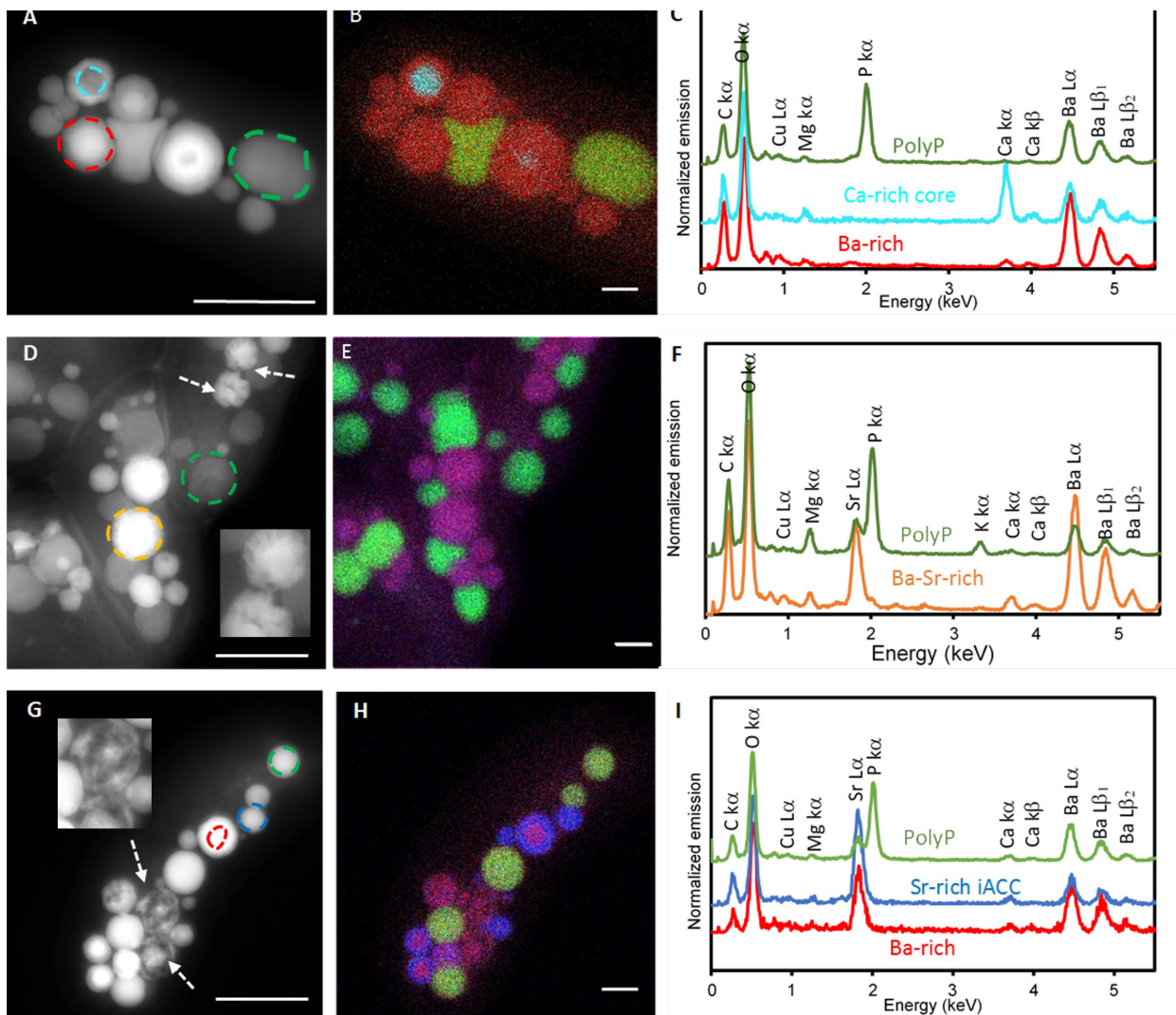
425 **Figure 2:** (A) Temporal evolution of Ba (black dots), Sr (black triangle), and Ca (black squares)
426 dissolved concentrations during the growth of *G. lithophora*. Data points and error bars
427 correspond to the average and $2 \times \text{SD}$ of three replicates cultures, respectively. When not visible,
428 error bars are smaller than the symbol size. The associated numerical values are provided in Table
429 S8. (B-E): Temporal evolution of the Ba (top) and Sr (bottom) stable isotope composition of the
430 solution (● for Ba and ▲ for Sr) and bacteria (○ for Ba and △ for Sr) fractions in two replicates
431 (left column, right column) as a function of the fraction of the element remaining in the solution
432 ($f(\text{element})_{\text{sol}}$). Error bars correspond to the analytical 2 SD. For Ba replicates (B, C), the solid
433 lines represent Rayleigh fits to $\delta^{137}\text{Ba}$ values of solution and bacteria for $f(\text{Ba})_{\text{sol}} > 0.2$. The
434 numerical $\delta^{137}\text{Ba}$ values are provided in Table S9. For Sr replicates (D, E), the solid line represents
435 the fit obtained when using data from the whole exponential growth stage ($f(\text{Sr})_{\text{sol}} \leq 0.72$), while
436 for replicate (E) the dashed line represents the fit obtained when using only data from the early

437 Sr uptake ($0.88 \leq f(\text{Sr})_{\text{sol}} < 1$; $123 < t < 291$ h). The numerical $\delta^{88}\text{Sr}$ values are provided in Table
438 S10.

439

440 **3.4. Cellular distribution of Ba and Sr in *G. lithophora***

441 In this study, the term amorphous carbonate refers to inclusions with different chemical
442 compositions ranging from Sr-rich to Ba-rich and Ca-rich. The cellular distribution of
443 sequestered Ba and Sr was determined using STEM-EDXS analyses. STEM-HAADF images
444 and the corresponding EDXS analyses (Figure 3) show that during the Ba uptake stage, some
445 amorphous carbonate inclusions showed a Ca-rich core and a Ba shell at 282 h (Figure 3A).
446 Moreover, polyP granules containing some Ba and/or Sr were also observed. Some amorphous
447 carbonate granules observed during the Sr uptake stage (at $t = 481$ h) were enriched in Sr-Ba
448 (Figure 3D). At 580 h, the cells contained amorphous carbonate inclusions with a Sr-rich shell
449 and a Ba-rich core, but also simple Sr-rich inclusions. Some amorphous carbonate inclusions
450 had an appearance of having rugged/pitted surfaces (Figures 3D and 3G). The EDXS maps
451 showed that Ba and Sr were less abundant in the polyP than in the carbonate granules, consistent
452 with previous studies showing that Ba and Sr are primarily hosted in amorphous carbonates
453 formed by *G. lithophora* (Cam et al., 2016; Li et al., 2016; Mehta et al., 2022). No peak
454 corresponding to sulfur was detected in the EDXS spectra of inclusions, confirming that the
455 amorphous inclusions were not sulfate solids (Figure 3C, Figure 3F; Figure 3I).



456

457
458
459
460
461
462
463
464
465
466
467
468
469
470
471

Figure 3. STEM-EDXS images and analyses of *G. lithophora* cells collected after 282 h (A, B, C) during the Ba uptake stage, after 481 h (D, E, F) during the Sr uptake stage, after 580 h (G, H, I). (A, D, and G): STEM-HAADF images of cells showing layered amorphous carbonate granules at 282, 451, and 580 h respectively. Colored circles show the different areas analyzed by EDXS. Arrows indicate amorphous carbonate inclusions with rugged/pitted surface. (B, E, and H): corresponding EDXS overlay chemical maps of Ca (cyan), Ba (red), Sr (dark blue), and P (green). As a result, Ba-Sr-rich amorphous carbonate inclusions appear in magenta. (C): EDXS spectra of a Ba-rich amorphous carbonate granule, the Ca-rich core of an amorphous carbonate granule, and a PolypP granule from panel A (red, cyan, and green circles, respectively). (F) EDXS spectra of a Ba-Sr rich amorphous carbonate granule and a PolypP granule from panel D (yellow and green circles). (G): EDXS spectra of the Sr-rich amorphous carbonate, the Ba-rich amorphous carbonate with a Sr-rich outer shell, and the PolyP granule from panel G (blue, red, and green circles, respectively). All scale bars represent 0.5 μm. The numerical values of the EDXS spectra are provided in Table S11. The insets in (D, G) show magnified views of amorphous carbonates inclusions with rugged/pitted appearance.

472 **4. DISCUSSION**473 **4.1. Barium and Sr intracellular carbonatogenesis is a dynamic process as highlighted by**
474 **isotopic fractionation**

475 As an initial attempt to quantitatively understand the observed Ba and Sr isotope fractionation
476 patterns during uptake of these elements by *G. lithophora*, the isotope data were modeled using a
477 Rayleigh distillation equation (Eq 4). The Rayleigh distillation simulations were conducted using
478 the data points of the cell samples corresponding to $0.2 \leq f(\text{Ba})_{\text{sol}} < 1$ ($0 < t < 270$ h) and $0.2 \leq$
479 $f(\text{Sr})_{\text{sol}} < 1$ ($123 \leq t \leq 480$) in Figure 2. Significant departures from the Rayleigh model were
480 observed in the later stage of the element uptake, corresponding to $f(\text{Ba})_{\text{sol}} \leq 0.2$ and $f(\text{Sr})_{\text{sol}} \leq 0.2$
481 in Figure 2. The inferred value for $\Delta^{137}\text{Ba}_{(\text{bac-sol})}$ (the offset between the cyanobacteria and the
482 solution) obtained from the two experimental replicates (referred to as R1 and R2) using eq. 4,
483 were $-0.25 \pm 0.03\text{\textperthousand}$ and $-0.28 \pm 0.10\text{\textperthousand}$, i.e. equal within uncertainty). For Sr, the inferred values of
484 $\Delta^{88}\text{Sr}_{(\text{bac-sol})}$ (the isotope enrichment factor between the cyanobacteria and the solution) were -0.40
485 $\pm 0.6\text{\textperthousand}$ and $-0.38 \pm 0.05\text{\textperthousand}$, i.e. also the same within error for both experimental replicates, R1 and
486 R2. Note, the large uncertainty in the $\Delta^{88}\text{Sr}_{(\text{bac-sol})}$ for replicate R1 is due to limited data points. For
487 experiment R2, the $\Delta^{88}\text{Sr}_{(\text{bac-sol})}$ value of $-0.38 \pm 0.05\text{\textperthousand}$ obtained using data at $0.2 \leq f(\text{Sr})_{\text{sol}} < 1$ (123
488 $\leq t \leq 480$) does not fit the experimental observations of the initial stage of Sr uptake ($0.88 \leq f(\text{Sr})_{\text{sol}}$
489 < 1 ; $123 < t < 291$ h; Figure 2 E). Such a difference between stages 1 and 2 could not be detected
490 in replicate R1, possibly because of a lack of data points corresponding to stage 1 (Figure 2D).
491 Initial data points of stage 1 of Sr uptake (i.e. $0.88 \leq f(\text{Sr})_{\text{sol}} < 1$; $123 < t < 291$ h) was better fitted
492 with a $\Delta^{88}\text{Sr}_{(\text{bac-sol})} = -0.17 \pm 0.04\text{\textperthousand}$ (shown as a dashed line in Figure 2E), which is lower in
493 magnitude than the $\Delta^{88}\text{Sr}_{(\text{bac-sol})}$ calculated for stage 2 ($-0.38 \pm 0.05\text{\textperthousand}$).

494 However, the decrease in $\delta^{88}\text{Sr}_{\text{sol}}$ and $\delta^{137}\text{Ba}_{\text{sol}}$ towards the end of their respective uptake
495 stages cannot be accounted for by a simple Rayleigh model (Figure 2). This decrease rather
496 suggests an exchange of Ba and Sr between the cells and the solution, eventually driving isotopic
497 equilibration between the cells and solution, with no apparent fractionation (i.e. $\Delta^{137}\text{Ba}_{(\text{bac-sol})}$ or
498 $\Delta^{88}\text{Sr}_{(\text{bac-sol})} \sim 0$) as can be seen in the Ba (experiment R1 and R2) and Sr (experiment R2). This
499 equilibration is achieved at ~300 h for Ba and ~550 h for Sr (Figure 2). The cause of the release of
500 the light isotopes of Ba and Sr from the cells back to the solution at the end of their respective
501 uptake stage can be discussed. As shown in Figure 2A, an increase in extracellular Ca concentration
502 is observed at 400 h. This increase might be indicative of partial dissolution of amorphous
503 carbonates, that may lead to the release of trapped Ca to the solution. Accordingly, some
504 amorphous carbonates inclusions seem to have a rugged/pitted aspect (Figure 3D and Figure 3G),
505 but it remains to be ascertained whether these features indeed result from dissolution. If so,
506 dissolution of amorphous carbonates may result in the release of some Ba and Sr within the cells,
507 thereby making these elements available for release back to the solution. The factors that could
508 cause such a dissolution of amorphous carbonate inclusions remain unclear. One possibility is that
509 switching between Ba and Sr uptake could be accompanied by cellular stress and/or shifts in the
510 AEE homeostasis. For instance, increased cell death due to accumulation of high concentration of
511 Ba and Sr, and/or disruption of processes involved in regulating intracellular pH during the switch
512 between Ba and Sr uptake, could favor the dissolution of amorphous carbonates. Future studies
513 aimed at tracking the lifetime of cells with respect to the incubation time may help in understanding
514 the link between the release of Ba and Sr and the toxicity of these elements for the cells.
515 Additionally, it would be interesting to assess whether the uptake of AEE parallel some changes in
516 the intracellular ionic strength and whether these changes in return may impact the uptake *versus*
517 release of these elements.

518 Alternatively, this marked decrease of $\delta^{88}\text{Sr}_{\text{sol}}$ and $\delta^{137}\text{Ba}_{\text{sol}}$ towards the end of the Sr and Ba uptake
519 stages can be modelled together with all other stages of the experiment using one single simple
520 mass balance dynamical model, referred to as the refined Rayleigh distillation model. To do so, we
521 consider two processes linking the solution and bacteria phases in the experiments. The first
522 process, termed as "uptake" hereafter, corresponds to the incorporation of the element from the
523 solution into the bacteria with the preferential incorporation of the lighter isotopes (^{134}Ba or ^{86}Sr in
524 the model). The preferential incorporation of the lighter isotopes is represented by the fractionation
525 factor (α) so that the incorporation of the heavier isotope occurs at a rate that is the rate of the
526 incorporation of the lighter isotope multiplied by the fractionation factor. The second process,
527 termed as exchange hereafter, contains two equal reactions (which have an identical rate), the
528 release of Ba and Sr from the bacteria to the solution (with no isotopic fractionation) and the equal
529 uptake of Ba and Sr (also with no isotopic fractionation) from the solution, which leads to a late
530 isotopic reequilibration between the solution and cells. Both the uptake and exchange processes
531 are modelled using first-order rate laws where the reaction rates are controlled by the rate constants
532 (k_{up} and k_{ex} respectively) and the concentration of the element of interest in the phase from which
533 the element is supplied. Consequently, the rate of uptake, i.e., formation of amorphous carbonates
534 is controlled by the amount of Ba and Sr in the solution, while the exchange reaction rate is
535 controlled by the amount of Ba and Sr in the bacteria.

536 The light stable isotope concentration ($^L[X]$) for the element of interest (X) is modelled using a
537 forward, discrete numerical scheme for the bacteria and solution phases using the following
538 equations (5–6):

539
$${}^L[X]_{bac_t} = {}^L[X]_{bac_{t-\Delta t}} + (k_{up} \times {}^L[X]_{sol_{t-\Delta t}}) - (k_{ex} \times {}^L[X]_{bac_{t-\Delta t}})$$

540
$$+ \left(\frac{R_{sol}}{(1 + R_{sol_{t-\Delta t}})} ((k_{ex} \times {}^H[X]_{bac_{t-\Delta t}}) + (k_{ex} \times {}^L[X]_{bac_{t-\Delta t}})) \right) \quad Eq (5)$$

541
$${}^L[X]_{sol_t} = {}^L[X]_{sol_{t-\Delta t}} - (k_{up} \times {}^L[X]_{sol_{t-\Delta t}}) + (k_{ex} \times {}^L[X]_{bac_{t-\Delta t}})$$

542
$$- \left(\frac{R_{sol}}{(1 + R_{sol_{t-\Delta t}})} ((k_{ex} \times {}^H[X]_{bac_{t-\Delta t}}) + (k_{ex} \times {}^L[X]_{bac_{t-\Delta t}})) \right) \quad Eq (6)$$

543 where the subscripts "bac" and "sol" denote the bacteria (bac) and solution phase, and t is the
 544 current timestep. R_{sol} is the ratio of the heavy isotope to the light isotope in the solution
 545 $(R_{sol} = \frac{{}^H[X]_{sol}}{{}^L[X]_{sol}}).$

546 The heavy stable isotope (${}^H[X]$) is also modelled using the same approach with the
 547 fractionation factor (α) included in the uptake rate term (equations 7–8).

548
$${}^H[X]_{bac_t} = {}^H[X]_{bac_{t-1}} + (\alpha \times k_{up} \times {}^H[X]_{sol_{t-1}}) - (k_{ex} \times {}^H[X]_{bac_{t-1}})$$

549
$$+ \left(\frac{1}{(1 + R_{sol_{t-\Delta t}})} ((k_{ex} \times {}^H[X]_{bac_{t-\Delta t}}) + (k_{ex} \times {}^L[X]_{bac_{t-\Delta t}})) \right) \quad Eq (7)$$

550
$${}^H[X]_{sol_t} = {}^H[X]_{sol_{t-1}} - (\alpha \times k_{up} \times {}^H[X]_{sol_{t-1}}) + (k_{ex} \times {}^H[X]_{bac_{t-1}})$$

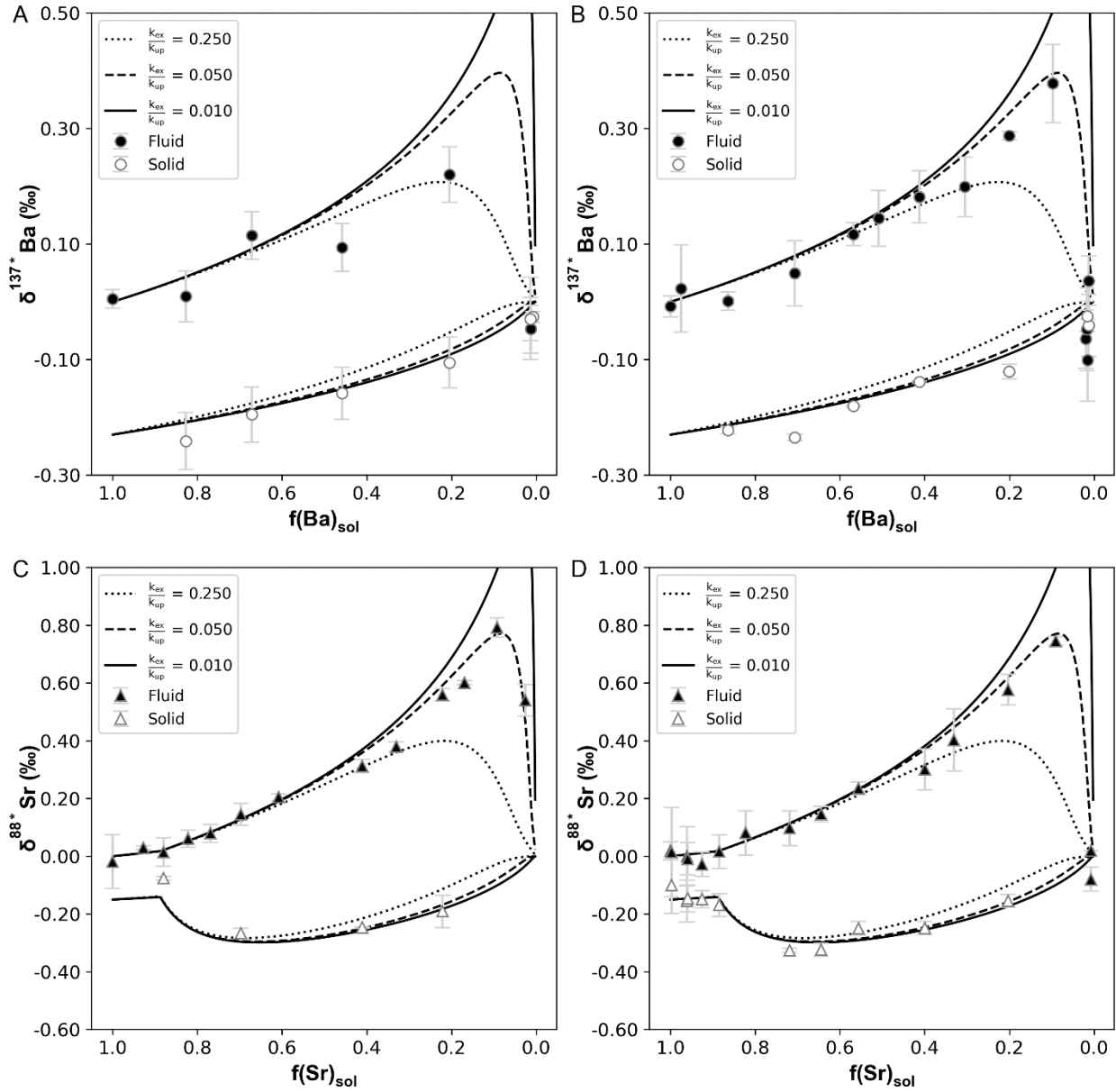
551
$$- \left(\frac{1}{(1 + R_{sol_{t-\Delta t}})} ((k_{ex} \times {}^H[X]_{bac_{t-\Delta t}}) + (k_{ex} \times {}^L[X]_{bac_{t-\Delta t}})) \right) \quad Eq (8)$$

552 For both isotopes, the initial concentrations (t=0) in the solutions are given by the initial
 553 element concentration and isotope ratio of the element of interest.

554 Figure 4 displays the evolution of the isotopic composition of the solution and cell fractions
555 as a function of the remaining element in solution using various, yet constant (with time) ratios of
556 uptake rate constant (k_{up}) to exchange rate constants (k_{ex}). In the early experimental stage, the Ba
557 or Sr elemental outflux is negligible with respect to uptake, meaning that the refined fractionation
558 model outlined above is effectively acting as a Rayleigh model with a unidirectional flux from
559 solution to bacteria with a constant isotope fractionation factor. A Ba isotope fractionation factor
560 of 0.99977 ($\Delta^{137}\text{Ba}_{(\text{bac-sol})} = -0.23\text{\textperthousand}$) was used for both replicates, in both the solution and cell
561 fractions. For Sr, the early uptake ($0.88 \leq f(\text{Sr})_{\text{sol}} < 1$; $123 < t < 291$ h) is modelled with a
562 fractionation factor of 0.99985 ($\Delta^{88}\text{Sr}_{(\text{bac-sol})} = -0.15\text{\textperthousand}$), while subsequently the uptake is assumed
563 to be characterized by a fractionation factor of 0.99954 ($\Delta^{88}\text{Sr}_{(\text{bac-sol})} = -0.46\text{\textperthousand}$). Using these
564 constraints for the isotope fractionation factors, a reasonable fit was achieved between the data and
565 the model for both Sr and Ba with a ratio $k_{\text{ex}}/k_{\text{up}} = 0.05$, i.e., the exchange rate constant is 5 % of
566 the uptake rate constant. With slower rates of exchange ($k_{\text{ex}}/k_{\text{up}} = 0.010$), the model produces a
567 trend similar to that of the Rayleigh model, until the fraction of the element remaining in solution
568 is less than 0.025. At this point, because of the first-order rate law used in our model (Eqs. 5–8),
569 the uptake rate slows down to the point where exchange equals uptake (Figure 4). Model results
570 based on the highest exchange rate show the largest deviation from the Rayleigh model, with a
571 significant impact of the isotopic composition of the solution after ~40 % of AEE removal from
572 the solution. However, at the beginning of the experiment all the parameter values produce trends
573 that are close to that of the Rayleigh model because the uptake process is dominant, while the
574 exchange process is negligible.

575

576



577

578
 579 **Figure 4.** Temporal evolution of the Ba (top) and Sr (bottom) stable isotope composition of the solution
 580 (\bullet for Ba and \blacktriangle for Sr) and bacteria (\circ for Ba and \triangle for Sr) fractions for two replicates (A—left
 581 column, B—right column) as a function of the fraction of the element remaining in the solution
 582 ($f(\text{element})_{\text{sol}}$). Error bars correspond to the analytical 2 SD. The black lines display the results of the
 583 combined uptake-exchange model with varying ratios (0.25—dotted, 0.05—dashed, 0.01—solid) for
 584 the rate constant for exchange (k_{ex}) versus the rate constant for uptake (k_{up}). Best fit values of
 585 $\alpha=0.99977$ and 0.99985 (0.99954 for the early stage) were selected for Ba and Sr, respectively.

585

586 The key difference between this modeling approach and the Rayleigh fractionation model
587 above is that the refined formulation includes the exchange of Ba and Sr towards the end of the
588 element uptake stage. In the improved formulation of the model, we assume that this exchange
589 occurs continuously all over the course of the experiment based on the amount of the element of
590 interest in the cell fraction. In reality, however, exchange might occur only after a certain time, for
591 example due to a change in cellular metabolic processes as mentioned above. Our approach is
592 unable to distinguish between these two scenarios as, by construction, the modeled exchange flux
593 of Ba and Sr at the beginning of the experiment is small as it is assumed to scale with the amount
594 of Ba or Sr in the cells. Nevertheless, the improved model drives to the conclusion that there is a
595 dynamic exchange of Ba and Sr isotopes between bacteria and solution, which is likely controlled
596 by the cells in response to Ba and Sr intracellular accumulation.

597 **4.2. Factors controlling Ba and Sr stable isotope fractionation by *G. lithophora***

598 Regardless of the exact mechanism under which Ba and Sr in cells are exchanged with the
599 solution during the later stage of our experiments, our data shows that initially *G. lithophora* is
600 enriched in the lighter isotopes relative to the solution for both Ba and Sr. This is consistent with
601 what has been observed for other marine calcifiers (e.g. Fietzke and Eisenhauer, 2006; Böhm et
602 al., 2012; Stevenson et al., 2014)) and inorganically precipitated carbonates (Mavromatis et al.,
603 2020). Several conceptual and numerical models have been proposed to understand isotope
604 fractionation of alkaline earth elements during crystal growth in inorganic systems. The “growth
605 entrapment model” (GEM) proposed by Watson and co-workers is based on the premise that the
606 thermodynamic properties of the near-surface region of a crystal differ from those of the bulk
607 (Watson, 2004). Accordingly, kinetic fractionation leads to a preferential incorporation of light
608 isotopes at the crystal surface. Then, an isotope equilibrium is slowly approached through ion

609 diffusion in the near surface region of the growing crystal. In this scenario, the higher the
610 precipitation rate, the shorter the time to reach isotope equilibrium. In any application of the GEM
611 model, the most uncertain input parameters are the near-surface diffusivity and the equilibrium
612 partition coefficient between the near-surface region and the bulk lattice. This limitation was
613 overcome in the surface reaction kinetic model (SRKM), which proposes that the isotope
614 fractionation is governed by the competition between the kinetics of crystal growth rate and ion
615 exchange between the mineral and solution (DePaolo, 2010). When the mineral growth rate
616 exceeds the rate of exchange of ions, the isotope composition tends towards kinetic limits; the
617 equilibrium fractionation is expressed only when the growth rate is much smaller than the exchange
618 rate. The SRKM has been previously used to describe the positive dependence of Ba and Sr isotope
619 fractionation on aragonite growth rate and calcite growth rate, respectively (AlKhatib and
620 Eisenhauer, 2017b; Mavromatis et al., 2020). The SRKM was further expanded into an ion-by-ion
621 growth model that allows for modeling isotope fractionation as a function of oversaturation and
622 solution stoichiometry, where low oversaturation or high Ca:CO₃ ion activity ratios will drive
623 isotope fractionation towards equilibrium limits and high oversaturation or low Ca:CO₃ ion activity
624 ratios will drive isotope fractionation towards the kinetic limit (Nielsen et al., 2012). Further, these
625 models were revised to include the effect of changes in surface speciation on isotope fractionation
626 (Wolthers et al., 2012; Watkins et al., 2013; Mills et al., 2021). While these models are able to
627 capture isotope fractionation dynamics during mineral growth in abiotic systems, their application
628 to biological isotope fractionation during biomineralization processes is complicated due to “vital”
629 effects that include biological control on ion transport, nucleation, growth, and mineral
630 transformation pathways that override the environmental controls (Weiner, 2003). Here, as a
631 tentative interpretation of the observed Ba and Sr isotope fractionation in the *G. lithophora*
632 cyanobacterium, we use the widely studied Ca isotope fractionation during intracellular

633 calcification in coccolithophores, a eukaryotic unicellular marine calcifier (Gussone et al., 2006).
634 This model involves (i) dehydration of Ca at the cell surface during the uptake of the ion, (ii)
635 subsequent rehydration within the cytoplasm, followed by (iii) removal of Ca via ion pump to cell
636 organelles for storage, to coccolith vesicles for calcification, or towards the outside of the cell to
637 maintain cellular homeostasis with respect to Ca. It is assumed that all the Ca entering the coccolith
638 vesicles is quantitatively precipitated within calcite, and thus that no Ca isotope fractionation
639 occurs during precipitation (Gussone et al., 2006; Stevenson et al., 2014). Therefore, isotope
640 fractionation in the coccolithophore model is proposed to occur prior to the mineral precipitation,
641 i.e., during cellular uptake/transport of Ca. Modeling studies have highlighted the influence of
642 parameters such as retention efficiency of the ion, rate of calcification, or rates of dehydration-
643 hydration on the isotope fractionation in coccolithophores (Mejía et al., 2018). The same model
644 could be applied in the case of Sr isotope fractionation by coccolithophores (Stevenson et al., 2014).

645 Application of the coccolithophore model to *G. lithophora* suggests that Ba and Sr
646 isotopes are predominantly fractionated at *G. lithophora* cell wall, i.e., at the point of dehydration
647 and influx/outflux of the ion. During cellular uptake, isotope fractionation happens due to the fact
648 that the lighter isotopes are dehydrated faster at the surface of the channel/transporter because of a
649 lower energy cost of bond breaking. As a result, it is expected that the final product will be enriched
650 in lighter isotopic species (DePaolo, 2010; Stevenson et al., 2014). The dehydration of the ion at
651 the channel/transporter entrance is in principle comparable with dehydration occurring at the
652 crystal surface observed in abiotic carbonates, since the latter process might resemble, from the
653 energetic point of view, the attachment of ion to molecules involved in uptake (Gussone et al.,
654 2006). Although fractionation during dehydration has not yet been quantified experimentally,
655 molecular dynamic calculations have simulated for solutions at infinite dilution a maximum

656 isotopic fractionation of both Ba and Sr of $-1.1\text{\textperthousand}$ upon dehydration (Hofmann et al., 2012). The
657 direction of the simulated Ba and Sr isotope fractionation as driven by dehydration dynamics agrees
658 with that measured here during Ba and Sr uptake by *G. lithophora* ($\Delta^{137}\text{Ba}_{(\text{bac-sol})} = -0.28\text{\textperthousand}$ to $-$
659 $0.23\text{\textperthousand}$; $\Delta^{88}\text{Sr}_{(\text{bac-sol})} = -0.46\text{\textperthousand}$ to $-0.38\text{\textperthousand}$), but its magnitude differs. Lower cellular enrichment in
660 light isotopes is possibly because the ions are not transported as free ions, but instead as much
661 heavier Ba- and Sr-aquocomplexes, suppressing the magnitude of isotope fractionation as proposed
662 by (Gussone et al., 2003). These complexes could be formed with ligands that are present in the
663 BG-11 growth medium (nitrate, chloride etc.). Complexation with ligands can impact isotope
664 fractionation depending on differences in the local bonding environment of the metal-ligand
665 complexes. As a general rule, heavier isotopes are relatively more stable having shorter, stronger
666 bonds for the same coordination. (AlKhatib and Eisenhauer, 2017b) hypothesized that depending
667 on the dominant Ca-complexes present in the solution (in their case $\text{Ca}^{2+}\text{-NH}_3$ complexes with
668 strong covalent character and $\text{Ca}^{2+}\text{-H}_2\text{O}$ complexes), apparent Ca isotope fractionation in calcite
669 could switch between equilibrium-like isotope fractionation and kinetic-like fractionation. In the
670 same study, Sr isotope fractionation in calcite did not follow a similar behavior, probably because
671 of Sr lower ionic potential based on its larger ionic radius, implying that solvation of Sr with water
672 molecules is more dominant than the formation of covalent bonding with NH_3 during solvation
673 (AlKhatib and Eisenhauer, 2017b). In this study, we cannot make predictions on the evolution of
674 the Ba and Sr aqueous speciation, due the absence of some solution chemistry parameters such as
675 carbonate alkalinity. Understanding the impact of these surface complexation effects on isotope
676 fractionation of Ba and Sr in *G. lithophora* cells could be an interesting future topic of study.

677 While dehydration of Ba and Sr during cellular uptake is so far the leading mechanism
678 attributed to cause isotope fractionation in biological systems, other mechanisms may also be at

679 play for *G. lithophora*. For instance, Mavromatis et al. (2017b) showed that the formation of abiotic
680 Mg-bearing ACC (Mg-ACC) results in the enrichment of the lighter isotope of Mg in the precipitate
681 relative to the fluid. If the formation of intracellular amorphous carbonate has a similar impact on
682 Ba and Sr isotope fractionation, it becomes an additional process contributing to the observed Ba
683 and Sr isotope fractionation measured during their uptake by *G. lithophora* cells. No experimental
684 or modeling studies of Ba or Sr isotope fractionation by abiotic precipitation of amorphous
685 carbonate have been performed so far. As a result, quantifying the relative contribution of Ba and
686 Sr dehydration *versus* amorphous carbonate formation on Ba and Sr isotope fractionation remains
687 an open question. Additionally, high-affinity cytosolic proteins could bind preferentially the
688 heavier isotopes of Ba and Sr, owing to their stronger binding strength relative to other complexing
689 agents present in the cytosol. Similar proteins have been suggested to bind Ca in coccolithophores
690 (Langer et al., 2006). However, so far nothing is known about the isotope fractionation caused by
691 such binding proteins, let alone their existence in *G. lithophora*. The mechanism(s) that cause the
692 elemental fractionation could also be responsible for causing the isotopic fractionation (Figure 2).
693 At this time, we do not know if these processes might be specific or not to *G. lithophora*, as such
694 an elemental selectivity and its origin require further research for other calcifying organisms..
695 These vital effects result from the biologically controlled formation of amorphous carbonates
696 including ion transport in the cell and eventually at the site of amorphous carbonate precipitation.
697 Future studies identifying the biochemical pathways enabling the observed elemental selectivity
698 will shed some light on the role of AEE uptake mechanisms on isotope fractionation.

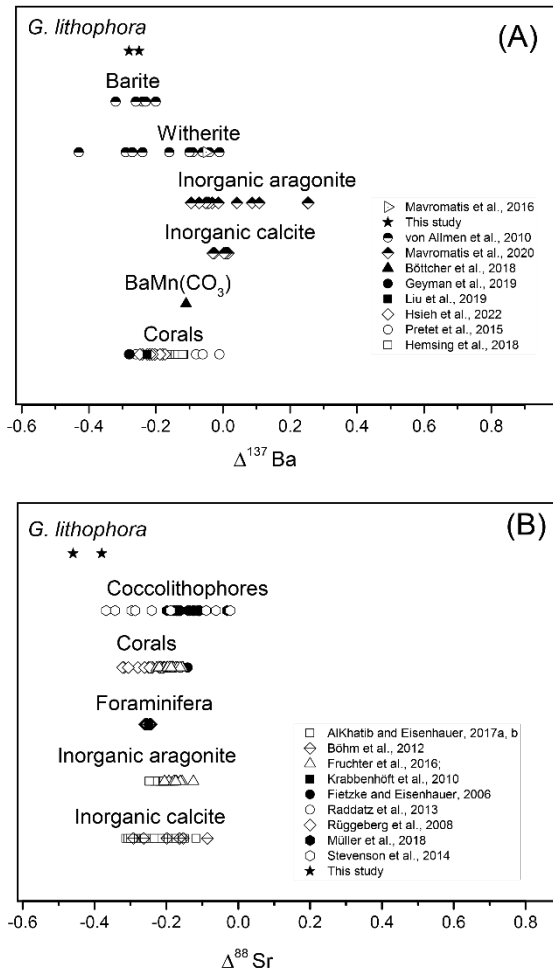
699 **4.3. Biogeochemical Implications**

700 The initial light isotope enrichment of Ba and Sr in cells of *G. lithophora* is consistent with that
701 observed for other biological and abiotic processes, but shows some differences (Figure 5). The

702 spread of $\Delta^{137}\text{Ba}_{(\text{bac-sol})}$ and $\Delta^{88}\text{Sr}_{(\text{bac-sol})}$ in *G. lithophora* ranges from $-0.28\text{\textperthousand}$ to $-0.25\text{\textperthousand}$ and $-0.46\text{\textperthousand}$ to $-0.38\text{\textperthousand}$ respectively. To put these values in context, Ba and Sr isotope fractionation factors for the biogenic carbonates (corals, coccolithophores, foraminifera) exhibit $\Delta^{88}\text{Sr}_{(\text{bac-sol})}$ ranging from $-0.37\text{\textperthousand}$ to $-0.022\text{\textperthousand}$ (Fietzke and Eisenhauer, 2006; Rüggeberg et al., 2008; Krabbenhöft et al., 2010; Böhm et al., 2012; Raddatz et al., 2013; Stevenson et al., 2014; Fruchter et al., 2016; Müller et al., 2018) and $\Delta^{137}\text{Ba}_{(\text{bac-sol})}$ ranging from $-0.28\text{\textperthousand}$ to $-0.01\text{\textperthousand}$ (Pretet et al., 2015; Hsieh and Henderson, 2017; Hemsing et al., 2018; Liu et al., 2019; Geyman et al., 2019). Abiogenic carbonates (calcite, aragonite, witherite) exhibit $\Delta^{88}\text{Sr}_{(\text{bac-sol})}$ ranging from $-0.313\text{\textperthousand}$ to $-0.086\text{\textperthousand}$ (Böhm et al., 2012; Fruchter et al., 2016; AlKhatib and Eisenhauer, 2017b, a) and $\Delta^{137}\text{Ba}_{(\text{bac-sol})}$ ranging from $-0.43\text{\textperthousand}$ to $0.25\text{\textperthousand}$ (von Allmen et al., 2010; Mavromatis et al., 2016, 2020; Böttcher et al., 2018). We note that the large spread in $\Delta^{137}\text{Ba}$ of witherite is due to its dependence on precipitation rates (von Allmen et al., 2010). Presently, the precipitation rate of the amorphous carbonate inclusions within *G. lithophora* cells is unknown and we do not know how to vary it, which prevents us from testing the existence of a relationship between isotope fractionation and precipitation rates. Nevertheless, this comparison raises an intriguing question about the use of the $\Delta^{137}\text{Ba}_{(\text{bac-sol})}$ and $\Delta^{88}\text{Sr}_{(\text{bac-sol})}$ of *G. lithophora* as an indicator for the presence of amorphous-carbonate-forming bacteria in the environment. This is of particular relevance given that *G. lithophora* is a deeply-rooted lineage in the cyanobacteria phylogenetic tree and the present-day closest relative of chloroplasts (Ponce-Toledo et al., 2017; Benzerara et al., 2022). Therefore, biomineralization of amorphous carbonates may be an ancient process but its geological record remains unexplored, in part due to lack of tracers of amorphous-carbonates-forming bacteria. However, the use of $\Delta^{137}\text{Ba}_{(\text{bac-sol})}$ and $\Delta^{88}\text{Sr}_{(\text{bac-sol})}$ of *G. lithophora* as indicators for the presence of amorphous carbonate forming bacteria in the environment is complicated for several reasons. Firstly, the Ba and Sr isotope composition of these bacteria is distinct from inorganic carbonates,

but similar to that observed in some other biogenic carbonates (Figure 5). This suggests that if geological carbonates could be screened for their Ba and Sr isotope compositions, the measurements may elucidate whether carbonates are biogenic in origin, but would not offer by itself a clue of their biological affiliation. Secondly, we observe that the initial kinetic isotope effect is overridden by isotope re-equilibration towards the end of element uptake stage, resulting in a close to zero Ba and Sr fractionation. Whether this behavior would apply to environmental conditions is not known. We argue that the observed isotope re-equilibration effect is due to the fact that the cultures were grown in a batch system, where there is a fixed supply of nutrients and elements. Under these constraints, as hypothesized in section 4.1, the isotope re-equilibration might be triggered by the sharp switch between Ba, Sr and Ca uptake because the extracellular Ba and Sr become exhausted at some time during the experiment. This phenomenon might be minimal in the environment where these bacteria live in an open system, and nutrients are likely continuously replenished. Moreover, the concentrations of Ba and Sr are considerably lower compared with those to which cells are exposed to in the batch system of the present study. For instance, Ba and Sr concentrations are typically between 0.01 and 18 µM in surface freshwater and 0.032–114 µM in seawater (Chowdhury and Blust, 2011; Peek and Clementz, 2012). The concentrations of dissolved Sr and Ba in Lake Alchichica, where *G. lithophora* was first observed, were in the nanomolar range (Couradeau et al., 2012). Overall, it is conceivable that the fractionations of Ba and Sr isotopes by *G. lithophora* in the environment are comparable to those measured in the batch system of the present study. Lastly, the use of Ba and Sr isotope compositions of *G. lithophora* as a biogenicity indicator requires that they are preserved during the transformation of amorphous carbonates upon cell death. Presently, there are no experimental studies validating or refuting this assumption. Interestingly, (Liu et al., 2020) provided some support to this hypothesis, as they showed that a high Mg content allows amorphous calcium carbonate (ACC) phases to transform

750 into Mg-calcite, preserving the trace element composition of the ACC precursor. This may suggest
751 that in some cases, Ba and Sr enrichment and their isotope composition may remain preserved upon
752 amorphous carbonate transformation. Future systematic measurements of Ba and Sr isotope
753 compositions in e.g., modern and ancient microbialites could yield some clues about the activity
754 of modern or past *G. lithophora*-like bacteria or other amorphous-carbonate-forming
755 cyanobacteria. How are these Ba and Sr isotope signatures altered or modified over geological time
756 scales remains an open question and beyond the scope of this study. Additionally, measurements
757 of Ca stable isotope fractionation during Ca uptake by amorphous-carbonate-forming
758 cyanobacteria could be a useful complement to the present study and open opportunities for the
759 development of a multi-isotope-based approach for tracking amorphous-carbonate-forming
760 bacteria in the geologic rock record.



761

762 **Figure 5: Comparison of $\Delta^{137}\text{Ba}_{(\text{bac-sol})}$ and $\Delta^{88}\text{Sr}_{(\text{bac-sol})}$ data between *G. lithophora* and other**
 763 **representative biogenic and abiotic carbonates and sulfates. The references for the published values**
 764 **reported in the figure are listed in the legend. All data are compiled as reported in these studies, with**
 765 **no averaging. In the studies by (Hemsing et al., 2018; Liu et al., 2019; Geyman et al., 2019; Hsieh et**
 766 **al., 2022), results were reported as $\Delta^{138}\text{Ba}$, and thus were converted to $\Delta^{137}\text{Ba}$ assuming exponential**
 767 **mass-dependent behavior ($\Delta^{138}\text{Ba} \approx 1.33 * \Delta^{137}\text{Ba}$) (van Zuilen et al., 2016). The datasets on corals**
 768 **obtained at varying temperatures, growth rates, and in different species, are all grouped under**
 769 **“corals”. The same treatment was applied for data on foraminifera, coccolithophores, inorganic**
 770 **calcite and aragonite. The $\Delta^{137}\text{Ba}_{(\text{bac-sol})}$ values of witherite precipitated at high temperatures (80°C)**
 771 **were not included in this data compilation.**

772

773

774 **5. CONCLUSIONS**

775 Barium and strontium stable isotope fractionations were measured in the Ba-Sr hyperaccumulating
776 cyanobacterium *G. lithophora*, which forms amorphous carbonate inclusions. The study was
777 motivated by the need to better understand the impact of bacteria forming amorphous carbonates
778 on Ba and Sr modern and past geochemical cycles, especially since (a) *G. lithophora* is the present-
779 day closest relative of chloroplasts (Ponce-Toledo et al., 2017) and (b) intracellular carbonate
780 biominerization is widespread in modern environments (Benzerara et al., 2014). The Ba and Sr
781 stable isotope measurements and STEM-EDXS analyses reveal that Ba and Sr net uptake by *G.*
782 *lithophora* is a dynamic process involving opposite fluxes, i.e., a forward reaction of Ba and Sr
783 uptake in *G. lithophora* vs a "back reaction" of exchange of Ba and Sr from the bacteria to the
784 extracellular solution. While the exact nature of the exchange reaction of Ba and Sr remains
785 unknown, hypotheses include the dissolution of Ba-Sr-enriched amorphous carbonate inclusions
786 in response to cellular stress of Ba and Sr accumulation, and/or disruption of cellular processes
787 involved in pH regulation. Nevertheless, the initial light isotope enrichment of Ba and Sr in *G.*
788 *lithophora* results in $\Delta^{137}\text{Ba}_{(\text{bac-sol})}$ and $\Delta^{88}\text{Sr}_{(\text{bac-sol})}$ values that may be used as tracers of bacteria
789 forming amorphous carbonates in the geological rock record. Similarly, these isotopic offsets may
790 be used to better measure the impact of amorphous-carbonate-forming bacteria on the
791 biogeochemical cycles of Ba and Sr in the environment, and thus should be integrated into future
792 models of Ba and Sr geochemical cycles, especially in environments dominated by these bacteria.

793 ACKNOWLEDGMENTS

794 This research was supported by European Research Council program under the direction of Karim
795 Benzerara (ERC under the European Community's Seventh Framework Programme FP7/2007-
796 2013 Grant Agreement no.307110 – ERC CALCYAN, PI: KB). Neha Mehta acknowledges the
797 Institute of Materials Science (iMAT) of the Alliance Sorbonne Université for a Post-Doc grant.

798 Parts of this work were supported by IPGP multidisciplinary program PARI, and by Paris–IdF
799 region SESAME Grant no. 12015908. We would also like to thank several instrumentation
800 facilities located at L'Institut de Minéralogie, de Physique des Matériaux et de
801 Cosmochimie (IMPMC, Paris, France) that enabled streamline measurement and analysis of
802 datasets presented in this work: Jean-Michel Guigner for STEM support. We thank GEMME
803 (geomicrobiology) facility for cyanobacterial culturing facilities. We thank Laure Cordier and
804 Pierre Burckel at Institut de Physique du Globe de Paris (IPGP, Paris, France) for ICP-OES and
805 ICP-MS analysis. Lastly, we thank the three anonymous reviewers and Nicola Allison for their
806 thorough comments and feedback on the manuscript.

807

808

809 **REFERENCES**

- 810 Abbass H. A. (2014) Calibrating Independent Component Analysis with Laplacian Reference for
811 Real-Time EEG Artifact Removal. *Neural Information Processing Lecture Notes in*
812 *Computer Science* **8836**, 68–75.
- 813 Achbergerová L. and Nahálka J. (2011) Polyphosphate - an ancient energy source and active
814 metabolic regulator. *Microbial Cell Factories* **10**, 1–14.
- 815 AlKhatib M. and Eisenhauer A. (2017a) Calcium and strontium isotope fractionation during
816 precipitation from aqueous solutions as a function of temperature and reaction rate; II.
817 Aragonite. *Geochimica et Cosmochimica Acta* **209**, 320–342.
- 818 AlKhatib M. and Eisenhauer A. (2017b) Calcium and strontium isotope fractionation in aqueous
819 solutions as a function of temperature and reaction rate; I. Calcite. *Geochimica et*
820 *Cosmochimica Acta* **209**, 296–319.
- 821 AlKhatib M., Qutob M., Alkhatib S. and Eisenhauer A. (2022) Strontium isotope fractionation
822 during precipitation of strontianite in aqueous solutions as a function of temperature and
823 reaction rate. *Chemical Geology* **587**, 120625.
- 824 von Allmen K., Böttcher M. E., Samankassou E. and Nägler T. F. (2010) Barium isotope
825 fractionation in the global barium cycle: First evidence from barium minerals and
826 precipitation experiments. *Chemical Geology* **277**, 70–77.
- 827 Altermann W., Kazmierczak J., Oren A. and Wright D. T. (2006) Cyanobacterial calcification and
828 its rock-building potential during 3.5 billion years of Earth history. *Geobiology* **4**, 147–166.
- 829 Amarouche-Yala S., Benouadah A., El Ouahab Bentabet A. and López-García P. (2014)
830 Morphological and phylogenetic diversity of thermophilic cyanobacteria in Algerian hot
831 springs. *Extremophiles* **18**, 1035–1047.
- 832 Avigliano E., Pisonero J., Bouchez J., Pouilly M., Domanico A., Sánchez S., Clavijo C., Scarabotti
833 P., Facetti J. F., Caffetti J. D., del Rosso F. R., Llamazares Vegh S. and Volpedo A. V.
834 (2021) Otolith Sr/Ca ratio complements Sr isotopes to reveal fish migration in large basins
835 with heterogeneous geochemical landscapes. *Environmental Biology of Fishes* **104**, 277–
836 292.
- 837 Bates S. L., Hendry K. R., Pryer H. V., Kinsley C. W., Pyle K. M., Woodward E. M. S. and Horner
838 T. J. (2017) Barium isotopes reveal role of ocean circulation on barium cycling in the
839 Atlantic. *Geochimica et Cosmochimica Acta* **204**, 286–299.
- 840 Benzerara K., Bolzoni R., Monteil C., Beyssac O., Forni O., Alonso B., Asta M. P. and Lefevre C.
841 (2021) The gammaproteobacterium *Achromatium* forms intracellular amorphous calcium
842 carbonate and not (crystalline) calcite. *Geobiology* **19**, 199–213.

- 843 Benzerara K., Duprat E., Bitard-Feildel T., Caumes G., Cassier-Chauvat C., Chauvat F., Dezi M.,
844 Diop S. I., Gaschignard G., Görgen S., Gugger M., López-García P., Millet M., Skouri-
845 Panet F., Moreira D. and Callebaut I. (2022) A New Gene Family Diagnostic for
846 Intracellular Biomineralization of Amorphous Ca Carbonates by Cyanobacteria. *Genome*
847 *biology and evolution* **14**, 1–16.
- 848 Benzerara K., Skouri-Panet F., Li J., Ferard C., Gugger M., Laurent T., Couradeau E., Ragon M.,
849 Cosmidis J., Menguy N., Margaret-Oliver I., Tavera R., Lopez-Garcia P. and Moreira D.
850 (2014) Intracellular Ca-carbonate biomineralization is widespread in cyanobacteria.
851 *Proceedings of the National Academy of Sciences* **111**, 10933–10938.
- 852 Blondeau M., Benzerara K., Ferard C., Guigner J. M., Poinsot M., Coutaud M., Tharaud M.,
853 Cordier L. and Skouri-Panet F. (2018a) Impact of the cyanobacterium *Gloeomargarita*
854 *lithophora* on the geochemical cycles of Sr and Ba. *Chemical Geology* **483**, 88–97.
- 855 Blondeau M., Sachse M., Boulogne C., Gillet C., Guigner J.-M., Skouri-Panet F., Poinsot M.,
856 Ferard C., Miot J. and Benzerara K. (2018b) Amorphous Calcium Carbonate Granules
857 Form Within an Intracellular Compartment in Calcifying Cyanobacteria. *Frontiers in*
858 *Microbiology* **9**, 1–14.
- 859 Böhm F., Eisenhauer A., Tang J., Dietzel M., Krabbenhöft A., Kisakürek B., Horn C., Kisaku B.
860 and Horn C. (2012) Strontium isotope fractionation of planktic foraminifera and inorganic
861 calcite. *Geochimica et Cosmochimica Acta* **93**, 300–314.
- 862 Böttcher M. E., Neubert N., von Allmen K., Samankassou E. and Nägler T. F. (2018) Barium
863 isotope fractionation during the experimental transformation of aragonite to witherite and
864 of gypsum to barite, and the effect of ion (de)solvation. *Isotopes in Environmental and*
865 *Health Studies* **54**, 324–335.
- 866 Bradley J. A., Daille L. K., Trivedi C. B., Bojanowski C. L., Stamps B. W., Stevenson B. S., Nunn
867 H. S., Johnson H. A., Loyd S. J., Berelson W. M., Corsetti F. A. and Spear J. R. (2017) Carbonate-rich dendrolitic cones: Insights into a modern analog for incipient microbialite
868 formation, Little Hot Creek, Long Valley Caldera, California. *npj Biofilms and*
869 *Microbiomes* **3**, 1–11.
- 870 Bridgestock L., Hsieh Y. T., Porcelli D., Homoky W. B., Bryan A. and Henderson G. M. (2018)
871 Controls on the barium isotope compositions of marine sediments. *Earth and Planetary*
872 *Science Letters* **481**, 101–110.
- 873 Bullen T. and Chadwick O. (2016) Ca , Sr and Ba stable isotopes reveal the fate of soil nutrients
874 along a tropical climosequence in Hawaii. *Chemical Geology* **422**, 25–45.
- 875 Cam N., Benzerara K., Georgelin T., Jaber M., Lambert J. F., Poinsot M., Skouri-Panet F. and
876 Cordier L. (2016) Selective Uptake of Alkaline Earth Metals by Cyanobacteria Forming
877 Intracellular Carbonates. *Environmental Science and Technology* **50**, 11654–11662.
- 878 Cam N., Benzerara K., Georgelin T., Jaber M., Lambert J. F., Poinsot M., Skouri-Panet F., Moreira
879 D., López-García P., Raimbault E., Cordier L. and Jézéquel D. (2018) Cyanobacterial

- 881 formation of intracellular Ca-carbonates in undersaturated solutions. *Geobiology* **16**, 49–
882 61.
- 883 Cam N., Georgelin T., Jaber M., Lambert J. F. and Benzerara K. (2015) In vitro synthesis of
884 amorphous Mg-, Ca-, Sr- and Ba-carbonates: What do we learn about intracellular
885 calcification by cyanobacteria? *Geochimica et Cosmochimica Acta* **161**, 36–49.
- 886 Cao Z., Li Y., Rao X., Yu Y., Hathorne E. C., Siebert C., Dai M. and Frank M. (2020) Constraining
887 barium isotope fractionation in the upper water column of the South China Sea. *Geochimica*
888 *et Cosmochimica Acta* **288**, 120–137.
- 889 Cao Z., Siebert C., Hathorne E. C., Dai M. and Frank M. (2016) Constraining the oceanic barium
890 cycle with stable barium isotopes. *Earth and Planetary Science Letters* **434**, 1–9.
- 891 Cavannaugh J., Whittaker M. L. and Joester D. (2019) Crystallization kinetics of amorphous calcium
892 carbonate in confinement. *Chemical Science*, 5039–5043.
- 893 Charbonnier Q., Bouchez J., Gaillardet J. and Gayer É. (2020) Barium stable isotopes as a
894 fingerprint of biological cycling in the Amazon River basin. *Biogeosciences* **17**, 5989–
895 6015.
- 896 Charbonnier Q., Bouchez J., Gaillardet J., Gayer E. and Porder S. (2022) A global imbalance in
897 potassium and barium river export: the result of biological uptake? *Geochemical*
898 *Perspectives Letters* **21**, 32–36.
- 899 Charbonnier Q., Moynier F. and Bouchez J. (2018) Barium isotope cosmochemistry and
900 geochemistry. *Science Bulletin* **63**, 385–394.
- 901 Cosmidis J. and Benzerara K. (2022) Why do microbes make minerals? *Comptes Rendus*
902 *Géoscience Planète* **34**, 1–39.
- 903 Couradeau E., Benzerara K., Gérard E., Moreira D., Bernard S., Brown G. E. Jr. and López-García
904 P. (2012) An Early-Branching Microbialite Cyanobacterium Forms Intracellular
905 Carbonates. *Science* **336**, 459–462.
- 906 Cusack M. and Freer A. (2008) Biomineralization: Elemental and organic influence in carbonate
907 systems. *Chemical Reviews* **108**, 4433–4454.
- 908 De Laeter J. R., Böhlke J. K., De Bièvre P., Hidaka H., Peiser H. S., Rosman K. J. R. and Taylor
909 P. D. P. (2003) Atomic weights of the elements: Review 2000 (IUPAC Technical Report).
910 *Pure and Applied Chemistry* **75**, 683–800.
- 911 DePaolo D. J. (2010) Surface kinetic model for isotopic and trace element fractionation during
912 precipitation of calcite from aqueous solution. *Geochimica et Cosmochimica Acta* **75**, 35–
913 43.
- 914 Dietzel M., Gussone N. and Eisenhauer A. (2004) Co-precipitation of Sr^{2+} and Ba^{2+} with aragonite
915 by membrane diffusion of CO_2 between 10 and 50 °C. *Chemical Geology* **203**, 139–151.

- 916 Evans D., Gray W. R., Rae J. W. B., Greenop R., Webb P. B., Penkman K., Kröger R. and Allison
917 N. (2020) Trace and major element incorporation into amorphous calcium carbonate (ACC)
918 precipitated from seawater. *Geochimica et Cosmochimica Acta* **290**, 293–311.
- 919 Fietzke J. and Eisenhauer A. (2006) Determination of temperature-dependent stable strontium
920 isotope ($^{88}\text{Sr}/^{86}\text{Sr}$) fractionation via bracketing standard MC-ICP-MS. *Geochemistry,*
921 *Geophysics, Geosystems* **7**, 1–6.
- 922 Fruchter N., Eisenhauer A., Dietzel M., Fietzke J., Böhm F., Montagna P., Stein M., Lazar B.,
923 Rodolfo-metalpa R. and Erez J. (2016) $^{88}\text{Sr}/^{86}\text{Sr}$ fractionation in inorganic aragonite and in
924 corals. *Geochimica et Cosmochimica Acta* **178**, 268–280.
- 925 Geyman B. M., Ptacek J. L., LaVigne M. and Horner T. J. (2019) Barium in deep-sea bamboo
926 corals: Phase associations, barium stable isotopes, & prospects for paleoceanography. *Earth*
927 and Planetary Science Letters **525**, 115751.
- 928 Gussone N., Eisenhauer A., Heuser A., Dietzel M., Bock B., Böhm F., Spero H. J., Lea D. W.,
929 Bijma J. and Nägler T. F. (2003) Model for kinetic effects on calcium isotope fractionation
930 ($\delta^{44}\text{Ca}$) in inorganic aragonite and cultured planktonic foraminifera. *Geochimica et*
931 *Cosmochimica Acta* **67**, 1375–1382.
- 932 Gussone N., Langer G., Geisen M., Steel B. A. and Riebesell U. (2007) Calcium isotope
933 fractionation in coccoliths of cultured *Calcidiscus leptoporus*, *Helicosphaera carteri*,
934 *Syracosphaera pulchra* and *Umbilicosphaera foliosa*. *Earth and Planetary Science Letters*
935 **260**, 505–515.
- 936 Gussone N., Langer G., Thoms S., Nehrke G., Eisenhauer A., Riebesell U. and Wefer G. (2006)
937 Cellular calcium pathways and isotope fractionation in *Emiliania huxleyi*. *Geology* **34**,
938 625–628.
- 939 Gustafsson J. P. (2012) Visual MINTEQ 3.0 user guide. *Dep.of Land & Water Resour.eng*, 1–73.
- 940 Hajj F., Poszwa A., Bouchez J. and Guérard F. (2017) Radiogenic and “stable” strontium isotopes
941 in provenance studies: A review and first results on archaeological wood from shipwrecks.
942 *Journal of Archaeological Science* **86**, 24–49.
- 943 Hemming F., Hsieh Y. T., Bridgestock L., Spooner P. T., Robinson L. F., Frank N. and Henderson
944 G. M. (2018) Barium isotopes in cold-water corals. *Earth and Planetary Science Letters*
945 **491**, 183–192.
- 946 Hofmann A. E., Bourg I. C. and DePaolo D. J. (2012) Ion desolvation as a mechanism for kinetic
947 isotope fractionation in aqueous systems. *Proceedings of the National Academy of Sciences*
948 *of the United States of America* **109**, 18689–18694.
- 949 Horner T. J., Kinsley C. W. and Nielsen S. G. (2015) Barium-isotopic fractionation in seawater
950 mediated by barite cycling and oceanic circulation. *Earth and Planetary Science Letters*
951 **430**, 511–522.

- 952 Hsieh Y. T. and Henderson G. M. (2017) Barium stable isotopes in the global ocean: Tracer of Ba
953 inputs and utilization. *Earth and Planetary Science Letters* **473**, 269–278.
- 954 Kellermeier M., Picker A., Kempter A., Cölfen H. and Gebauer D. (2014) A straightforward
955 treatment of activity in aqueous CaCO₃ solutions and the consequences for nucleation
956 theory. *Advanced Materials* **26**, 752–757.
- 957 Krabbenhöft A., Eisenhauer A., Böhm F., Vollstaedt H., Fietzke J., Liebetrau V., Augustin N.,
958 Peucker-Ehrenbrink B., Müller M. N., Horn C., Hansen B. T., Nolte N. and Wallmann K.
959 (2010) Constraining the marine strontium budget with natural strontium isotope
960 fractionations ($^{87}\text{Sr}/^{86}\text{Sr}^*$, $\delta^{88/86}\text{Sr}$) of carbonates, hydrothermal solutions and river waters.
961 *Geochimica et Cosmochimica Acta* **74**, 4097–4109.
- 962 Langer G., Gussone N., Nehrke G., Riebesell U., Eisenhauer A., Kuhnert H., Rost B., Trimborn S.,
963 and Thoms S. (2006) Coccolith strontium to calcium ratios in *Emiliania huxleyi*: The
964 dependence on seawater strontium and calcium concentrations. *Limnology and
965 Oceanography* **51**, 310–320.
- 966 Li J., Margaret Oliver I., Cam N., Boudier T., Blondeau M., Leroy E., Cosmidis J., Skouri-Panet
967 F., Guigner J.-M., Férand C., Poinsot M., Moreira D., Lopez-Garcia P., Cassier-Chauvat C.,
968 Chauvat F. and Benzerara K. (2016) Biomineralization Patterns of Intracellular
969 Carbonatogenesis in Cyanobacteria: Molecular Hypotheses. *Minerals* **6**, 10.
- 970 Liu Y., Li X., Zeng Z., Yu H.-M., Huang F., Felis T. and Shen C.-C. (2019) Annually-resolved
971 coral skeletal $\delta^{138/134}\text{Ba}$ records: A new proxy for oceanic Ba cycling. *Geochimica et
972 Cosmochimica Acta* **247**, 27–39.
- 973 Liu Z., Zhang Z., Wang Z., Jin B., Li D., Tao J., Tang R. and de Yoreo J. J. (2020) Shape-preserving
974 amorphous-to-crystalline transformation of CaCO₃ revealed by in situ TEM. *Proceedings
975 of the National Academy of Sciences of the United States of America* **117**, 3397–3404.
- 976 Loste E., Wilson R. M., Seshadri R. and Meldrum F. C. (2003) The role of magnesium in stabilising
977 amorphous calcium carbonate and controlling calcite morphologies. *Journal of Crystal
978 Growth* **254**, 206–218.
- 979 Martignier A., Filella M., Pollok K., Melkonian M., Bensimon M., Barja F., Langenhorst F., Jaquet
980 J. M. and Ariztegui D. (2018) Marine and freshwater micropearls: Biomineralization
981 producing strontium-rich amorphous calcium carbonate inclusions is widespread in the
982 genus *Tetraselmis* (Chlorophyta). *Biogeosciences* **15**, 6591–6605.
- 983 Martignier A., Pacton M., Filella M., Jaquet J. M., Barja F., Pollok K., Langenhorst F., Lavigne S.,
984 Guagliardo P., Kilburn M. R., Thomas C., Martini R. and Ariztegui D. (2017) Intracellular
985 amorphous carbonates uncover a new biomineralization process in eukaryotes. *Geobiology*
986 **15**, 240–253.
- 987 Mavromatis V., Immenhauser A., Buhl D., Purgstaller B., Baldermann A. and Dietzel M. (2017a)
988 Effect of organic ligands on Mg partitioning and Mg isotope fractionation during low-

- 989 temperature precipitation of calcite in the absence of growth rate effects. *Geochimica et*
990 *Cosmochimica Acta* **207**, 139–153.
- 991 Mavromatis V., Purgstaller B., Dietzel M., Buhl D., Immenhauser A. and Schott J. (2017b) Impact
992 of amorphous precursor phases on magnesium isotope signatures of Mg-calcite. *Earth and*
993 *Planetary Science Letters* **464**, 227–236.
- 994 Mavromatis V., van Zuilen K., Blanchard M., van Zuilen M., Dietzel M. and Schott J. (2020)
995 Experimental and theoretical modelling of kinetic and equilibrium Ba isotope fractionation
996 during calcite and aragonite precipitation. *Geochimica et Cosmochimica Acta* **269**, 566–
997 580.
- 998 Mavromatis V., van Zuilen K., Purgstaller B., Baldermann A., Nägler T. F. and Dietzel M. (2016)
999 Barium isotope fractionation during witherite (BaCO_3) dissolution, precipitation and at
1000 equilibrium. *Geochimica et Cosmochimica Acta* **190**, 72–84.
- 1001 Mehta N., Bougoure J., Kocar B. D., Duprat E. and Benzerara K. (2022) Cyanobacteria
1002 Accumulate Radium (^{226}Ra) within Intracellular Amorphous Calcium Carbonate
1003 Inclusions. *ACS ES&T Water* **2**, 616–623.
- 1004 Meibom A., Cuif J. P., Houlbreque F., Mostefaoui S., Dauphin Y., Meibom K. L. and Dunbar R.
1005 (2008) Compositional variations at ultra-structure length scales in coral skeleton.
1006 *Geochimica et Cosmochimica Acta* **72**, 1555–1569.
- 1007 Mejía L. M., Paytan A., Eisenhauer A., Böhm F., Kolevica A., Bolton C., Méndez-Vicente A.,
1008 Abrevaya L., Isensee K. and Stoll H. (2018) Controls over $\delta^{44}\text{Ca}/^{40}\text{Ca}$ and Sr/Ca variations
1009 in coccoliths: New perspectives from laboratory cultures and cellular models. *Earth and*
1010 *Planetary Science Letters* **481**, 48–60.
- 1011 Meynadier L., Gorge C., Birck J. L. and Allègre C. J. (2006) Automated separation of Sr from
1012 natural water samples or carbonate rocks by high performance ion chromatography.
1013 *Chemical Geology* **227**, 26–36.
- 1014 Middelburg J. J., Soetaert K. and Hagens M. (2020) Ocean Alkalinity, Buffering and
1015 Biogeochemical Processes. *Rev. Geophys.* **58**.
- 1016 Mills J. V., DePaolo D. J. and Lammers L. N. (2021) The influence of Ca:CO₃ stoichiometry on
1017 Ca isotope fractionation: Implications for process-based models of calcite growth.
1018 *Geochimica et Cosmochimica Acta* **298**, 87–111.
- 1019 Monteil C. L., Benzerara K., Menguy N., Bidaud C. C., Michot-Achdjian E., Bolzoni R., Mathon
1020 F. P., Coutaud M., Alonso B., Garau C., Jézéquel D., Viollier E., Ginet N., Floriani M.,
1021 Swaraj S., Sachse M., Busigny V., Duprat E., Guyot F. and Lefevre C. T. (2021)
1022 Intracellular amorphous Ca-carbonate and magnetite biomineralization by a magnetotactic
1023 bacterium affiliated to the Alphaproteobacteria. *ISME Journal* **15**, 1–18.
- 1024 Moreira D., Tavera R., Benzerara K., Skouri-Panet F., Couradeau E., Gérard E., Fonta C. L.,
1025 Novelo E., Zivanovic Y. and López-García P. (2017) Description of *Gloeo-margarita*

- 1026 *lithophora* gen. nov., sp. nov., a thylakoid-bearing, basal-branching cyanobacterium with
1027 intracellular carbonates, and proposal for Gloeomargaritales ord. nov. *International*
1028 *Journal of Systematic and Evolutionary Microbiology* **67**, 653–658.
- 1029 Müller M. N., Krabbenhöft A., Vollstaedt H., Brandini F. P. and Eisenhauer A. (2018) Stable
1030 isotope fractionation of strontium in coccolithophore calcite: Influence of temperature and
1031 carbonate chemistry. *Geobiology* **16**, 297–306.
- 1032 Nielsen L. C., DePaolo D. J. and De Yoreo J. J. (2012) Self-consistent ion-by-ion growth model
1033 for kinetic isotopic fractionation during calcite precipitation. *Geochimica et Cosmochimica
1034 Acta* **86**, 166–181.
- 1035 Paytan A., Griffith E. M., Eisenhauer A., Hain M. P., Wallmann K. and Ridgwell A. (2021) A 35-
1036 million-year record of seawater stable Sr isotopes reveals a fluctuating global carbon cycle.
1037 *Science* **371**, 1346–1350.
- 1038 Ponce-Toledo R. I., Deschamps P., López-García P., Zivanovic Y., Benzerara K. and Moreira D.
1039 (2017) An Early-Branching Freshwater Cyanobacterium at the Origin of Plastids. *Current
1040 Biology* **27**, 386–391.
- 1041 Pretet C., Zuilen K., Nägler T. F., Reynaud S., Böttcher M. E. and Samankassou E. (2015)
1042 Constraints on barium isotope fractionation during aragonite precipitation by corals. *The
1043 Depositional Record* **1**, 118–129.
- 1044 Raddatz J., Liebetrau V., Rüggeberg A., Hathorne E., Krabbenhöft A., Eisenhauer A., Böhm F.,
1045 Vollstaedt H., Fietzke J., Correa M. L., Freiwald A. and Dullo W. (2013) Stable Sr-isotope
1046 , Sr/Ca , Mg/Ca , Li/Ca and Mg / Li ratios in the scleractinian cold-water coral *Lophelia*
1047 pertusa. *Chemical Geology* **352**, 143–152.
- 1048 Ragon M., Benzerara K., Moreira D., Tavera R. and Lopez-Garcia P. (2014) 16S rDNA-based
1049 analysis reveals cosmopolitan occurrence but limited diversity of two cyanobacterial
1050 lineages with contrasted patterns of intracellular carbonate mineralization. *Frontiers in
1051 Microbiology* **5**, 1–11.
- 1052 Riding R. (2006) Cyanobacterial calcification, carbon dioxide concentrating mechanisms, and
1053 Proterozoic-Cambrian changes in atmospheric composition. *Geobiology* **4**, 299–316.
- 1054 Rodriguez-Blanco J. D., Shaw S. and Benning L. G. (2011) The kinetics and mechanisms of
1055 amorphous calcium carbonate (ACC) crystallization to calcite, via vaterite. *Nanoscale* **3**,
1056 265–271.
- 1057 Romaniello S. J., Field M. P., Smith H. B., Gordon G. W., Kim M. H. and Anbar A. D. (2015)
1058 Fully automated chromatographic purification of Sr and Ca for isotopic analysis. *Journal
1059 of Analytical Atomic Spectrometry* **30**, 1906–1912.
- 1060 Rüggeberg A., Fietzke J., Liebetrau V., Eisenhauer A., Dullo W. C. and Freiwald A. (2008) Stable
1061 strontium isotopes ($\delta^{88/86}\text{Sr}$) in cold-water corals - A new proxy for reconstruction of
1062 intermediate ocean water temperatures. *Earth and Planetary Science Letters* **269**, 570–575.

- 1063 Russell W. A., Papanastassiou D. A. and Tombrello T. A. (1978) Ca isotope fractionation on the
1064 Earth and other solar system materials. *Geochimica et Cosmochimica Acta* **42**, 1075–1090.
- 1065 Souza G. F. D., Reynolds B. C., Kiczka M. and Bourdon B. (2010) Evidence for mass-dependent
1066 isotopic fractionation of strontium in a glaciated granitic watershed. *Geochimica et*
1067 *Cosmochimica Acta* **74**, 2596–2614.
- 1068 Stanier R. Y., Deruelles J., Rippka R., Herdman M. and Waterbury J. B. (1979) Generic
1069 Assignments, Strain Histories and Properties of Pure Cultures of Cyanobacteria.
1070 *Microbiology* **111**, 1–61.
- 1071 Stephens C. J., Ladden S. F., Meldrum F. C. and Christenson H. K. (2010) Biomineralization:
1072 Amorphous Calcium Carbonate is Stabilized in Confinement. *Advanced Functional*
1073 *Materials* **20**, n/a-n/a.
- 1074 Stevenson E. I., Hermoso M., Rickaby R. E. M., Tyler J. J., Minoletti F., Parkinson I. J., Mokadem
1075 F. and Burton K. W. (2014) Controls on stable strontium isotope fractionation in
1076 coccolithophores with implications for the marine Sr cycle. *Geochimica et Cosmochimica*
1077 *Acta* **128**, 225–235.
- 1078 Tasker T. L., Piotrowski P. K., Dorman F. L. and Burgos W. D. (2016) Metal Associations in
1079 Marcellus Shale and Fate of Synthetic Hydraulic Fracturing Fluids Reacted at High
1080 Pressure and Temperature. *Environmental Engineering Science* **33**, 753–765.
- 1081 Teng F.-Z., Dauphas N. and Watkins J. M. (2017) Non-Traditional Stable Isotopes: Retrospective
1082 and Prospective. *Reviews in Mineralogy and Geochemistry* **82**, 1–26.
- 1083 Tesoriero J. A. and Pankow F. J. (1996) Solid solution partitioning of Sr, Ba and Cd to calcite.
1084 *Geochimica et Cosmochimica Acta* **60**, 1053–1063.
- 1085 Ulrich R. N., Guillermic M., Campbell J., Hakim A., Han R., Singh S., Stewart J. D., Román-
1086 Palacios C., Carroll H. M., De Corte I., Gilmore R. E., Doss W., Tripati A., Ries J. B. and
1087 Eagle R. A. (2021) Patterns of Element Incorporation in Calcium Carbonate Biominerals
1088 Recapitulate Phylogeny for a Diverse Range of Marine Calcifiers. *Frontiers in Earth*
1089 *Science* **9**, 1–26.
- 1090 Vollstaedt H., Eisenhauer A., Wallmann K., Böhm F., Fietzke J., Liebetrau V., Krabbenhöft A.,
1091 Farkaš J., Tomašových A., Raddatz J. and Veizer J. (2014) The Phanerozoic $\delta^{88}/^{86}\text{Sr}$ record
1092 of seawater: New constraints on past changes in oceanic carbonate fluxes. *Geochimica et*
1093 *Cosmochimica Acta* **128**, 249–265.
- 1094 Watkins J. M., Nielsen L. C., Ryerson F. J. and DePaolo D. J. (2013) The influence of kinetics on
1095 the oxygen isotope composition of calcium carbonate. *Earth and Planetary Science Letters*
1096 **375**, 349–360.
- 1097 Watson E. B. (2004) A conceptual model for near-surface kinetic controls on the trace- element
1098 and stable isotope composition of abiogenic calcite crystals. *Geochimica et Cosmochimica*
1099 *Acta* **68**, 1473–1488.

- 1100 Wei W., Zeng Z., Shen J., Tian L.-L., Wei G.-Y., Ling H.-F. and Huang F. (2021) Dramatic
1101 changes in the carbonate-hosted barium isotopic compositions in the Ediacaran Yangtze
1102 Platform. *Geochimica et Cosmochimica Acta* **299**, 113–129.
- 1103 Weiner S. (2003) An Overview of Biomineralization Processes and the Problem of the Vital Effect.
1104 *Reviews in Mineralogy and Geochemistry* **54**, 1–29.
- 1105 Wolthers M., Nehrke G., Gustafsson J. P. and Van Cappellen P. (2012) Calcite growth kinetics:
1106 Modeling the effect of solution stoichiometry. *Geochimica et Cosmochimica Acta* **77**, 121–
1107 134.
- 1108 Zhang F., Frýda J., Fakhraee M., Lin Y., Wei G.-Y., Cao M., Li N., Zhou J., Frýdová B., Wei H.
1109 and Shen S. (2022) Marine anoxia as a trigger for the largest Phanerozoic positive carbon
1110 isotope excursion: Evidence from carbonate barium isotope record. *Earth and Planetary
1111 Science Letters* **584**, 117421.
- 1112 van Zuilen K., Nägler T. F. and Bullen T. D. (2016) Barium Isotopic Compositions of Geological
1113 Reference Materials. *Geostandards and Geoanalytical Research* **40**, 543–558.
- 1114

Supplementary Material

Barium and strontium isotope fractionation during their uptake by cyanobacteria forming intracellular carbonates

Neha Mehta¹, Margot Coutaud¹, Julien Bouchez², Kirsten van Zuilen^{2,3}, Harold J. Bradbury^{4,5}, Frederic Moynier², Caroline Gorge², Feriel Skouri-Panet¹ and Karim Benzerara^{1*}

¹Sorbonne Université, Muséum National d'Histoire Naturelle, UMR CNRS 7590. Institut de Minéralogie, de Physique des Matériaux et de Cosmochimie (IMPMC), 4 Place Jussieu, 75005 Paris, France.

²Université Paris Cité, Institut de physique du globe de Paris (IPGP), CNRS, F-75005 Paris, France

³Shell Global Solutions International B.V., Grasweg 31, 1031 HW Amsterdam, The Netherlands

⁴Department of Earth Sciences, University of Cambridge, Cambridge, CB2 3EQ, UK

⁵Department of Earth, Ocean and Atmospheric Sciences, University of British Columbia, 2020-2207 Main Mall, Vancouver, British Columbia, V6T 1Z4, Canada.

*Corresponding author: karim.benzerara@sorbonne-universite.fr

Table S1: Composition of BG-11

Table S2: Saturation index of possible phases that could form in the initial growth medium

Table S3: Matrix effect

Table S4: Isotope offsets

Table S5: Barium isotope measurement in in-house standards

Table S6: Barium isotope balance

Table S7: Numeric data for OD

Table S8: Concentration of Ba, Sr and Ca in inoculated samples

Table S9: Ba isotope numerical values

Table S10: Sr isotope numerical values

Table S11: EDXS spectra in numeric format

Table S12: Three isotope plot

Table S13: Concentration of Ba, Sr, and Ca in non-inoculated sample

Figure S1: Yield of acid digestion procedure.

Figure S2: Three-isotope plot ($\delta^{88}\text{Sr}$ vs $\delta^{84}\text{Sr}$ and $\delta^{88}\text{Sr}$ vs $\delta^{87}\text{Sr}$) showing the absence of uncorrected interference

Figure S3: pH of cultures and control

Figure S4: Ba, Sr mass balance in cultures

Figure S5: Ba, Sr and Ca concentrations in non-inoculated control

Table S1: Chemical composition of the growth solution (BG11 supplemented with Ba and Sr).

Parameter	Value	Unit
pH	7.8	unit of pH
[NaHCO ₃]	0.48	mM
[Sr ²⁺]	0.250	mM
[Ba ²⁺]	0.250	mM
[Ca ²⁺]	0.250	mM
[Na ⁺]	18.1	mM
[Mg ²⁺]	0.302	mM
[K ⁺]	0.365	mM
[NO ₃ ⁻]	17.7	mM
[Cl ⁻]	1.5	mM
[CO ₃ ²⁻]	0.380	mM
[SO ₄ ²⁻]	0.301	mM
[PO ₄ ³⁻]	0.180	mM
[NH ₄ ⁺]	90.0	µM
[Fe ³⁺]	30.0	µM
[Mn ²⁺]	9.1	µM
[Cu ²⁺]	0.3	µM
[Zn ²⁺]	0.8	µM
[Co ²⁺]	0.2	µM
[BO ₃ ⁻]	46.3	µM
[MoO ₄ ⁴⁻]	1.6	µM

Table S2: Estimated saturation indices based on Visual MINTEQ for Ca, Ba and Sr phases and ACC in the initial growth medium (Table S1). See text for details for Visual MINTEQ calculations.

	saturation index	Mineral formula
Anhydrite	-3,328	<chem>CaSO4</chem>
Aragonite	-1,479	<chem>CaCO3</chem>
Barite	2,21	<chem>BaSO4</chem>
Calcite	-1,339	<chem>CaCO3</chem>
Celestite	-1,091	<chem>SrSO4</chem>
Dolomite	-2,398	<chem>Ca(Mg)(CO3)2</chem>
Gypsum	-3,102	<chem>CaSO4</chem>
Hydroxyapatite	6,635	<chem>Ca5(PO4)3OH</chem>
ACC	-1,96	<chem>CaCO3</chem>
Strontianite	-0,572	<chem>SrCO3</chem>
Witherite	-1,279	<chem>BaCO3</chem>

Table S3: Evaluation of the matrix effect on the $\delta^{88}\text{Sr}$ values through doping experiment on the SRM 987 Sr reference material

Chromatography	Matrix	Initial Sr concentration μM	$\delta^{88}\text{Sr} (\text{\textperthousand})$	
			value	2sd
Automatic	EDTA (2.4 μM)*	262	0.08	0.06
		126	-0.02	0.04
		23	0.02	-0.02
	Citrate (30 μM)†	262	0.04	-0.07
		126	-0.02	-0.01
		23	-0.03	0.02
	BG11 medium	262	-0.03	0.05
		126	0.01	-0.04
		23	0.048	-0.006
Manual	HNO_3 (0.5 M)	6	0.00	0.01
			0.01	0.02
	BG11 medium	262	0.00	0.01
			0.00	0.02
		126	-0.014	0.004
			-0.01	0.03
		23	0.015	0.005
			0.01	0.01

* 2.4 μM EDTA ($\text{C}_{10}\text{H}_{12}\text{K}_2\text{MgN}_2\text{O}_8 \cdot 2 \text{H}_2\text{O}$)

† 30 μM citrate ($\text{Fe(III)}(\text{NH}_4)_3$ citrate)

Table S4: Results of the isotope mass balance between the measured $\delta^{88}\text{Sr}$ of the bulk fraction and the $\delta^{88}\text{Sr}$ calculated from the Sr-weighted sum of the solution and bacteria fraction ($\delta^{88}\text{Sr}_{\text{sol}}$, $\delta^{88}\text{Sr}_{\text{bac}}$).

Replicate	Time (h)	Measured $\delta^{88}\text{Sr}_{\text{bulk}}$ (‰)		Calculated $\delta^{88}\text{Sr}_{\text{bulk}}^{\dagger}$ (‰)		Difference (‰) ¹	
		value	2sd	value	2sd	value	2sd
R1	340	0.82	0.03	0.92	0.04	-0.09	0.05
	451	0.83	0.07	0.87	0.06	-0.04	0.09
	291	na		0.87	0.05	na	
	411	na		0.88	0.02	na	
	average	0.83	0.08	0.88	0.05	-0.06	0.09
R2	291	0.82	0.01	0.87	0.07	-0.05	0.07
	480	0.88	0.07	0.87	0.06	0.01	0.09
	123	na		0.881	0.02	na	
	162	na		0.84	0.05	na	
	195	na		0.9	0.2	na	
	258	na		0.85	0.07	na	
	361	na		0.87	0.06	na	
	385	na		0.86	0.04	na	
	411	na		0.90	0.03	na	
	428	na		0.86	0.07	na	
R1-R2	average	0.85	0.07	0.87	0.03	-0.02	0.07
	average	0.84	0.06	0.87	0.04	-0.04	0.07

[†]Calculated $\delta^{88}\text{Sr}_{\text{bulk}}$ derived from mass balance calculation with measured $\delta^{88}\text{Sr}_{\text{sol}}$ and $\delta^{88}\text{Sr}_{\text{bac}}$ values

¹ Measured $\delta^{88}\text{Sr}_{\text{bulk}} - \text{Calculated } \delta^{88}\text{Sr}_{\text{bulk}}$

na= not analyzed

Table S5: $\delta^{137}\text{Ba}$ values obtained for different reference materials (BCR-2, BHVO-1 and AGV-1 USGS international standards and two in-house references)

Standard	Description (origin)	$\delta^{137}\text{Ba}$ (‰) value	$\delta^{137}\text{Ba}$ (‰) 2sd	References
BHVO-1	Basalt (USGS)	0.03	0.06	our study
		0.03	0.04	van Zuilen <i>et al.</i> (2016) ¹
BCR-2	Basalt (USGS)	0.05	0.04	our study
		0.05	0.03	Nan <i>et al.</i> (2015) ²
AGV-1	Andesite (USGS)	0.01	0.02	our study
		0.06	0.04	van Zuilen <i>et al.</i> (2016) ¹
BaBe12*	In-house pure Ba solution	-1.16	0.04	our study
		-1.16	0.05	van Zuilen <i>et al.</i> (2016) ¹
BaBe27*	In-house pure Ba solution	-0.64	0.04	our study
		-0.62	0.05	van Zuilen <i>et al.</i> (2016) ¹

*The in-house BaBE12 and BaBe27 materials were artificially fractionated by Ba diffusion through a silica hydrogel and correspond to the dilution of G_1.0_25_12d_H2O and G_1.0_25_27d_H2O samples from van Zuilen et al. (2016)¹

Table S6: Results of the isotope mass balance between the measured $\delta^{137}\text{Ba}$ of the bulk fraction and the calculated one from the Ba-weighted sum of the solution and bacteria ($\delta^{137}\text{Ba}^{\text{sol}}$, $\delta^{137}\text{Ba}^{\text{bac}}$).

Replicate	Time (h)	Measured $\delta^{137}\text{Ba}_{\text{bulk}}$ (‰)		Calculated $\delta^{137}\text{Ba}_{\text{bulk}}^{\dagger}$ (‰)		Difference ¹ (‰)	
		value	2sd	value	2sd	value	2sd
A	99	na		0.07	0.07		
	138	0.09	0.03	0.13	0.06	0.04	0.07
	187	na		0.06	0.06		
	243	0.10	0.05	0.06	0.07	-0.04	0.08
	315	na		0.07	0.04		
	530	na		0.06	0.08		
	mean	0.10	0.06	0.08	0.05	-0.02	0.08
B	99	0.05	0.06	0.071	0.017	0.03	0.06
	138	na		0.081	0.057		
	171	na		0.095	0.020		
	217	0.118	0.005	0.091	0.046	-0.03	0.05
	267	na		0.064	0.014		
	315	na		0.054	0.069		
	mean	0.08	0.06	0.08	0.03	-0.01	0.07
A-B	mean	0.09	0.06	0.08	0.04	-0.01	0.07

[†]Calculated $\delta^{137}\text{Ba}_{\text{bulk}}$ derived from mass balance calculation with measured $\delta^{137}\text{Ba}_{\text{sol}}$ and $\delta^{137}\text{Ba}_{\text{bac}}$ values

na= not analyzed

¹ Measured $\delta^{137}\text{Ba}_{\text{bulk}} - \text{Calculated } \delta^{137}\text{Ba}_{\text{bulk}}$

Table S7: Optical density at 730 nm ($OD_{730\text{nm}}$) of *G. lithophora* cultures incubated in the BG-11 medium amended with 260 μM Ba and Sr and pH of the inoculated and non-inoculated samples.

Time (h)	OD₇₃₀	1SD	pH inoculated cultures	SD	pH non-inoculated control
0	0.058	0.002	7.463	0.014	7.56
67	0.098	0.006	8.010	0.007	7.58
75	0.108	0.000	8.133	0.028	7.57
90	0.116	0.002	8.302	0.103	7.61
99	0.134	0.001	8.652	0.017	7.68
114	0.152	0.005	8.652	0.117	7.65
123	0.166	0.008	8.588	0.184	7.70
138	0.188	0.007	8.658	0.132	7.68
147	0.208	0.005	8.746	0.157	7.71
162	0.228	0.001	8.527	0.014	7.64
171	0.237	0.005	8.464	0.007	7.70
187	0.259	0.007	8.580	0.080	7.68
195	0.270	0.008	8.614	0.143	7.67
217	0.308	0.014	8.722	0.223	7.73
234	0.328	0.017	8.721	0.256	7.68
243	0.353	0.011	9.273	0.183	7.66
258	0.372	0.016	9.204	0.246	7.69
267	0.399	0.020	9.438	0.202	7.68
282	0.431	0.025	9.389	0.233	7.62
291	0.481	0.038	9.503	0.178	7.61
306	0.507	0.037	9.460	0.261	7.65
315	0.528	0.035	9.583	0.139	7.62
330	0.539	0.033	9.324	0.260	7.65
340	0.563	0.021	9.283	0.094	7.60
361	0.575	0.013	8.933	0.078	7.55
385	0.590	0.016	8.726	0.062	7.69
411	0.645	0.017	9.172	0.098	7.65
428	0.699	0.026	8.956	0.297	7.66
437	0.706	0.026	9.142	0.017	7.73
451	0.725	0.022	9.399	0.125	7.72
459	0.765	0.024	9.465	0.256	7.71
480	0.854	0.033	9.836	0.266	7.63
506	0.944	0.050	9.672	0.435	7.74
530	0.979	0.045	9.328	0.359	7.74
554	1.011	0.040	9.105	0.445	7.74
580	1.057	0.027	9.312	0.034	7.72
603	1.197	0.032	10.332	0.121	7.69

Time (h)	OD₇₃₀	1SD	pH inoculated cultures	SD	pH non-inoculated control
625	1.259	0.050	10.229	0.264	7.79
651	1.379	0.074	10.230	0.246	7.78
674	1.433	0.104	9.734	0.262	7.68
699	1.451	0.074	9.306	0.226	7.69

Table S8: Temporal evolution of Ba, Sr, and Ca concentrations in different fractions during the growth of *G. lithophora*. Data points correspond to the average of the three replicates.

Fraction	Dissolved AEE fraction (>0.22μM) (μM)						AEE cellular incorporation (μM)						Bulk fraction (solution + cyanobacteria) (μM)					
	Ba		Sr		Ca		Ba		Sr		Ca		Ba		Sr		Ca	
Time(h)	values	2SD	values	2SD	values	2SD	values	SD	values	SD	values	SD	values	SD	values	SD	values	SD
0	257.8	12.2	264.4	5.5	232.2	7.3	nd	nd	nd	nd	nd	nd	249.67	26.78	264.87	14.67	249.03	15.83
67	241.6	3.3	268.2	4.8	235.5	2.4	nd	nd	nd	nd	nd	nd	265.42	8.06	266.02	10.76	247.63	10.58
75	230.1	10.6	262.9	7.6	235.0	6.9	nd	nd	nd	nd	nd	nd	268.53	12.43	266.21	8.93	246.53	8.29
90	223.1	13.8	265.3	13.2	231.5	15.8	nd	nd	nd	nd	nd	nd	271.67	7.35	268.89	8.44	250.30	7.51
99	213.4	10.7	263.7	14.6	231.1	16.3	28.04	5.00	1.67	0.29	8.36	2.03	266.35	8.42	263.63	7.85	244.70	5.97
114	201.6	12.6	263.3	10.6	228.6	15.0	39.13	3.23	2.20	0.25	8.51	1.29	271.04	11.33	267.00	11.57	248.94	10.82
123	186.9	8.6	258.2	15.4	222.3	13.8	50.73	3.69	2.79	0.33	9.36	0.57	269.05	11.32	265.27	9.52	246.99	8.07
138	173.5	8.9	259.0	14.5	221.0	12.1	59.33	9.34	3.08	0.60	11.56	1.80	266.65	4.41	262.56	5.63	243.94	7.95
147	159.9	7.6	257.0	15.4	219.6	16.1	57.12	15.35	3.00	0.87	9.55	1.26	265.59	3.79	262.18	5.13	245.42	6.88
162	145.5	6.5	254.0	16.9	218.5	14.2	89.09	3.90	4.71	0.26	12.19	1.12	253.49	6.13	262.20	5.12	239.99	5.59
171	137.9	5.5	253.3	9.9	215.9	10.4	94.01	10.87	5.02	0.85	12.15	2.02	262.12	0.68	262.79	5.91	254.05	22.39
187	122.6	8.4	252.9	6.9	215.0	9.4	112.80	9.33	5.73	0.59	13.78	1.90	264.46	7.46	261.79	2.79	242.41	2.36
195	116.2	10.7	255.6	9.1	217.1	9.3	120.12	16.26	6.08	0.94	15.47	2.00	267.98	10.04	266.55	10.79	247.62	11.09
217	93.1	9.4	254.7	11.4	215.7	8.5	146.30	5.75	7.23	0.24	16.11	1.12	267.64	8.41	264.91	7.99	243.09	10.96
234	74.4	14.1	254.6	11.7	216.8	11.6	164.91	12.71	8.01	0.51	10.83	9.25	262.87	14.57	264.16	5.60	244.49	7.93
243	61.3	14.5	247.1	12.2	207.7	15.9	176.12	17.09	9.05	1.76	19.22	3.91	264.71	1.56	266.79	2.47	247.52	4.01
258	48.3	14.0	247.8	16.1	201.4	21.8	182.90	13.11	10.76	2.53	22.26	7.32	252.50	6.50	261.83	3.89	235.31	8.74
267	35.0	14.8	240.2	14.3	187.6	21.2	182.37	19.11	11.51	3.58	23.69	8.52	259.17	5.98	262.80	1.86	239.59	8.03
282	23.0	14.3	233.4	13.6	180.7	14.5	202.42	17.83	13.73	3.05	29.00	7.61	257.56	6.63	261.40	5.42	235.35	8.07
291	12.0	12.3	229.4	10.1	176.6	17.3	226.10	27.85	23.45	8.34	49.20	18.91	232.17	6.41	250.76	4.07	220.63	9.11
307	5.9	5.7	221.8	9.9	173.1	12.2	228.25	10.06	21.54	9.44	31.26	9.12	263.19	19.73	263.24	15.06	243.26	23.87
315	2.5	0.8	211.2	15.3	171.0	12.5	258.06	44.76	29.75	13.77	33.17	12.08	260.51	12.66	260.03	11.41	246.73	27.53
330	2.9	0.8	201.1	13.4	176.8	5.7	237.26	2.95	43.25	12.09	40.34	8.09	264.52	8.68	259.88	8.68	239.06	12.76

Fraction	Dissolved AEE fraction (>0.22µM) (µM)						AEE cellular incorporation (µM)						Bulk fraction (solution + cyanobacteria) (µM)					
	Ba		Sr		Ca		Ba		Sr		Ca		Ba		Sr		Ca	
Time(h)	values	2SD	values	2SD	values	2SD	values	SD	values	SD	values	SD	values	SD	values	SD	values	SD
340	3.1	1.7	189.3	7.9	173.3	12.1	222.78	3.30	48.00	8.29	32.58	4.49	247.54	8.39	257.17	8.93	233.19	19.76
361	3.5	1.0	188.9	13.6	197.8	5.1	230.83	10.23	61.35	5.00	28.11	5.72	253.36	5.56	260.90	3.28	236.64	1.50
385	3.6	1.5	171.2	10.5	210.0	9.1	223.70	15.64	76.07	5.63	25.27	2.40	268.04	13.73	265.10	9.90	244.90	10.35
411	3.7	0.7	135.4	24.8	208.4	13.2	243.88	9.12	115.66	10.85	28.34	3.82	249.56	11.66	250.86	7.84	231.23	6.16
428	2.4	1.2	109.8	27.8	200.6	23.7	246.55	4.73	134.88	12.43	28.86	2.75	262.90	8.37	258.27	8.51	237.49	10.24
437	3.8	0.3	99.0	25.2	198.9	15.2	251.28	6.01	150.83	14.69	31.45	4.00	252.38	11.02	249.79	9.20	230.09	9.44
451	2.8	0.9	80.8	21.7	200.1	8.6	237.69	13.19	159.88	16.11	29.94	3.15	252.15	10.19	249.95	7.78	231.91	8.33
459	2.8	1.0	69.5	25.6	199.9	12.4	255.15	2.24	183.05	20.65	31.95	1.41	269.18	9.44	262.22	5.92	242.83	3.95
480	2.5	0.2	46.8	22.3	213.8	14.5	257.70	11.64	207.75	23.68	38.21	9.32	262.64	10.20	258.84	8.48	244.48	4.82
506	3.9	0.7	22.7	17.7	205.6	1.7	254.35	2.60	230.09	17.87	38.24	2.63	265.00	1.97	259.88	1.58	244.71	1.09
530	3.3	1.3	6.6	5.6	201.5	3.4	259.75	2.44	250.65	9.21	42.29	3.50	272.34	4.84	263.63	4.12	246.61	4.12
554	2.7	0.2	2.5	0.5	190.4	7.4	271.73	1.93	262.55	4.26	51.71	5.34	283.40	3.73	269.90	1.79	250.02	2.05
580	2.6	0.3	2.3	0.1	170.4	23.0	265.05	9.15	251.68	8.73	67.74	11.11	260.45	4.24	248.12	1.13	259.56	33.63
603	2.5	0.6	2.6	0.6	149.8	17.1	264.61	3.69	251.67	0.99	82.58	12.68	273.37	13.58	260.82	10.78	246.78	10.86
625	1.5	0.9	1.7	0.5	141.6	24.4	263.32	8.81	247.47	8.24	90.97	9.62	269.17	2.10	254.83	1.61	241.67	1.57
651	1.3	0.9	1.6	0.5	115.8	20.7	275.02	6.92	260.09	7.96	121.64	8.36	271.62	7.58	256.52	4.04	241.52	3.01
674	1.7	0.7	2.2	0.7	95.4	29.5	274.04	7.05	257.99	8.55	132.66	17.68	272.95	3.44	258.50	4.54	241.18	4.90
699	1.3	0.5	1.8	0.6	54.2	36.2	263.81	6.07	253.90	2.93	168.91	29.59	276.81	3.55	261.48	2.30	245.66	2.09

Table S9: Summary of Ba elemental and isotope data for time points where isotope measurements were performed

Replicate	Fraction	Time (h)	Ba concentration (μM)		Remaining f(Ba) _{sol}	Elemental yield*	$\delta^{137}\text{Ba} (\text{\textperthousand})$		Corrected $\delta^{137}\text{Ba} (\text{\textperthousand})^{\ddagger}$
			value	2sd			value	2sd	
R1-R2	Growth solution [†]	0	258	4	1	nd	0.09	0.02	0
R1	Growth solution	0	268.7	0.8	1.00	1.22	0.10	0.02	0.01
		99	222	3	0.83	0.93	0.10	0.04	0.01
		138	180	3	0.67	0.90	0.21	0.04	0.11
		187	123.3	0.7	0.46	0.95	0.19	0.04	0.09
		243	55.1	0.2	0.21	0.91	0.31	0.05	0.22
		330	3.43	0.06	0.01	0.91	0.05	0.04	-0.05
		530	3.742	0.003	0.01	0.98	0.07	0.07	-0.03
	Cells	99	33.79	0.08	0.83	0.93	-0.15	0.05	-0.24
		138	60.1	0.3	0.67	0.90	-0.10	0.05	-0.20
		187	120	2	0.46	0.95	-0.06	0.05	-0.16
		243	185.5	0.8	0.21	0.91	-0.01	0.04	-0.11
		315	228	2	0.01	0.85	0.07	0.01	-0.03
		530	262.5	0.9	0.01	0.98	0.06	0.04	-0.03
	Bulk	138	266	2	0.67	0.90	0.09	0.03	0.00
		243	263	2	0.21	0.91	0.10	0.05	0.01
R2	Growth solution	0	248	2	1.00	0.97	0.09	0.02	-0.01
		67	241.5	0.6	0.98	0.93	0.12	0.08	0.02
		99	214	2	0.86	0.93	0.10	0.02	0.00
		138	175	4	0.71	0.86	0.14	0.06	0.05
		171	140.7	0.4	0.57	0.88	0.21	0.02	0.12
		195	126.0	0.5	0.51	0.87	0.24	0.05	0.14
		217	102.1	0.7	0.41	0.93	0.28	0.05	0.18
		243	76	1	0.31	0.87	0.29	0.05	0.20
		267	50	1	0.20	0.88	0.382	0.007	0.288
		291	24.2	0.2	0.10	0.97	0.47	0.07	0.38
		315	3.22	0.01	0.01	0.91	0.13	0.04	0.04
		340	4.83	0.01	0.02	0.95	0.03	0.05	-0.06
		459	3.80	0.01	0.02	0.98	-0.01	0.07	-0.10
		530	4.19	0.02	0.02	0.94	0.05	0.07	-0.05
	Cells	99	25.70	0.04	0.86	0.93	-0.128	0.006	-0.222
		138	49.6	0.5	0.71	0.86	-0.141	0.005	-0.235
		171	91	2	0.57	0.88	-0.086	0.002	-0.180
		217	140	3	0.41	0.93	-0.044	0.002	-0.138
		267	174	4	0.20	0.88	-0.03	0.01	-0.121

Replicate	Fraction	Time (h)	Ba concentration (μM)		Remaining $f(\text{Ba})_{\text{sol}}$	Elemental yield*	$\delta^{137}\text{Ba} (\text{\textperthousand})$		Corrected $\delta^{137}\text{Ba} (\text{\textperthousand})^{\ddagger}$
			value	2sd			value	2sd	
		315	237	2	0.01	0.91	0.05	0.05	-0.04
		437	244.8	0.1	0.02	1.03	0.07	0.03	-0.02
Bulk		99	258	3	0.86	0.97	0.05	0.06	-0.05
		217	259	4	0.41	0.93	0.12	0.01	0.02

*defined as the ratio between the sum of the element concentration in solution plus bacteria fractions, and the element concentration in the bulk fraction

‡ Corrected $\delta^{137}\text{Ba} (\text{\textperthousand})$ = Corrected Ba ($\delta^{137}\text{Ba}$) for the initial solution isotope signature. 2sd = 0.05‰

† Mean of the initial solution values

Table S10: Summary of Sr elemental and isotope data for time points where isotope measurements were performed.

	Fraction	Time (h)	Sr concentration (μM)	Remaining f(Sr) _{sol}	Elemental yield*	δ ⁸⁸ Sr (‰)		Corrected δ ⁸⁸ Sr (‰)‡	
						value	2sd		
R1-R2	Growth solution [†]	0	265	4	1	nd	0.87	0.07	0
R1	Cells	291	27.88	0.07	0.88	1.06	0.792	0.006	-0.076
		340	57.2	0.1	0.70	0.95	0.60	0.02	-0.27
		411	128	1	0.41	0.96	0.621	0.002	-0.247
		451	178	2	0.22	0.97	0.68	0.06	-0.19
	Growth solution	0	270	1	1.00	1.03	0.85	0.09	-0.02
		267	250	2	0.93	0.98	0.897	0.006	0.029
		291	237	3	0.88	1.06	0.88	0.05	0.01
		306	222	2	0.82	0.93	0.93	0.03	0.06
		306	208	1	0.77	0.89	0.95	0.03	0.08
		340	188	3	0.70	0.95	1.01	0.04	0.14
		385	164	2	0.61	0.88	1.07	0.01	0.20
		411	110.8	0.7	0.41	0.96	1.18	0.02	0.31
		428	89.1	0.9	0.33	0.92	1.25	0.02	0.38
		451	59.8	0.2	0.22	0.97	1.43	0.02	0.56
R2	Cells	459	45.8	0.2	0.17	0.93	1.469	0.006	0.601
		480	25.04	0.05	0.09	1.04	1.66	0.03	0.79
		506	6.97	0.03	0.03	0.98	1.41	0.05	0.54
		340	257.2	0.8	0.70	0.95	0.82	0.03	-0.05
		451	245	3	0.22	0.97	0.83	0.07	-0.04
		123	2.47	0.01	0.96	0.99	0.71	0.07	-0.15
		162	4.42	0.04	0.93	0.96	0.72	0.03	-0.15
		195	5.01	0.02	1.00	1.04	0.77	0.09	-0.10
		258	8.70	0.05	0.96	0.99	0.72	0.05	-0.15
		291	13.83	0.06	0.89	0.99	0.70	0.04	-0.17
R2	Growth solution	361	58.2	0.5	0.72	0.94	0.542	0.007	-0.326
		385	79.4	0.4	0.64	0.96	0.54	0.02	-0.32
		411	107	1	0.56	1.03	0.62	0.02	-0.25
		428	131	1	0.40	0.94	0.62	0.02	-0.25
		480	194	2	0.20	0.93	0.71	0.02	-0.15
		0	261	5	1.00	1.03	0.89	0.03	0.02
		123	251	3	0.96	0.99	0.9	0.1	0.0
		162	241.5	0.7	0.93	0.96	0.84	0.04	-0.03
		195	260	2	1.00	1.04	0.9	0.2	0.0
		258	250	2	0.96	0.99	0.86	0.06	-0.01
		291	231	2	0.89	0.99	0.88	0.06	0.02

Fraction	Time (h)	Sr concentration (μ M)		Remaining $f(\text{Sr})_{\text{sol}}$	Elemental yield*	$\delta^{88}\text{Sr} (\text{\textperthousand})$		Corrected $\delta^{88}\text{Sr} (\text{\textperthousand})^{\ddagger}$
		value	2sd			value	2sd	
	330	214.5	0.4	0.82	0.98	0.95	0.08	0.08
	361	187	4	0.72	0.94	0.97	0.06	0.10
	385	168	2	0.64	0.96	1.01	0.03	0.15
	411	145.0	0.7	0.56	1.03	1.10	0.02	0.23
	428	104.1	0.3	0.40	0.94	1.17	0.07	0.30
	451	86	1	0.33	0.95	1.3	0.1	0.4
	480	53.0	0.4	0.20	0.93	1.45	0.05	0.58
	506	23.6	0.1	0.09	0.98	1.61	0.01	0.75
	554	2.07	0.01	0.01	0.98	0.89	0.05	0.02
	603	2.029	0.006	0.01	1.02	0.79	0.04	-0.08
Bulk	291	247	1	0.89	0.99	0.82	0.01	-0.05
	480	266	3	0.20	0.93	0.88	0.07	0.01

*defined as the ratio between the sum of the element concentration in solution plus bacteria fractions, and the element concentration in the bulk fraction

\ddagger Corrected $\delta^{88}\text{Sr} (\text{\textperthousand}) = \text{Corrected Sr } (\delta^{88}\text{Sr})$ for the initial solution isotope signature. $2\text{sd} = 0.05\text{\textperthousand}$

\dagger Mean of the initial solution values

Table S11: Numeric format of EDXS spectra shown in Figure 3C, Figure 3F, and Figure 3I.

Energy (eV)	Figure 3C			Figure 3F		Figure 3I		
	Ca-core	PolyP	Ba-rich	PolyP	Ba-Sr-rich	Sr-rich	PolyP	Ba-rich
ev	counts	counts	counts	counts	counts	counts	counts	counts
0	0	0	0	0	0	0	0	0
10	0	0	0	0	0	0	0	0
20	0	0	0	0	0	0	0	0
30	0	0	0	0	0	0	0	0
40	0	0	0	0	0	0	0	0
50	0	0	0	0	0	0	0	0
60	0	0	0	0	0	0	0	0
70	0	0	0	0	0	0	0	0
80	0	0	0	0	0	0	0	0
90	14	165	77	203	15203	21	38	6
100	12	97	48	122	8325	13	24	0
110	6	56	24	54	3799	2	10	2
120	5	30	17	20	1786	0	7	1
130	4	33	15	25	1079	1	4	0
140	7	28	27	24	1080	1	4	1
150	6	40	21	40	1501	1	6	0
160	7	36	37	46	1935	4	5	0
170	6	67	49	47	2603	11	12	1
180	10	72	54	57	3421	10	17	1
190	20	99	90	105	4791	8	20	1
200	19	102	103	150	6824	15	22	0
210	27	168	199	184	10805	28	29	5
220	34	229	226	319	17427	41	70	4
230	69	339	339	430	28447	57	90	13
240	104	470	485	715	44536	63	140	11
250	108	665	603	970	63866	104	200	16
260	179	821	818	1219	83417	130	261	14
270	185	883	1003	1429	97189	165	276	24
280	187	938	945	1473	100070	152	310	23
290	152	879	924	1331	90880	135	321	17
300	137	790	719	1108	73741	117	240	14
310	101	557	583	862	53443	98	182	9
320	80	390	387	515	34740	61	130	11
330	62	292	278	349	21524	40	89	8
340	40	227	184	272	14162	32	57	5
350	24	195	142	218	11370	24	45	4

Energy (eV)	Figure 3C			Figure 3F			Figure 3I		
	Ca-core	PolyP	Ba-rich	PolyP	Ba-Sr-rich	Sr-rich	PolyP	Ba-rich	
ev	counts	counts	counts	counts	counts	counts	counts	counts	
360	27	177	133	218	11232	16	46	3	
370	23	186	134	232	12191	27	57	2	
380	24	182	137	255	13444	20	62	4	
390	17	192	140	293	13947	23	70	2	
400	23	200	131	297	13832	28	76	5	
410	39	233	163	289	12595	24	62	8	
420	30	230	160	247	11002	23	62	5	
430	39	259	159	286	10217	35	70	10	
440	55	323	191	341	10364	40	74	10	
450	63	448	227	442	12404	50	84	25	
460	120	666	330	621	16396	62	142	33	
470	151	920	522	862	23297	110	188	33	
480	215	1281	652	1246	32771	160	266	47	
490	306	1699	890	1790	44725	199	328	77	
500	391	2256	1126	2245	56580	240	433	100	
510	457	2598	1277	2650	66753	289	475	90	
520	483	2808	1430	2951	71968	320	598	118	
530	477	2787	1370	2898	72193	367	583	100	
540	407	2510	1294	2645	65616	316	520	95	
550	364	2062	1153	2123	54410	232	409	91	
560	276	1637	838	1570	41493	179	310	69	
570	185	1191	661	1071	30280	141	219	48	
580	131	907	495	752	21137	85	165	32	
590	92	652	408	473	15403	58	84	25	
600	66	462	337	340	11870	54	73	15	
610	51	381	281	244	9600	32	71	22	
620	35	324	238	205	8061	20	60	5	
630	60	244	194	177	7118	13	46	3	
640	34	222	156	147	6326	21	40	9	
650	22	169	150	133	5896	16	35	12	
660	30	160	128	141	5788	12	34	7	
670	25	147	114	130	5600	21	25	4	
680	16	126	116	119	5372	26	31	5	
690	23	116	95	118	5293	22	26	10	
700	20	103	89	128	5144	17	13	7	
710	21	115	104	119	4891	19	29	5	
720	20	119	94	104	4963	22	26	4	
730	16	152	98	95	4891	14	22	4	

Energy (eV)	Figure 3C			Figure 3F			Figure 3I		
	Ca-core	PolyP	Ba-rich	PolyP	Ba-Sr-rich	Sr-rich	PolyP	Ba-rich	
ev	counts	counts	counts	counts	counts	counts	counts	counts	
740	20	141	137	118	5175	22	24	8	
750	22	203	148	130	5669	23	31	8	
760	30	165	141	112	6298	18	51	6	
770	34	196	156	174	6916	14	47	10	
780	44	237	170	154	7430	19	63	19	
790	41	269	176	155	7655	28	43	9	
800	37	244	181	175	7811	29	51	11	
810	36	229	145	149	7289	22	48	7	
820	30	207	155	154	6625	22	38	6	
830	35	195	142	141	5937	25	51	9	
840	24	181	110	130	5433	6	29	9	
850	24	141	117	101	4946	18	31	4	
860	21	128	91	85	4448	12	22	11	
870	19	127	83	105	4200	15	31	7	
880	20	131	93	90	4402	10	34	5	
890	30	153	112	103	4837	15	34	9	
900	26	170	101	115	5420	18	38	7	
910	35	157	147	106	6166	22	45	4	
920	17	190	148	134	6857	18	50	7	
930	31	173	158	132	7380	28	38	9	
940	35	202	141	153	7600	23	52	9	
950	38	201	158	129	7363	28	45	6	
960	36	223	147	132	7059	28	53	8	
970	27	169	134	108	6649	25	39	12	
980	36	188	125	97	5851	16	39	8	
990	27	151	103	98	5281	21	29	4	
1000	12	145	101	107	4808	10	27	6	
1010	20	115	84	106	4363	14	22	4	
1020	18	126	96	105	4253	14	26	6	
1030	21	123	86	116	4140	14	37	5	
1040	15	107	59	86	4170	10	29	9	
1050	16	112	68	124	4113	13	23	7	
1060	19	105	71	95	3901	7	20	4	
1070	9	89	75	94	3755	14	12	7	
1080	15	101	59	84	3544	7	28	3	
1090	19	93	67	75	3341	17	27	3	
1100	11	99	67	77	3108	13	22	2	
1110	25	97	52	62	2958	9	18	7	

Energy (eV)	Figure 3C			Figure 3F			Figure 3I		
	Ca-core	PolyP	Ba-rich	PolyP	Ba-Sr-rich	Sr-rich	PolyP	Ba-rich	
ev	counts	counts	counts	counts	counts	counts	counts	counts	
1120	12	85	51	73	2928	7	22	2	
1130	12	73	53	77	2917	8	22	3	
1140	8	76	45	70	2914	8	17	4	
1150	7	86	51	61	2868	10	13	5	
1160	5	70	40	76	2904	13	16	3	
1170	15	76	46	80	3032	7	14	4	
1180	12	82	51	97	3194	11	27	8	
1190	11	77	46	116	3628	15	24	1	
1200	15	75	60	133	4136	10	21	5	
1210	22	81	70	171	4963	16	20	4	
1220	26	111	73	244	6014	10	26	4	
1230	33	130	92	295	7149	18	31	11	
1240	42	139	79	329	8091	9	35	5	
1250	49	155	86	376	8794	25	36	7	
1260	53	168	108	366	9258	26	33	7	
1270	44	148	84	384	9149	27	45	2	
1280	30	150	81	327	8475	21	30	6	
1290	33	143	84	334	7465	17	33	4	
1300	24	137	88	228	6322	23	29	2	
1310	32	98	73	192	5221	17	20	2	
1320	11	74	68	140	4317	11	19	6	
1330	25	102	61	118	3637	14	15	4	
1340	17	80	50	93	3231	9	11	4	
1350	13	73	49	66	2898	13	18	3	
1360	8	84	44	83	2723	7	13	4	
1370	10	74	49	58	2584	9	13	3	
1380	9	61	37	63	2526	12	11	2	
1390	7	66	32	64	2442	8	15	5	
1400	12	60	47	62	2446	4	14	3	
1410	9	78	50	52	2461	4	21	6	
1420	10	52	46	61	2490	12	12	10	
1430	8	64	54	64	2586	7	12	10	
1440	5	61	53	52	2578	13	16	7	
1450	11	59	41	77	2627	8	15	6	
1460	11	64	62	49	2698	6	10	2	
1470	19	66	47	63	2626	9	12	4	
1480	9	66	44	60	2653	10	17	1	
1490	10	66	52	57	2780	5	15	3	

Energy (eV)	Figure 3C			Figure 3F			Figure 3I		
	Ca-core	PolyP	Ba-rich	PolyP	Ba-Sr-rich	Sr-rich	PolyP	Ba-rich	
ev	counts	counts	counts	counts	counts	counts	counts	counts	
1500	12	85	73	59	2723	9	16	4	
1510	11	73	45	59	2769	15	13	5	
1520	10	66	46	67	2775	14	20	3	
1530	16	64	47	61	2842	10	14	3	
1540	10	73	45	68	2991	9	21	6	
1550	9	64	38	76	3048	22	20	4	
1560	14	59	50	80	3150	12	18	6	
1570	16	68	43	98	3267	19	25	0	
1580	8	75	46	70	3318	20	12	8	
1590	14	66	50	67	3385	29	23	4	
1600	19	62	48	84	3412	25	25	4	
1610	14	70	41	76	3446	15	34	11	
1620	4	53	56	90	3374	14	28	5	
1630	17	75	44	82	3288	21	14	6	
1640	8	62	32	82	3271	15	21	7	
1650	9	54	39	83	3234	15	16	5	
1660	10	87	58	79	3317	24	17	4	
1670	11	52	53	89	3259	14	20	8	
1680	4	71	48	79	3465	11	19	5	
1690	10	64	47	88	3675	11	18	3	
1700	11	68	42	90	3899	17	26	5	
1710	9	68	38	115	4542	18	28	3	
1720	9	71	59	101	5269	32	27	5	
1730	18	73	42	126	6084	34	21	12	
1740	15	90	64	164	7607	47	36	18	
1750	15	80	57	224	9434	73	47	16	
1760	18	102	60	264	11868	119	71	28	
1770	18	107	68	348	14555	121	71	37	
1780	25	115	85	400	17305	188	79	29	
1790	12	123	87	471	20123	208	101	48	
1800	12	143	75	567	22554	244	96	54	
1810	17	143	76	564	23916	246	109	63	
1820	32	137	80	555	24382	282	106	54	
1830	17	176	81	619	24191	268	131	70	
1840	15	149	81	548	22919	258	119	63	
1850	13	173	67	528	21489	223	88	56	
1860	10	169	87	479	19294	194	98	42	
1870	16	173	59	461	17392	163	79	52	

Energy (eV)	Figure 3C			Figure 3F			Figure 3I		
	Ca-core	PolyP	Ba-rich	PolyP	Ba-Sr-rich	Sr-rich	PolyP	Ba-rich	
ev	counts	counts	counts	counts	counts	counts	counts	counts	
1880	15	175	66	414	15646	151	98	35	
1890	12	173	56	382	13818	123	80	40	
1900	10	223	51	362	12139	97	77	28	
1910	13	192	48	346	11056	94	89	29	
1920	15	251	42	346	10052	82	88	17	
1930	7	323	42	402	9625	61	71	28	
1940	10	430	45	486	9814	52	93	9	
1950	13	546	50	485	10397	36	128	14	
1960	11	689	47	647	11804	42	159	6	
1970	11	817	46	864	13834	34	190	8	
1980	13	1022	50	1075	16659	28	241	9	
1990	15	1349	61	1233	18882	23	281	10	
2000	5	1530	56	1471	21476	18	394	4	
2010	9	1683	60	1535	22963	21	379	6	
2020	11	1587	53	1526	23298	17	386	4	
2030	5	1622	56	1567	22818	18	347	3	
2040	6	1427	46	1379	20673	15	317	5	
2050	10	1234	40	1230	18270	15	314	8	
2060	13	1058	58	978	15193	16	206	3	
2070	7	854	45	752	12034	7	179	4	
2080	9	661	54	560	9339	6	147	2	
2090	18	424	34	406	7200	4	115	3	
2100	11	369	36	275	5655	14	73	5	
2110	12	274	32	237	4457	6	62	3	
2120	13	236	40	213	4019	7	51	4	
2130	7	163	26	166	3498	8	45	4	
2140	4	155	41	112	3338	15	29	2	
2150	13	114	42	134	3164	7	31	0	
2160	13	113	44	114	2998	9	29	0	
2170	7	112	52	103	2882	8	19	2	
2180	5	104	31	101	2755	10	25	6	
2190	12	109	36	94	2703	5	19	3	
2200	11	71	41	86	2601	10	23	4	
2210	6	84	33	66	2489	10	17	3	
2220	11	60	28	65	2472	11	12	4	
2230	11	69	42	78	2527	6	20	2	
2240	6	65	30	72	2670	11	16	3	
2250	9	68	42	62	2790	4	16	3	

Energy (eV)	Figure 3C			Figure 3F			Figure 3I		
	Ca-core	PolyP	Ba-rich	PolyP	Ba-Sr-rich	Sr-rich	PolyP	Ba-rich	
	ev	counts	counts	counts	counts	counts	counts	counts	counts
2260	12	57	49	58	3035	9	17	0	
2270	10	66	41	61	3342	15	18	2	
2280	10	63	60	72	3844	5	19	4	
2290	11	53	52	74	4007	10	13	3	
2300	14	72	59	75	4387	9	20	1	
2310	10	73	66	83	4330	8	19	4	
2320	8	74	51	65	4366	7	16	4	
2330	10	59	43	58	4245	11	19	1	
2340	11	65	48	77	3967	14	12	2	
2350	7	64	61	60	3539	6	18	5	
2360	13	54	42	60	3170	9	9	6	
2370	8	43	45	51	2824	9	9	1	
2380	4	52	41	43	2561	3	15	1	
2390	8	65	36	41	2236	6	11	4	
2400	11	55	29	42	2088	9	13	4	
2410	7	54	36	45	1911	8	17	3	
2420	8	43	37	40	1909	4	10	2	
2430	11	59	28	39	1891	4	12	2	
2440	13	46	32	46	1886	10	14	3	
2450	6	64	33	46	1842	4	16	2	
2460	10	59	42	36	1846	8	8	3	
2470	12	65	36	42	1976	5	14	3	
2480	5	60	41	42	1947	5	12	1	
2490	6	59	50	45	1900	5	9	2	
2500	9	46	31	45	1924	6	11	3	
2510	6	46	39	32	1884	8	7	0	
2520	10	48	48	38	1840	3	7	3	
2530	7	49	37	35	1930	4	13	2	
2540	8	45	38	49	1913	6	12	1	
2550	9	54	45	41	1984	5	15	5	
2560	7	44	46	24	2106	5	17	2	
2570	9	68	53	42	2145	6	13	4	
2580	10	60	43	46	2326	12	16	3	
2590	12	45	59	38	2498	14	15	3	
2600	15	55	45	43	2794	7	18	0	
2610	13	65	41	48	3005	3	12	0	
2620	12	41	55	64	3046	9	11	1	
2630	9	64	54	53	3106	14	16	2	

Energy (eV)	Figure 3C			Figure 3F			Figure 3I		
	Ca-core	PolyP	Ba-rich	PolyP	Ba-Sr-rich	Sr-rich	PolyP	Ba-rich	
	ev	counts	counts	counts	counts	counts	counts	counts	counts
2640	10	50	64	55	3026	5	15	2	
2650	11	59	69	54	3067	9	11	5	
2660	15	62	45	55	2749	9	10	2	
2670	8	56	56	44	2666	8	8	3	
2680	16	57	60	34	2532	8	15	3	
2690	6	54	43	39	2267	4	12	5	
2700	10	44	43	39	2167	6	13	5	
2710	7	52	49	32	2095	7	11	4	
2720	9	47	36	39	2020	9	11	4	
2730	12	55	36	43	1954	4	8	3	
2740	8	42	56	26	1904	10	8	6	
2750	14	34	37	37	1758	4	7	3	
2760	14	56	40	27	1723	8	10	4	
2770	15	35	39	42	1669	6	9	0	
2780	15	39	39	43	1721	5	9	5	
2790	10	44	42	48	1679	1	9	2	
2800	9	25	37	38	1699	4	10	3	
2810	14	34	36	44	1684	4	8	3	
2820	9	41	40	36	1638	3	9	5	
2830	8	40	39	29	1677	5	12	2	
2840	6	40	41	36	1601	6	6	1	
2850	6	39	26	34	1571	4	10	0	
2860	8	43	35	44	1538	7	6	2	
2870	4	31	41	32	1459	3	11	1	
2880	8	48	24	30	1494	7	12	3	
2890	4	47	30	32	1547	4	13	6	
2900	7	40	25	32	1498	6	8	1	
2910	6	51	26	34	1472	5	8	1	
2920	4	45	35	26	1449	6	11	2	
2930	7	44	34	36	1439	3	11	4	
2940	7	45	31	33	1461	9	7	2	
2950	5	31	35	30	1442	4	5	2	
2960	7	33	30	39	1475	8	14	1	
2970	6	34	23	26	1419	6	11	4	
2980	4	26	16	30	1430	4	4	2	
2990	9	35	29	29	1426	3	7	0	
3000	7	39	25	24	1380	4	11	4	
3010	3	23	27	45	1443	2	5	4	

Energy (eV)	Figure 3C			Figure 3F		Figure 3I		
	Ca-core	PolyP	Ba-rich	PolyP	Ba-Sr-rich	Sr-rich	PolyP	Ba-rich
ev	counts	counts	counts	counts	counts	counts	counts	counts
3020	7	32	17	32	1462	5	10	4
3030	8	22	32	36	1453	6	9	3
3040	7	41	32	34	1424	5	10	5
3050	7	39	36	32	1498	4	4	1
3060	7	36	34	38	1462	5	9	1
3070	13	47	31	23	1475	4	10	0
3080	8	38	42	37	1468	0	15	2
3090	8	41	28	22	1434	6	6	2
3100	10	43	25	34	1543	1	6	1
3110	14	36	29	30	1488	8	10	4
3120	7	40	36	38	1483	7	5	3
3130	14	35	27	28	1550	6	8	3
3140	9	47	33	35	1450	5	8	1
3150	5	32	33	32	1422	3	8	6
3160	7	27	24	36	1439	3	9	1
3170	12	35	29	40	1501	5	9	2
3180	9	32	23	29	1480	3	9	2
3190	10	31	29	35	1522	3	14	1
3200	8	36	22	57	1471	3	8	3
3210	7	28	20	37	1642	7	8	3
3220	5	33	24	36	1646	4	12	5
3230	9	48	21	49	1840	5	6	2
3240	14	54	20	68	2089	5	8	1
3250	7	51	19	91	2280	4	6	2
3260	14	63	20	116	2575	3	14	3
3270	6	74	25	108	2840	6	4	1
3280	4	65	37	138	3327	3	11	2
3290	7	66	26	141	3613	9	9	3
3300	12	65	25	185	4011	5	10	1
3310	5	52	30	193	4474	7	9	4
3320	6	73	29	191	4401	2	13	1
3330	7	72	26	185	4398	3	16	0
3340	12	52	30	195	4260	8	11	2
3350	9	59	27	167	3842	3	3	4
3360	8	77	27	158	3545	2	11	0
3370	9	52	34	129	3114	5	8	2
3380	7	43	33	108	2747	4	8	1
3390	5	48	26	88	2415	4	3	2

Energy (eV)	Figure 3C			Figure 3F			Figure 3I		
	Ca-core	PolyP	Ba-rich	PolyP	Ba-Sr-rich	Sr-rich	PolyP	Ba-rich	
ev	counts	counts	counts	counts	counts	counts	counts	counts	
3400	11	45	20	64	2084	2	10	2	
3410	8	46	23	65	1979	0	12	2	
3420	6	43	37	34	1635	3	9	2	
3430	12	26	36	37	1498	4	8	2	
3440	9	31	34	31	1429	4	7	0	
3450	3	31	32	37	1372	4	7	2	
3460	8	33	30	27	1446	8	9	2	
3470	5	27	27	25	1267	5	6	0	
3480	8	33	36	29	1337	3	4	1	
3490	5	38	33	39	1333	5	10	1	
3500	8	33	33	40	1384	3	6	1	
3510	10	36	30	29	1309	3	9	1	
3520	9	21	23	36	1444	6	3	1	
3530	12	33	18	29	1424	1	8	1	
3540	8	38	25	39	1487	7	6	2	
3550	9	37	27	47	1503	3	6	4	
3560	17	32	19	46	1645	4	13	3	
3570	18	34	26	65	1667	6	6	1	
3580	18	34	19	41	1699	9	9	0	
3590	29	40	30	53	1762	1	11	4	
3600	26	51	33	45	1954	4	10	2	
3610	33	35	40	63	2158	7	12	2	
3620	50	50	34	75	2343	12	14	4	
3630	71	51	39	72	2566	9	22	6	
3640	87	54	49	69	2859	12	22	3	
3650	101	60	38	57	3202	14	17	5	
3660	132	57	69	69	3535	16	21	6	
3670	144	75	58	58	3923	16	17	6	
3680	182	72	70	79	4147	16	26	4	
3690	186	81	68	92	4306	10	27	6	
3700	199	71	74	86	4272	19	36	8	
3710	165	72	67	91	4122	18	29	10	
3720	157	66	58	92	3922	17	26	12	
3730	146	53	61	66	3687	18	22	7	
3740	133	62	48	69	3313	10	23	4	
3750	111	53	57	55	3002	20	16	7	
3760	101	52	60	58	2670	9	13	4	
3770	63	57	40	45	2283	8	11	1	

Energy (eV)	Figure 3C			Figure 3F			Figure 3I		
	Ca-core	PolyP	Ba-rich	PolyP	Ba-Sr-rich	Sr-rich	PolyP	Ba-rich	
	ev	counts	counts	counts	counts	counts	counts	counts	counts
3780	46	43	34	43	1927	6	9	5	
3790	41	43	39	50	1743	10	13	2	
3800	21	30	33	45	1512	7	13	2	
3810	18	34	28	36	1441	10	4	1	
3820	21	35	22	31	1348	6	11	3	
3830	17	35	14	37	1353	6	6	1	
3840	12	36	25	27	1299	7	7	1	
3850	12	34	28	27	1339	11	11	0	
3860	7	28	37	23	1268	7	9	4	
3870	16	29	24	28	1439	6	4	1	
3880	13	47	24	27	1554	8	12	4	
3890	7	47	42	34	1597	5	11	4	
3900	6	58	46	39	1679	9	13	5	
3910	18	48	37	28	1796	3	19	6	
3920	13	43	39	43	1980	4	14	4	
3930	12	66	41	43	2146	12	22	3	
3940	24	62	69	47	2331	11	19	4	
3950	31	59	52	55	2369	10	15	5	
3960	28	64	67	51	2474	14	9	4	
3970	32	76	54	52	2524	4	25	10	
3980	23	70	65	41	2372	7	16	4	
3990	27	78	62	40	2475	4	15	8	
4000	29	78	50	42	2373	4	13	7	
4010	33	60	48	46	2310	5	15	5	
4020	39	56	52	43	2221	7	15	2	
4030	37	51	47	32	2157	7	18	2	
4040	29	56	44	35	1903	3	11	1	
4050	30	39	35	40	1826	7	6	1	
4060	26	46	42	44	1674	6	10	3	
4070	26	47	42	26	1622	2	12	0	
4080	18	37	32	41	1512	4	7	1	
4090	17	41	35	27	1396	4	15	4	
4100	9	37	33	24	1434	2	8	2	
4110	15	38	21	26	1304	2	8	3	
4120	12	46	28	28	1317	7	6	4	
4130	12	34	27	23	1373	2	11	0	
4140	8	36	33	28	1333	6	10	1	
4150	6	34	28	30	1272	5	3	2	

Energy (eV)	Figure 3C			Figure 3F			Figure 3I		
	Ca-core	PolyP	Ba-rich	PolyP	Ba-Sr-rich	Sr-rich	PolyP	Ba-rich	
ev	counts	counts	counts	counts	counts	counts	counts	counts	
4160	13	39	28	34	1270	6	11	0	
4170	11	37	25	26	1337	6	7	1	
4180	13	40	30	34	1314	1	10	3	
4190	4	36	26	25	1317	2	10	1	
4200	9	50	32	23	1309	7	6	2	
4210	8	39	33	32	1390	8	3	3	
4220	7	37	42	33	1383	3	7	3	
4230	9	38	32	24	1357	4	10	1	
4240	8	39	38	19	1438	9	6	2	
4250	5	31	29	25	1386	4	9	2	
4260	13	46	30	22	1451	4	8	6	
4270	6	48	34	21	1555	10	4	2	
4280	8	48	28	31	1614	5	11	1	
4290	15	46	38	32	1754	5	14	1	
4300	3	44	50	37	1804	1	6	11	
4310	10	58	49	42	1933	5	9	1	
4320	14	59	38	50	2214	4	13	2	
4330	11	85	61	47	2472	4	19	2	
4340	16	108	86	57	2849	5	24	7	
4350	11	104	90	54	3531	6	21	5	
4360	24	155	120	96	4372	8	26	9	
4370	37	168	187	98	5798	18	48	13	
4380	40	250	234	118	7321	20	47	13	
4390	71	327	273	168	9530	18	62	15	
4400	71	400	327	232	12283	26	88	22	
4410	99	475	438	258	15138	41	102	26	
4420	113	593	562	352	18754	41	120	32	
4430	114	719	648	390	21645	49	150	43	
4440	158	762	674	458	24953	62	183	37	
4450	161	844	789	516	27437	62	198	32	
4460	170	919	824	504	29080	70	168	57	
4470	182	930	839	515	29805	69	204	47	
4480	164	907	808	520	29929	69	175	52	
4490	163	831	793	511	28288	58	167	39	
4500	153	851	719	486	26162	49	199	44	
4510	141	775	677	427	23495	54	156	43	
4520	130	632	596	357	19865	54	131	37	
4530	95	583	483	282	16564	30	107	28	

Energy (eV)	Figure 3C			Figure 3F			Figure 3I		
	Ca-core	PolyP	Ba-rich	PolyP	Ba-Sr-rich	Sr-rich	PolyP	Ba-rich	
ev	counts	counts	counts	counts	counts	counts	counts	counts	
4540	64	454	404	259	13546	31	80	28	
4550	75	356	338	223	10652	23	73	23	
4560	44	249	249	140	8162	25	77	17	
4570	46	197	177	108	6260	19	36	12	
4580	27	158	133	92	4580	7	33	9	
4590	31	115	103	78	3591	9	28	8	
4600	17	98	75	58	2753	9	25	7	
4610	19	75	69	40	2143	7	20	2	
4620	9	56	49	43	1893	2	7	3	
4630	14	37	49	32	1680	6	6	3	
4640	14	50	47	26	1567	3	8	5	
4650	11	33	49	30	1459	5	10	2	
4660	9	40	39	33	1470	7	8	2	
4670	7	38	45	33	1539	2	11	2	
4680	9	58	53	31	1607	5	12	1	
4690	9	37	41	22	1711	6	6	3	
4700	18	61	43	50	1923	8	12	4	
4710	17	65	55	56	2286	11	9	2	
4720	12	86	86	59	2622	11	20	3	
4730	16	115	103	63	3254	12	15	5	
4740	22	117	131	81	3920	7	20	10	
4750	32	169	134	101	4970	9	34	6	
4760	46	178	183	107	6359	16	29	14	
4770	54	240	226	142	7648	23	53	11	
4780	48	308	259	164	9272	17	60	16	
4790	60	360	316	196	10647	21	66	21	
4800	79	396	328	215	12367	23	74	15	
4810	75	446	385	250	13678	36	83	20	
4820	90	472	451	296	14686	40	92	20	
4830	90	497	428	252	15417	44	116	29	
4840	107	495	418	254	15664	24	103	39	
4850	73	451	444	278	15521	36	117	23	
4860	97	487	439	262	14910	38	108	28	
4870	98	454	410	256	14181	30	103	31	
4880	74	408	376	230	12819	34	78	18	
4890	73	392	330	200	11677	32	66	31	
4900	62	325	308	181	10306	28	73	20	
4910	50	321	288	167	9115	16	55	17	

Energy (eV)	Figure 3C			Figure 3F		Figure 3I		
	Ca-core	PolyP	Ba-rich	PolyP	Ba-Sr-rich	Sr-rich	PolyP	Ba-rich
ev	counts	counts	counts	counts	counts	counts	counts	counts
4920	51	278	216	136	7924	17	64	18
4930	48	221	231	134	7174	16	46	18
4940	30	236	189	119	6215	18	43	11
4950	37	188	158	94	5229	15	41	12
4960	27	161	147	84	4620	14	26	6
4970	25	142	111	78	4216	9	25	13
4980	20	115	122	77	3602	5	23	6
4990	27	99	101	48	3194	4	23	6
5000	18	86	89	50	2803	5	24	9
5010	15	84	81	40	2531	6	19	8
5020	13	62	66	33	2253	12	10	5
5030	13	67	64	39	2179	4	11	2
5040	14	68	47	43	2112	5	12	7
5050	11	67	38	32	1982	1	15	4
5060	14	71	60	38	2091	3	13	1
5070	11	72	71	42	2364	8	14	3
5080	18	83	78	46	2640	6	11	10
5090	29	100	84	55	3086	5	24	5
5100	15	115	102	66	3503	9	18	3
5110	24	143	108	64	3863	14	13	3
5120	29	131	121	87	4299	11	26	17
5130	44	177	162	88	4682	10	33	11
5140	26	135	157	91	4946	18	32	6
5150	30	155	148	97	5344	17	39	13
5160	29	158	171	108	5501	7	38	6
5170	41	170	159	85	5545	13	32	4
5180	24	178	145	91	5240	23	31	7
5190	34	139	127	96	4981	10	28	8
5200	30	151	123	74	4547	9	29	8
5210	24	141	134	62	4035	11	17	5
5220	28	116	80	54	3637	8	18	2
5230	24	97	73	62	3036	2	24	4
5240	18	94	88	61	2651	8	26	8
5250	18	75	64	42	2338	9	19	3
5260	13	70	68	33	1993	3	14	6
5270	8	51	46	33	1715	2	11	7
5280	8	40	32	37	1532	7	9	4
5290	7	41	34	21	1316	2	15	3

Energy (eV)	Figure 3C			Figure 3F			Figure 3I		
	Ca-core	PolyP	Ba-rich	PolyP	Ba-Sr-rich	Sr-rich	PolyP	Ba-rich	
	ev	counts	counts	counts	counts	counts	counts	counts	counts
5300	9	35	24	29	1222	2	8	2	
5310	3	38	27	18	1146	3	5	2	
5320	5	35	23	23	1136	2	7	0	
5330	6	41	26	19	1019	2	3	2	
5340	7	30	34	20	1066	3	9	1	
5350	9	23	33	19	1068	5	7	1	
5360	6	32	37	23	1062	3	10	0	
5370	4	26	30	21	1108	10	7	2	
5380	5	33	28	28	1131	1	3	2	
5390	7	34	20	20	1095	1	6	2	
5400	4	30	23	20	1068	3	6	1	
5410	9	38	27	26	1213	3	4	0	
5420	4	27	28	19	1213	3	3	1	
5430	6	40	37	28	1286	2	7	3	
5440	11	42	36	21	1355	1	9	5	
5450	4	47	29	22	1437	12	9	0	
5460	8	42	42	39	1638	5	8	0	
5470	9	66	53	40	1920	2	15	3	
5480	9	59	54	35	2007	7	12	4	
5490	16	79	55	40	2243	7	19	4	
5500	17	77	57	45	2550	7	21	3	
5510	18	82	68	43	2580	10	14	1	
5520	16	78	71	40	2720	9	22	4	
5530	19	79	61	57	2833	9	20	2	
5540	17	85	78	47	2857	6	18	4	
5550	16	88	72	56	2747	5	26	7	
5560	17	85	64	60	2622	8	25	5	
5570	17	70	61	49	2457	4	27	4	
5580	20	66	53	43	2318	6	11	4	
5590	17	65	56	44	2117	7	15	6	
5600	9	41	48	45	1863	4	8	2	
5610	10	38	50	29	1629	6	13	2	
5620	9	40	35	31	1506	6	15	1	
5630	9	39	32	18	1292	4	7	2	
5640	10	44	28	26	1190	4	5	5	
5650	3	29	19	26	1170	2	4	0	
5660	5	27	34	22	1022	4	9	0	
5670	5	27	18	30	1054	4	9	1	

Energy (eV)	Figure 3C			Figure 3F		Figure 3I		
	Ca-core	PolyP	Ba-rich	PolyP	Ba-Sr-rich	Sr-rich	PolyP	Ba-rich
ev	counts	counts	counts	counts	counts	counts	counts	counts
5680	10	22	24	20	993	10	7	1
5690	7	31	29	15	1014	3	5	0
5700	4	25	27	22	1031	5	7	2
5710	7	30	24	16	1106	2	8	1
5720	7	37	30	28	1147	8	8	3
5730	10	32	32	24	1282	5	5	3
5740	7	36	37	28	1328	6	11	4
5750	4	29	32	23	1460	2	8	3
5760	11	42	40	38	1464	3	8	3
5770	11	58	47	30	1564	8	11	2
5780	11	55	37	36	1673	1	10	3
5790	12	60	48	35	1732	2	6	4
5800	11	53	39	41	1637	5	13	2
5810	15	50	41	29	1671	2	15	1
5820	11	53	46	31	1589	3	13	5
5830	3	44	29	29	1595	5	9	5
5840	7	51	28	33	1491	4	13	2
5850	10	52	33	33	1445	2	13	2
5860	8	36	43	19	1313	4	7	1
5870	2	33	32	21	1279	5	5	1
5880	7	28	31	17	1224	4	7	2
5890	5	49	29	20	1126	1	7	6
5900	5	39	23	16	1068	3	7	2
5910	3	23	20	19	1057	2	10	1
5920	6	38	22	14	982	1	7	0
5930	5	22	23	18	1019	4	6	1
5940	7	28	20	17	932	1	7	0
5950	3	29	15	14	927	3	4	0
5960	6	26	23	16	953	5	7	3
5970	10	29	18	21	925	4	4	1
5980	5	32	22	19	908	4	2	1
5990	4	20	26	22	928	3	8	2
6000	8	31	21	24	979	3	3	0
6010	2	26	20	22	905	2	6	0
6020	8	15	24	16	829	2	6	1
6030	3	11	15	17	829	5	1	2
6040	6	26	21	24	826	3	4	1
6050	3	18	19	16	833	1	3	3

Energy (eV)	Figure 3C			Figure 3F			Figure 3I		
	Ca-core	PolyP	Ba-rich	PolyP	Ba-Sr-rich	Sr-rich	PolyP	Ba-rich	
	ev	counts	counts	counts	counts	counts	counts	counts	counts
6060	3	20	8	13	789	5	4	0	
6070	4	22	19	16	785	1	3	1	
6080	4	18	13	14	749	2	6	2	
6090	3	21	16	15	728	3	5	1	
6100	6	15	13	19	777	1	3	0	
6110	5	19	28	16	775	5	7	0	
6120	5	21	13	15	688	2	3	0	
6130	2	17	16	19	766	6	4	0	
6140	7	21	6	12	740	4	2	2	
6150	7	27	19	21	681	1	10	1	
6160	5	23	22	13	794	2	6	0	
6170	4	12	16	17	761	0	3	0	
6180	3	20	17	20	788	1	5	1	
6190	3	13	20	14	724	2	5	2	
6200	8	16	19	17	774	2	7	1	
6210	5	20	11	16	797	2	9	1	
6220	3	17	9	16	780	5	5	1	
6230	3	19	11	13	800	3	6	0	
6240	4	23	23	17	782	4	5	1	
6250	6	23	20	15	794	3	5	0	
6260	4	21	25	14	782	3	5	2	
6270	5	28	16	21	813	2	6	1	
6280	4	29	17	18	826	2	6	2	
6290	6	23	15	12	885	1	3	0	
6300	6	31	22	27	902	4	4	2	
6310	1	31	20	17	804	1	7	0	
6320	2	16	14	19	844	1	5	0	
6330	4	16	11	20	870	3	4	2	
6340	10	25	17	12	797	1	6	0	
6350	3	23	24	19	864	1	7	2	
6360	2	25	23	6	875	2	6	2	
6370	5	25	18	11	875	3	9	1	
6380	6	29	20	15	881	2	8	1	
6390	4	21	18	20	867	2	5	1	
6400	2	22	19	14	854	2	5	0	
6410	3	19	20	24	852	3	7	4	
6420	3	23	21	23	880	6	3	0	
6430	3	24	15	15	807	3	8	3	

Energy (eV)	Figure 3C			Figure 3F			Figure 3I		
	Ca-core	PolyP	Ba-rich	PolyP	Ba-Sr-rich	Sr-rich	PolyP	Ba-rich	
	ev	counts	counts	counts	counts	counts	counts	counts	counts
6440	4	21	12	20	848	0	5	2	
6450	2	26	16	10	798	3	5	0	
6460	5	33	11	16	795	1	10	1	
6470	3	20	19	19	765	3	4	1	
6480	6	20	22	12	777	1	1	0	
6490	2	29	18	12	752	1	3	0	
6500	6	23	15	20	773	4	2	1	

Table S12: Numerical data associated with the three isotope plots ($\delta^{88}\text{Sr}$ vs $\delta^{84}\text{Sr}$ and $\delta^{88}\text{Sr}$ vs $\delta^{87}\text{Sr}$ shown in Figure S2).

$\delta^{84}\text{Sr}$	$\delta^{88}\text{Sr}$	$\delta^{87}\text{Sr}$
value	value	value
-1.051	0.951	0.476
-0.886	0.886	0.444
-1	0.906	0.455
-1.014	0.991	0.497
-1.02	0.986	0.496
-1.037	1.028	0.516
-1.025	1.114	0.559
-1.235	1.18	0.591
-1.003	1.318	0.660
-1.626	1.475	0.740
-0.917	0.893	0.449
-1.057	0.902	0.453
-1.08	1.026	0.514
-0.868	0.886	0.445
-0.857	0.85	0.426
-0.619	0.619	0.310
-0.65	0.618	0.309
-0.571	0.616	0.308
-0.608	0.633	0.316
-0.76	0.709	0.355
-0.812	0.719	0.361
-0.905	0.85	0.428
-1.068	0.932	0.468
-0.984	0.898	0.451
-0.947	0.861	0.432

$\delta^{84}\text{Sr}$	$\delta^{88}\text{Sr}$	$\delta^{87}\text{Sr}$
value	value	value
-0.977	0.895	0.449
-0.984	0.94	0.472
-1.074	0.98	0.493
-1.094	1.013	0.509
-1.119	1.104	0.553
-1.236	1.198	0.601
-1.257	1.282	0.644
-1.424	1.434	0.719
-0.84	0.855	0.429
-0.884	0.89	0.447
-1.016	0.999	0.502
-0.976	0.908	0.456
-0.92	0.855	0.429
-0.546	0.604	0.303
-0.57	0.607	0.319
-0.663	0.632	0.306
-0.709	0.704	0.317
-0.71	0.731	0.353
-0.879	0.87	0.367
-0.963	0.965	0.438
-0.837	0.799	0.485
-0.818	0.83	0.400
-1.041	0.851	0.416
-0.889	0.916	0.426
-0.927	0.931	0.459
-0.951	1.001	0.467
-1.048	1.091	0.503
-1.257	1.129	0.548
-1.215	1.212	0.566
-1.49	1.426	0.609
-0.912	0.8	0.717
-0.883	0.855	0.401
-1.006	0.918	0.428
-0.858	0.81	0.461
-0.848	0.816	0.407
-0.611	0.608	0.411
-0.727	0.625	0.304
-0.61	0.609	0.313
-0.63	0.622	0.305

$\delta^{84}\text{Sr}$	$\delta^{88}\text{Sr}$	$\delta^{87}\text{Sr}$
value	value	value
-0.773	0.787	0.356
-0.919	0.847	0.395
-1.025	0.893	0.425
-0.919	0.899	0.447
-0.81	0.927	0.452
-0.862	0.965	0.466
-1.457	1.427	0.625
-1.048	1.079	0.485
-1.398	1.468	0.716
-1.763	1.673	0.737
-0.843	0.792	0.839
-0.665	0.602	0.396
-0.577	0.622	0.302
-0.916	0.869	0.312
-0.818	0.899	0.436
-0.794	0.944	0.452
-0.99	1.068	0.474
-1.151	1.167	0.537
-1.349	1.24	0.586
-1.48	1.416	0.623
-1.549	1.473	0.710
-1.736	1.642	0.739
-0.831	0.789	0.824
-0.544	0.592	0.396
-0.575	0.622	0.296
-1.009	0.899	0.312
-0.926	0.894	0.451
-0.747	0.915	0.449
-0.919	0.943	0.460
-0.934	1.069	0.474
-1.217	1.188	0.536
-1.086	1.257	0.596
-1.35	1.438	0.632
-1.385	1.467	0.720
-1.592	1.667	0.737
-0.924	0.795	0.836
-0.561	0.61	0.400
-0.572	0.62	0.307
-1.023	0.893	0.311

$\delta^{84}\text{Sr}$	$\delta^{88}\text{Sr}$	$\delta^{87}\text{Sr}$
value	value	value
-0.56	0.688	0.448
-0.758	0.834	0.346
-0.754	0.853	0.418
-1.497	1.439	0.428
-0.733	0.733	0.721
-0.845	0.718	0.368
-0.61	0.546	0.360
-0.451	0.552	0.274
-0.928	0.825	0.277
-0.547	0.646	0.413
-0.689	0.79	0.324
-0.689	0.78	0.396
-1.486	1.389	0.392
-0.773	0.695	0.697
-0.578	0.679	0.349
-0.572	0.542	0.341
-0.667	0.531	0.273
-0.869	0.815	0.267
-0.802	0.699	0.410
-0.772	0.812	0.350
-0.869	0.802	0.407
-1.386	1.395	0.402
-0.73	0.737	0.700
-0.738	0.702	0.369
-0.499	0.539	0.353
-0.591	0.549	0.271
-0.776	0.818	0.275
-0.543	0.744	0.410
-0.98	0.735	0.374
-1.449	1.609	0.369
-0.937	0.739	0.807
-0.909	0.887	0.371
-0.863	0.774	0.446
-0.765	0.736	0.388
-0.88	0.719	0.369
-1.884	1.619	0.360

Table S13: Temporal evolution of Ba, Sr, and Ca concentrations in different fractions in non-inoculated control.

Fraction	Dissolved AEE fraction (>0.22µM) (µM)						Bulk fraction (µM)					
	Ba		Sr		Ca		Ba		Sr		Ca	
Time(h)	values	2SD	values	2SD	values	2SD	values	SD	values	SD	values	SD
0	244.42	1.04	268.10	4.79	246.64	0.58	244.42	1.04				
67	207.75	0.39	264.13	1.09	241.12	2.87	212.91	1.66	266.03	3.59	240.16	0.43
75	199.51	1.36	268.55	1.35	236.38	1.06	206.44	1.41	265.43	1.23	239.94	1.63
90	175.26	0.82	267.66	3.62	238.15	3.14	178.34	2.05	266.46	0.90	237.50	4.46
99	162.68	1.27	265.54	2.22	237.58	6.08	168.19	0.74	268.21	3.66	240.89	2.29
114	149.06	2.60	266.33	1.35	238.28	2.73	148.67	0.49	260.00	2.88	234.72	1.96
123	140.68	0.68	266.54	2.33	239.49	1.97	140.50	1.82	260.60	2.19	235.80	2.38
138	129.82	1.98	266.36	1.66	240.16	3.88	131.98	1.00	263.84	2.13	234.89	1.60
147	124.32	2.30	266.44	3.23	241.25	2.56						
162	118.32	0.12	269.25	0.88	238.00	1.36	118.93	1.71	262.22	0.73	235.03	1.55
171	114.19	1.36	268.87	3.25	242.21	3.08						
187	111.09	0.21	270.92	2.57	243.77	1.43						
234	97.70	1.01	259.24	3.17	231.33	1.16	100.46	2.04	261.73	2.72	235.69	0.71
258	98.13	0.61	267.11	2.72	241.49	3.93	96.33	0.76	258.19	2.05	234.50	3.24
282	92.39	0.28	261.36	1.18	232.46	4.79	93.41	0.44	259.11	3.08	233.46	2.42
307	90.39	1.02	262.54	3.64	236.46	1.76	91.47	2.10	257.16	3.81	234.54	2.85
330	89.97	0.79	270.12	3.89	241.45	0.70	90.29	1.02	264.47	1.42	236.25	4.44
361	86.28	0.85	261.39	0.98	236.48	3.91	87.93	0.68	262.19	0.48	236.62	1.79
385	85.26	1.98	262.49	2.01	235.44	2.27	86.10	1.13	255.79	0.80	231.99	2.16
411	85.24	1.06	262.73	1.36	242.92	4.02	87.80	1.67	265.88	2.20	238.92	1.97
428	85.06	1.40	263.43	1.90	239.72	1.60	86.80	1.05	259.78	1.21	234.31	4.10
451	86.97	1.55	269.10	0.57	243.89	2.16	85.47	0.59	259.92	3.48	235.51	0.64
480	86.30	0.90	270.95	0.76	240.52	3.09	86.30	0.97	261.76	2.05	236.31	1.31
506	85.22	0.46	261.67	0.62	238.34	1.16	87.22	0.56	261.78	0.52	235.11	1.93
530	84.16	0.78	263.82	0.55	238.15	1.34	85.01	1.23	258.64	3.32	233.74	3.26

Fraction	Dissolved AEE fraction (>0.22μM) (μM)						Bulk fraction (μM)					
	Ba		Sr		Ca		Ba		Sr		Ca	
Time(h)	values	2SD	values	2SD	values	2SD	values	SD	values	SD	values	SD
554	86.62	0.12	266.19	3.62	239.02	3.08	86.12	0.42	261.34	3.37	243.48	0.55
580	85.75	0.66	264.53	2.12	236.38	1.57	83.48	1.13	253.91	0.30	234.10	1.22
603	81.37	0.27	250.43	1.91	236.24	3.99	86.55	0.73	263.58	3.91	237.39	1.37
625	83.47	0.15	260.78	2.34	232.69	2.09	85.12	0.56	258.06	1.80	233.70	2.85
651	82.12	0.35	258.14	2.45	227.67	3.14	83.22	0.83	252.31	1.36	229.61	3.06
674	82.40	0.21	257.28	2.31	229.99	1.97	88.46	0.31	266.85	4.08	240.37	2.86
699	83.58	1.76	258.13	3.62	231.58	3.70	87.47	2.14	259.08	1.03	239.69	2.38

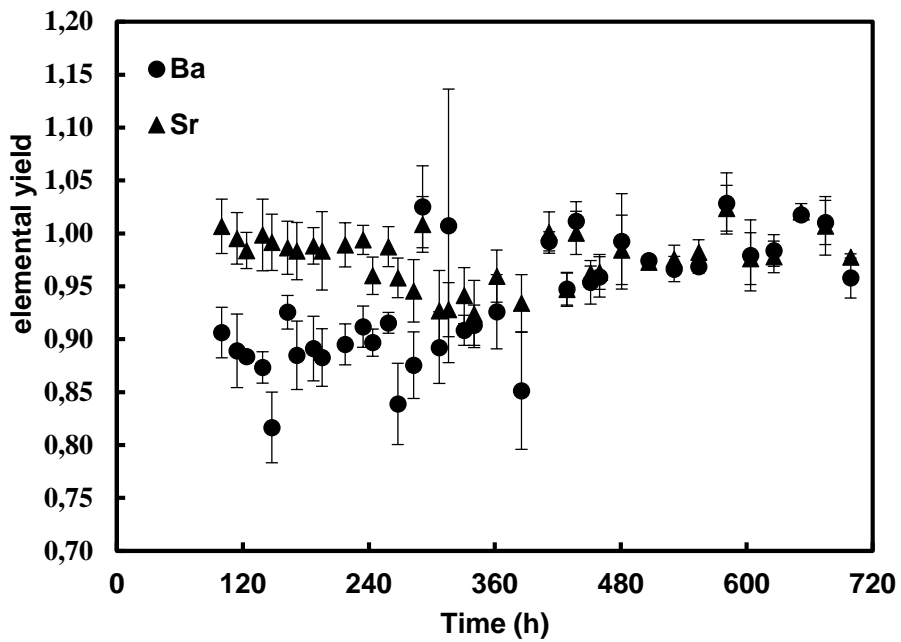


Figure S1: Temporal evolution of the elemental yield (defined as the ratio between the sum of the element concentration in solution plus bacteria fractions, and the element concentration in the bulk fraction) for Ba (●) and Sr (▲). Data points and error bars correspond to the average and standard deviation (with gaussian uncertainty propagation) of three replicate cultures. The average elemental yield is $93 \pm 7\%$ and $98 \pm 4\%$ for Ba and Sr. The numerical data are provided in Table S8.

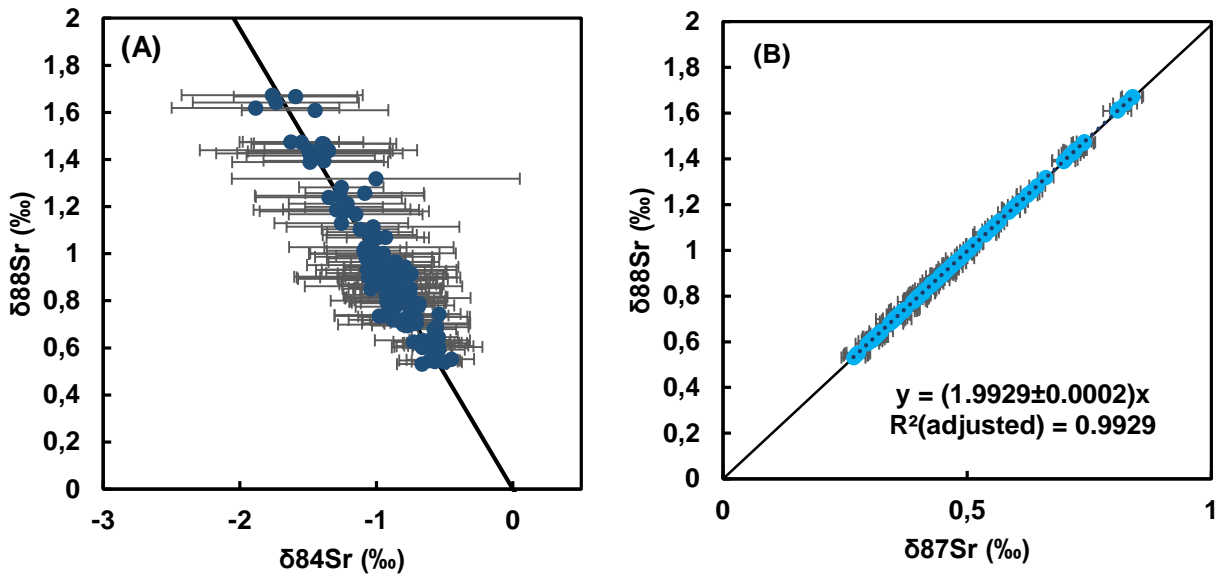


Figure S2: Three-isotopes plots: (A) $\delta^{88}\text{Sr}$ vs $\delta^{84}\text{Sr}$; (B) $\delta^{88}\text{Sr}$ vs $\delta^{87}\text{Sr}$. The black line represents the trend expected for mass-dependent fractionation. $\delta^{87}\text{Sr}$ and $\delta^{84}\text{Sr}$ values were calculated by the standard-sample bracketing method, just as explained in the main text for $\delta^{88}\text{Sr}$. The numerical data is provided in Table S12.

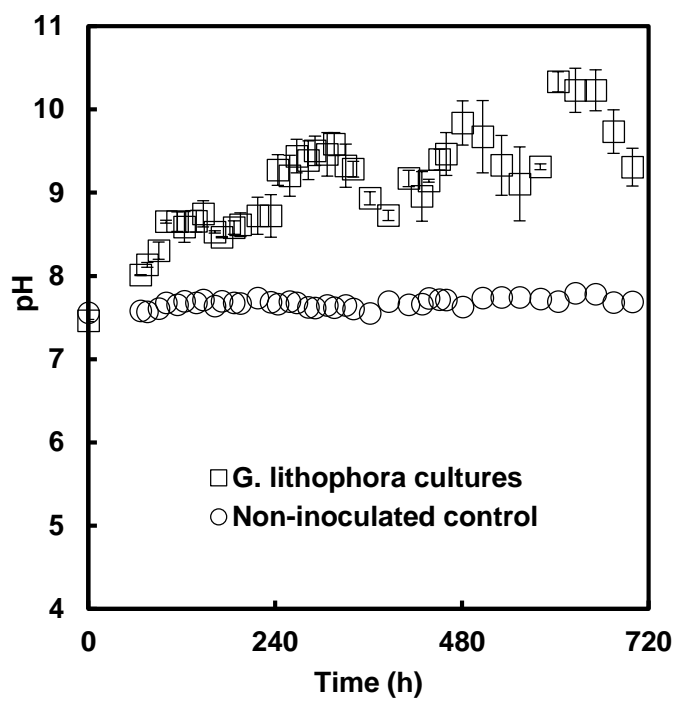


Figure S3: Temporal evolution of solution pH during the growth of *G. lithophora* cultures (□) and in the non-inoculated control (○). Error bars denote standard deviation of triplicate cultures. No replicates were done for non-inoculated control. The numerical data is provided in Table S7.

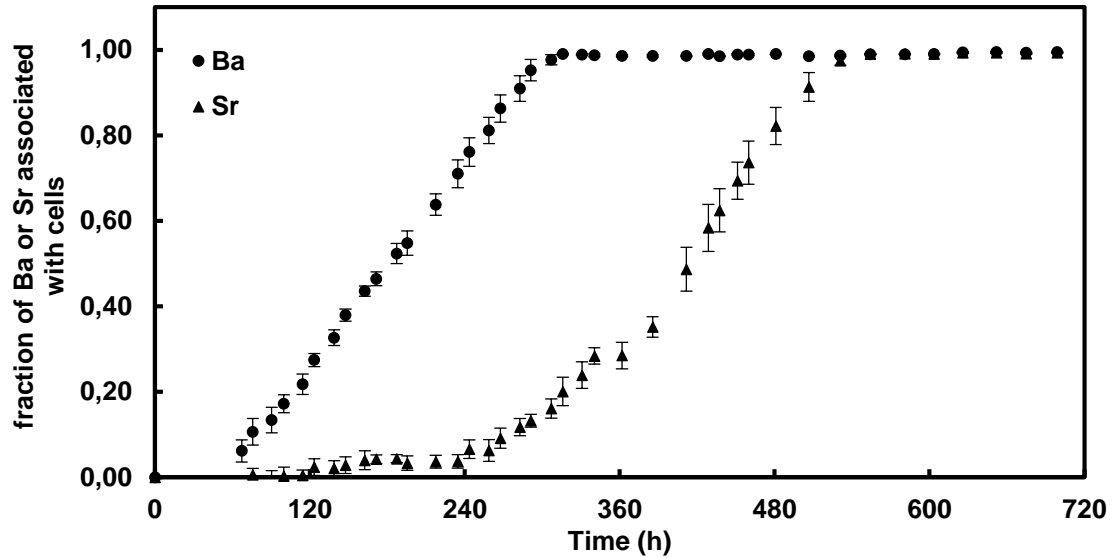


Figure S4: Temporal evolution of the proportion of total Ba (circles) and Sr (triangles) present in *G. lithophora* cells. Error bars are standard deviation of the triplicate measurement. Numerical data are provided in Table S8.

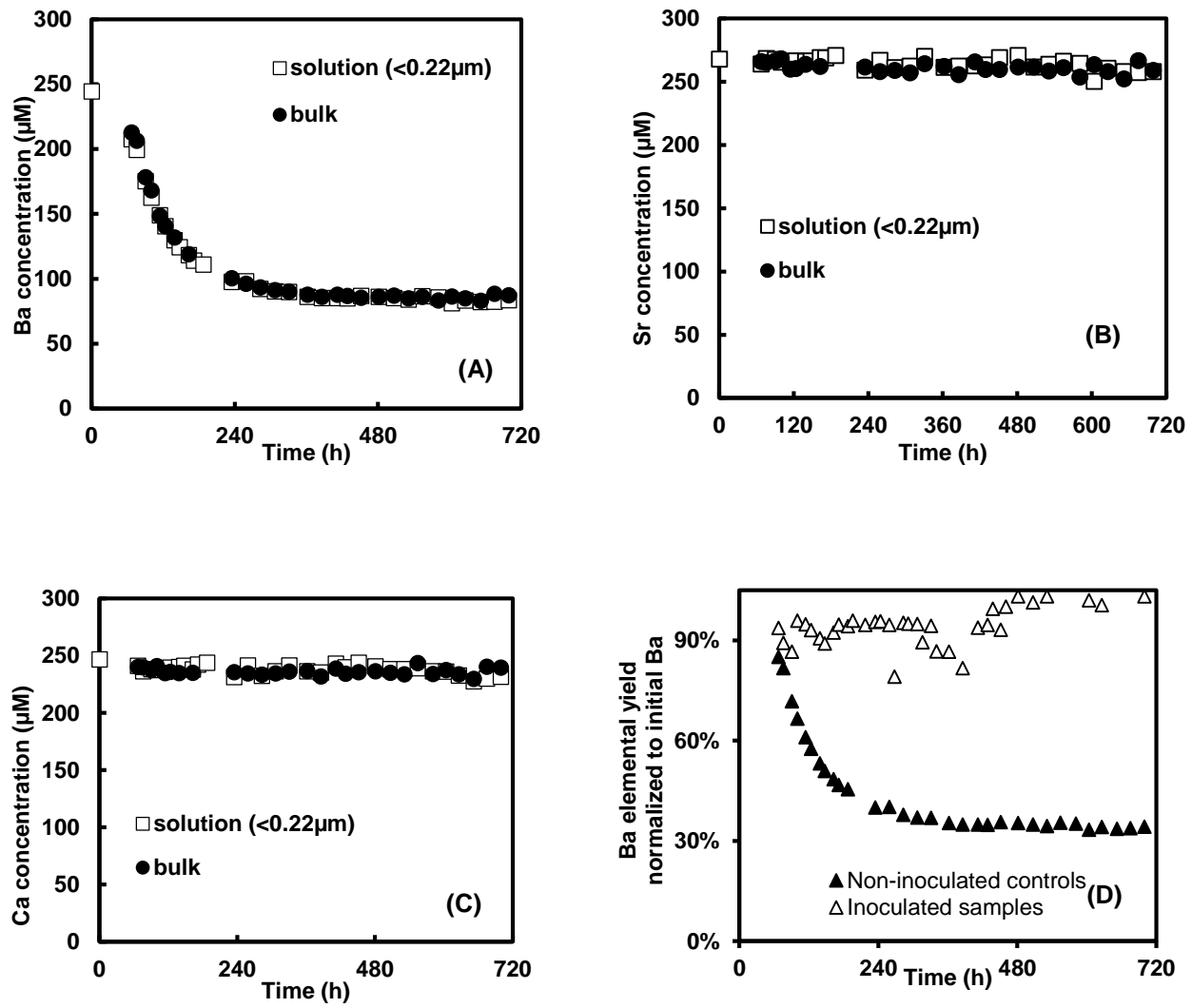


Figure S5: (A) Temporal evolution of Ba concentrations in solution (□) and bulk (●) fraction in the non-inoculated control. (B) Temporal evolution of Sr concentrations in solution (□) and bulk fraction (●) in the non-inoculated control. (C) Temporal evolution of Ca concentrations in solution (□) and bulk fraction (●) in the non-inoculated control. Data points and error bars correspond to the average and standard deviation of triplicate measurement done on same sample using ICP-OES, respectively. (D) Ba elemental yield normalized to initial Ba concentration in the solution for non-inoculated control and inoculated control. The numerical data is provided in Table S13.